NASA/TM—2016–219070

Assessment of JVX Proprotor Performance Data in Hover and Airplane-Mode Flight Conditions

C. W. Acree, Jr.
Ames Research Center
Moffett Field, California

February 2016

NASA STI Program ... in Profile

Since its founding, NASA has been dedicated to the advancement of aeronautics and space science. The NASA scientific and technical information (STI) program plays a key part in helping NASA maintain this important role.

The NASA STI program operates under the auspices of the Agency Chief Information Officer. It collects, organizes, provides for archiving, and disseminates NASA's STI. The NASA STI program provides access to the NTRS Registered and its public interface, the NASA Technical Reports Server, thus providing one of the largest collections of aeronautical and space science STI in the world. Results are published in both non-NASA channels and by NASA in the NASA STI Report Series, which includes the following report types:

- TECHNICAL PUBLICATION. Reports of completed research or a major significant phase of research that present the results of NASA Programs and include extensive data or theoretical analysis. Includes compilations of significant scientific and technical data and information deemed to be of continuing reference value. NASA counterpart of peer-reviewed formal professional papers but has less stringent limitations on manuscript length and extent of graphic presentations.

- TECHNICAL MEMORANDUM. Scientific and technical findings that are preliminary or of specialized interest, e.g., quick release reports, working papers, and bibliographies that contain minimal annotation. Does not contain extensive analysis.

- CONTRACTOR REPORT. Scientific and technical findings by NASA-sponsored contractors and grantees.

- CONFERENCE PUBLICATION. Collected papers from scientific and technical conferences, symposia, seminars, or other meetings sponsored or co-sponsored by NASA.

- SPECIAL PUBLICATION. Scientific, technical, or historical information from NASA programs, projects, and missions, often concerned with subjects having substantial public interest.

- TECHNICAL TRANSLATION. English-language translations of foreign scientific and technical material pertinent to NASA's mission.

Specialized services also include organizing and publishing research results, distributing specialized research announcements and feeds, providing information desk and personal search support, and enabling data exchange services.

For more information about the NASA STI program, see the following:

- Access the NASA STI program home page at http://www.sti.nasa.gov

- E-mail your question to help@sti.nasa.gov

- Phone the NASA STI Information Desk at 757-864-9658

- Write to:
  NASA STI Information Desk
  Mail Stop 148
  NASA Langley Research Center
  Hampton, VA 23681-2199

NASA/TM—2016–219070

Assessment of JVX Proprotor Performance Data in Hover and Airplane-Mode Flight Conditions

C. W. Acree, Jr.
Ames Research Center
Moffett Field, California

National Aeronautics and
Space Administration

Ames Research Center
Moffett Field, CA 94035-1000

February 2016

Acknowledgments

The author wishes to thank Randy Peterson of Ames Research Center for maintaining several priceless rotor test datasets extending back over three decades. Such efforts are too often undervalued. Further thanks are owed to Wayne Johnson, also of Ames, for his long-standing support and encouragement for this research.

Available from:

NASA STI Support Services
Mail Stop 148
NASA Langley Research Center
Hampton, VA 23681-2199
757-864-9658

National Technical Information Service
5301 Shawnee Road
Alexandria, VA 22312
webmail@ntis.gov
703-605-6000

Table of Contents

Table of Contents (continued)

List of Figures

List of Figures (continued)

List of Figures (concluded)

List of Tables

Notations

ATB	Advanced Technology Blade
BEMT	Blade Element/Momentum Theory
CAMRAD	Comprehensive Analytical Model of Rotorcraft Aerodynamics and Dynamics
CFD	Computational Fluid Dynamics
DES	Detached Eddy Simulation
DNW	Deutsch-Niederlandischer Windkanal
JVX	Joint Vertical Experimental
NFAC	National Full-Scale Aerodynamics Complex
OARF	Outdoor Aerodynamic Research Facility
PTR	Propeller Test Rig
RDRS	Rotor Data Reduction System
TRAM	Tilt Rotor Aeroacoustic Model
TTR	Tiltrotor Test Rig
U^{2}NCLE	Unstructured UNsteady Computation of fieLd Equations
2D	Two-dimensional
3D	Three-dimensional
40x80	40- by 80-ft NFAC test section

A	rotor disk area
A_{SP}	effective spinner drag area, ft^2
B	Prandtl tip-loss factor
c_d	airfoil section drag coefficient
$c_{d\,\mathrm{mean}}$	mean blade section drag coefficient
c_{d_0}	section drag coefficient at zero lift
c_l	airfoil section lift coefficient
c_{lmax}	maximum section lift coefficient
$c_{d\,\mathrm{2D}}$	drag coefficient from 2D airfoil table
$c_{l\,\mathrm{2D}}$	lift coefficient from 2D airfoil table
C	wind tunnel cross-section area
C_P	rotor power coefficient, $P/(\rho A V_{tip}^3)$
C_{Pi}	induced power coefficient, $P_i/(\rho A V_{tip}^3)$
$C_{P\mathrm{ideal}}$	ideal power coefficient (hover), $C_T^{3/2}/\sqrt{2}$
C_{Pm}	ideal power coefficient, $P_m/(\rho A V_{tip}^3)$
C_{P_o}	profile power coefficient, $P_o/(\rho A V_{tip}^3)$
C_Q	rotor torque coefficient, $Q/(\rho A V_{tip}^2)R$
C_T	rotor thrust coefficient, $T/(\rho A V_{tip}^2)$

Notations (continued)

FM	rotor hover figure of merit, $\left(T\sqrt{T/2\rho A}\right)/P$
F_P	profile power factor
k	number of data points
K_L	Reynolds number factor for lift
K_D	Reynolds number factor for drag
K_{QT}	torque/thrust correction coefficient
K_{TQ}	thrust/torque correction coefficient
m	order of curve fit
M_{tip}	rotor tip Mach number
n	exponent in Reynolds no. correction
N	number of blades
P	rotor power, hp
P_i	rotor induced power, hp
P_o	rotor profile power, hp
P_m	ideal (minimum) rotor power, hp
q_0	tunnel dynamic pressure, lb/ft^2
$q_{.75R}$	dynamic pressure at 0.75 R
Q	rotor torque, ft-lb
Q_s	measured shaft torque
r	regression coefficient
R	rotor radius, ft
Re	Reynolds number (actual)
Re_t	Reynolds number of airfoil table
s_d	standard deviation
s_e	standard error of estimate
T	rotor thrust, lb
v	induced velocity, ft/sec
V	tunnel wind speed, knots
V'	Glauert equivalent velocity, knots
V_{tip}	rotor tip speed, ft/sec
X_b	X-force measured at the balance
X_c	corrected X-force
X_s	measured residual shaft thrust
y	measured value
$\hat{y}$	predicted value
α	angle of attack
α_1	area ratio A/C

Notations (concluded)

Δx	change in x
η	propulsive efficiency TV/P
λ	induced velocity ratio, v/V_{tip}
κ	induced power ratio, $C_{Pi}/C_{P\text{ideal}}$
κ_σ	power factor for swirl losses
κ_τ	power factor for tip losses (=1/B)
Ω	rotor rotational speed
μ	advance ratio V/V_{tip}
ρ	atmospheric density, slug/ft^3
σ	rotor solidity (thrust weighted)
σ_x	measurement uncertainty of x
τ	Glauert thrust coefficient, $T/(\rho A V^2)$
ψ_s	rotor shaft yaw angle, deg

Summary

A 0.656-scale V-22 proprotor, the Joint Vertical Experimental (JVX) rotor, was tested at the NASA Ames Research Center in both hover and airplane-mode (high-speed axial flow) flight conditions, up to an advance ratio of 0.562 (231 knots). This paper examines the two principal data sets generated by those tests, and includes investigations of hub spinner tares, torque/thrust measurement interactions, tunnel blockage effects, and other phenomena suspected of causing erroneous measurements or predictions. Uncertainties in hover and high-speed data are characterized. The results are reported here to provide guidance for future wind tunnel tests, data processing, and data analysis.

Introduction

The JVX rotor was an experimental precursor to the V-22 rotor, hence the name "Joint Vertical Experimental." Several tests of the JVX rotor were performed at NASA Ames Research Center, including hover testing at the NASA Outdoor Aerodynamic Research Facility (OARF) and high-speed, axial-flow tests in the 40- by 80-ft test section (the "40x80") of the National Full-Scale Aerodynamics Complex (NFAC). The hover data were originally reported in reference 1 and the high-speed data in reference 2. Data are also available for the 1/4-scale Tilt Rotor Aeroacoustic Model (TRAM) rotor (ref. 3). This report is a major expansion of references 4 and 5.

Several motivations underlie this work:

- NASA, with the support of the U.S. Army and Air Force, is developing the Tiltrotor Test Rig (TTR) for testing large (26-ft-diameter) proprotors in the NFAC. A re-examination of previous tests and test data was undertaken to assist with equipment design, test planning, and improved data analysis.

- Anomalies in the JVX rotor test data prompted a close look at data and data processing requirements. The uncertainty analyses reported here started out as an effort to detect and understand any errors in the existing database. The methods described here may lead to improved test data collection, processing, and interpretation of the data expected from the TTR. In some cases, the value of the work lies in determining what cannot be definitively analyzed, with the hope that future tests can be planned to generate more useful data sets.

- There was a difference between predictions and high-speed performance data for the JVX isolated rotor (refs. 4 and 5); the problem persists with newly available, independent analyses (ref. 6). A possible cause is suggested here.

This report begins with a description of the JVX rotor and test history, plus a brief summary of the TRAM rotor and test data. Uncertainty analyses of JVX hover and high-speed axial-flow test data are given in separate sections, each with comparisons with CAMRAD II and U^{2}NCLE predictions. This report also includes Appendix A that summarizes an attempt to measure hover performance in the 40x80, plus Appendices B and C that discuss spinner tares and wind tunnel blockage effects, respectively. Numerical data are tabulated in Appendix D (a major revision to the data published in reference 5).

Hover thrust of a proprotor is greater than airplane-mode thrust by approximately the lift-to-drag ratio of the aircraft. For a modern tiltrotor or tilt-wing aircraft, the ratio is at least a factor of 10. The relative effect of any measurement error, nonlinearity, or uncertainty on airplane-mode data is therefore an order of magnitude greater than on hover data. This effect is compounded by large spinner drag tares. These considerations raise major challenges for analysis of wind tunnel data for high-speed proprotors, as reflected by the different approaches taken to analyze the hover and airplane-mode data described in this report.

A Note on Statistics Terminology

While no claims of statistical or terminological rigor are made here, this paper generally observes the difference between *error* and *uncertainty*. Strictly speaking, it is not possible to determine *errors* in the test data presented here, because there are no independent measurements. (There is a minor exception for calibration data, where the reference values have much lower uncertainties than the test data.) In contrast, *uncertainty* can be characterized by statistical means.

This paper uses the traditional term *standard deviation* to refer to variations about a point value, and *standard error of estimate* (or simply *standard error*), *confidence interval,* and *prediction interval* to refer to variations about a regression line, with the implication that they refer to uncertainties in the measurements.

Statistical significance is a measure of the reliability of a test or measurement. The traditional definition of statistical significance is the probability that an observed effect is due purely to chance. Tests of statistical significance were always made at the 5-percent level.

Too little data from the JVX tests survive to perform a proper uncertainty analysis to the standards of reference 7. While this paper freely applies curve fits and makes statistical tests of the data, the purpose is to gain insight into the physical properties of the rotor, not to generate definitive statistical analyses.

The primary reference used for statistics was the classic “Statistics Manual” by Crow, Davis, and Maxfield (ref. 8). A useful and readily available introduction to the newer methods and terminology is NIST Technical Note 1297 (ref. 9). Reference 7 is also recommended.

The JVX Test Rotor

Sometimes referred to as a “2/3-scale V-22,” and more rarely “M901 rotor,” the JVX rotor in fact differed from the V-22 in several respects, as described below. The following description includes information from references 1 and 2. See also reference 10 for JVX airfoil data.

The JVX rotor was 25 feet in diameter, which is 0.656-scale relative to the production V-22. The JVX rotor used an XV-15 hub with fixed, 2.5-deg precone, whereas the V-22 hub has a coning flexure with slightly different at-rest precone. An XV-15 spinner was used for the JVX rotor, instead of the proportionately much shorter V-22 spinner. Hover testing was done with the original JVX blade planform and airfoil distribution, which had linear taper and an XN-28 airfoil at the root. JVX wind tunnel testing was done with a thicker root section to model the V-22 production blade, which must accommodate a folding hinge; the resulting inboard planform did not match that used for the hover tests. The JVX rotor was always tested when mounted to the Propeller Test Rig (PTR), which had a fairing over the rotor balance just behind the hub (Figs. 1 and 2). The trailing edges at the blade roots were slightly clipped to clear the rotor balance fairing. See reference 11 for additional details of the PTR and its installation at the OARF.

All JVX rotor tests were done at the OARF or in the 40x80 test section of the NFAC. No wing was installed for any data reported here. The test article no longer survives.

Another scale V-22 test rotor is the Tilt Rotor Aeroacoustics Model (TRAM); its data are useful for comparison with JVX (and of course V-22). TRAM is a 1/4-scale V-22, designed for acoustics and blade loads measurements; a detailed description is given in reference 3.

Figure 1. The JVX rotor mounted on the PTR for hover tests at the OARF.

Figure 2. The JVX rotor mounted on the PTR for airplane-mode tests in the NFAC.

JVX and TRAM rotor characteristics are summarized in Table 1, with V-22 data for reference. The V-22 data apply to the production version. The test conditions for data presented in this report are summarized in Table 2. Additional details are given in reference 12, from which Table 1 was adapted. Reference 13 presents the most important TRAM test data.

At least five different variations of the blade cuff have been built and tested. For consistent comparisons, the linear portion of each blade, running from about 25 percent radius to the tip, was extrapolated to the root to define a nominal root chord. The values of taper in Table 1 are based on the nominal chord value.

Existing publications of JVX, TRAM, and V-22 typically use nominal, thrust-weighted values of solidity and not necessarily literal values derived from as-built geometry. Table 1 conforms to that convention.

Table 1. JVX and TRAM Rotor Characteristics.

	JVX	TRAM	V-22
Scale, referenced to V-22	0.656	0.25	1
Rotor radius (in.)	150	57	228.5
Solidity (thrust weighted)	0.1138	0.105	0.105
Tip chord (in.)	15.79	5.5	22.0
Taper (tip/root chord)	0.646	0.641	0.641

Test Summary

Complete JVX hover test data were published in reference 1, and very limited airplane-mode data from a subsequent 40x80 test were published in reference 2. A more extensive set of airplane-mode wind tunnel data acquired in 1991 were published in reference 5. A limited amount of hover data were taken during the 1988 40x80 entry (ref. 14).

This paper incorporates data from five separate tests, primarily the 1984 JVX OARF hover test and the 1991 JVX 40x80 test (refs. 1 and 5). Supplementary data include JVX spinner drag data from the 1988 40x80 wind tunnel test (ref. 2) and a very limited amount of balance check-loads data from the 1984 Advanced Technology Blade (ATB) OARF tests (ref. 11). The 1970 XV-15 40x80 wind tunnel test (ref. 15) provides useful data for cross reference, but no actual data from that test are included here. Table 2 summarizes the major tests and datasets.

Table 3 summarizes the JVX test conditions analyzed in depth here. Limited hover data at other tip speeds are reported in reference 1; a subset is briefly examined here. Limited comparisons between OARF and 40x80 hover test data are given in Appendix A.

Table 2. Proprotor Test Datasets.

Test Article	Facility	Date	Dataset No.	Reference No.
XV-15	40x80	1970	Test 374	15
ATB	OARF	1984	Test 910	11
JVX	OARF	1984	Test 911	1
JVX Phase I	40x80	1988	Test 568	14
JVX Phase II	40x80	1991	Test 579	5
TRAM	DNW	1998	Test 20	3

Table 3. JVX Summary Test Conditions.

	Hover	Airplane Mode	
Tip Mach no.	0.676	0.575	0.625
Tip speed (ft/sec)	754	640	695
Airspeed (knots)	0	99–200	231
Density (slug/ft^3)	0.00239	0.00224–0.00234	0.00220

Hover Data and Analyses

JVX hover data were taken outdoors at near-zero wind conditions. The bulk of the hover data were for a nominal tip Mach number (M_{tip}) of 0.68 (754 ft/sec), with a small amount of data at M_{tip} = 0.73. The following discussion is focused on the lower tip speed, which is the design operating condition for the JVX rotor.

Reference 1 provides corrections for wind and plots data at a variety of cut-off wind speeds. Previous publications of JVX hover data (e.g., refs. 4, 5, and 16) typically exclude data above 1 knot. Criteria are developed here for including more data from the dataset. See reference 17 for a completely different approach to wind corrections.

Figures 3 and 4 plot all data at nominal $M_{tip} = 0.68$ and $C_T/\sigma > 0$. Different plot symbols denote different data runs. Each run included one or more thrust sweeps from low to high thrust. The PTR was shut down between each run, and the data system reset with new zeros and resistance calibration checks (R-cals). There were 6 runs at $M_{tip} = 0.68$ for a total of 100 data points.

The maximum attained thrust was $C_T/\sigma = 0.1600$, whereas typical V-22 design hover conditions are $C_T/\sigma = 0.16$ to 0.17 (ref. 18). The V-22 rotor also has lower solidity than the JVX rotor (Table 1). Comparison of JVX OARF data to flight data should therefore be treated with due caution.

The C_P/σ data (Fig. 3) appear to be tightly clustered, but the expanded scale of Figure 4 reveals considerable scatter in figure of merit (*FM*). All data in Figures 3 and 4 are corrected for the effects of wind; the corrections are given in reference 1. Figure 5 shows figure of merit without wind corrections. With wind corrections, the data are generally more consistent run-to-run, most obviously between Run 5 and Run 6. However, there is little apparent effect on the scatter within each run; the scatter in Run 3 is possibly even worse near $C_T/\sigma = 0.11$ for the corrected data (compare Figure 4 to Figure 5).

Figure 6 plots the data of Figure 4, but only for wind <1 knot. The data from Run 5 have been completely eliminated, as have the high-thrust data from Run 6 and most of the data from Run 2. However, the anomalous data point from Run 3 at the highest measured figure of merit ($C_T/\sigma = 0.11$ and $FM = 0.83$) has *not* been eliminated. A different method of selecting data is clearly desirable.

Figure 7 shows histograms of selected parameters for all runs at $M_{tip} = 0.68$ and $C_T/\sigma > 0$ (the same data points as Figures 3–5). Included are counts of M_{tip}, $q_{.75R}$, and V_{tip}, where $q_{.75R}$ is the dynamic pressure at 3/4 blade radius and V_{tip} is the rotor tip speed. V_{tip} is the most accurately measured parameter because it requires only a measurement of rotation speed, whereas M_{tip} requires a measurement of temperature and $q_{.75R}$ requires a measurement of atmospheric density.

M_{tip} shows little variation (Fig. 7a), as does $q_{.75R}$ (Fig. 7b), and both have an approximately Gaussian distribution as expected. However, V_{tip} has a much more erratic distribution (Fig. 7c). Furthermore, all of the points below $V_{tip} = 750$ ft/sec are from Run 3, but $V_{tip} \geq 750$ ft/sec for all other data. Also, no points from Run 1 exceed 753 ft/sec. The spread in the M_{tip} data—the difference between maximum and minimum values, divided by the mean—is ±0.33 percent; but for V_{tip}, the spread is ±1.03 percent (over three times as much). The spread in the $q_{.75R}$ data is ±0.62 percent.

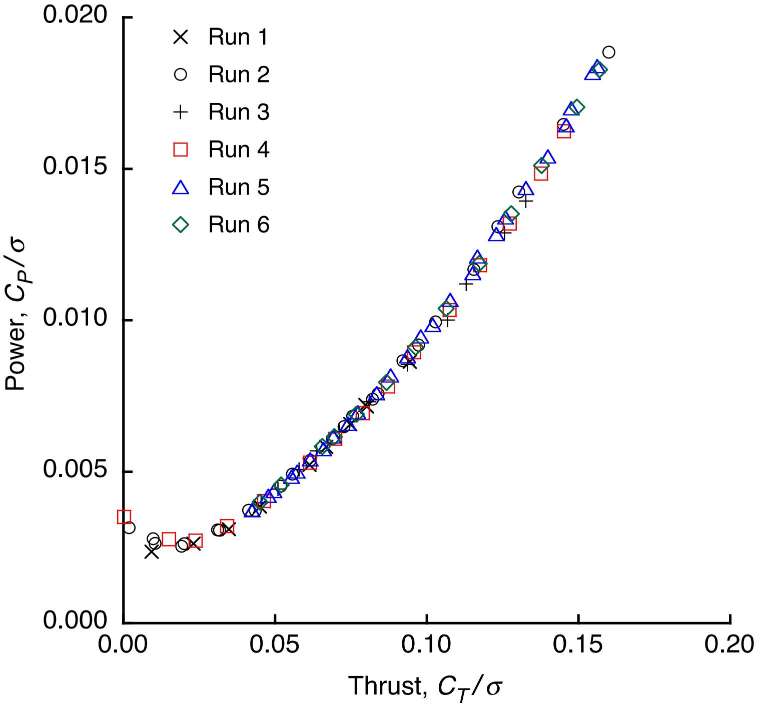

Figure 3. Hover power (corrected for wind) versus thrust, M_{tip} = 0.68.

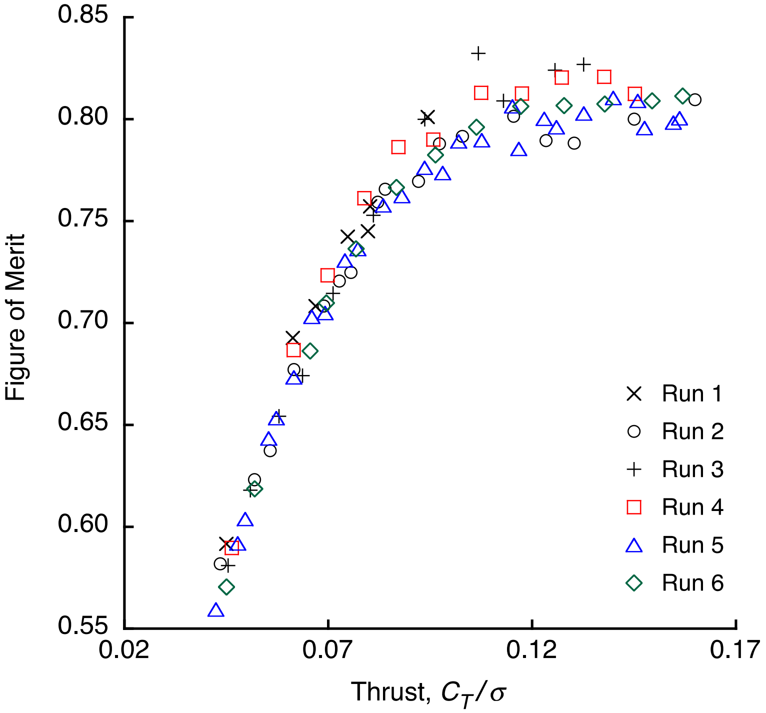

Figure 4. Figure of merit (corrected for wind) versus thrust, M_{tip} = 0.68.

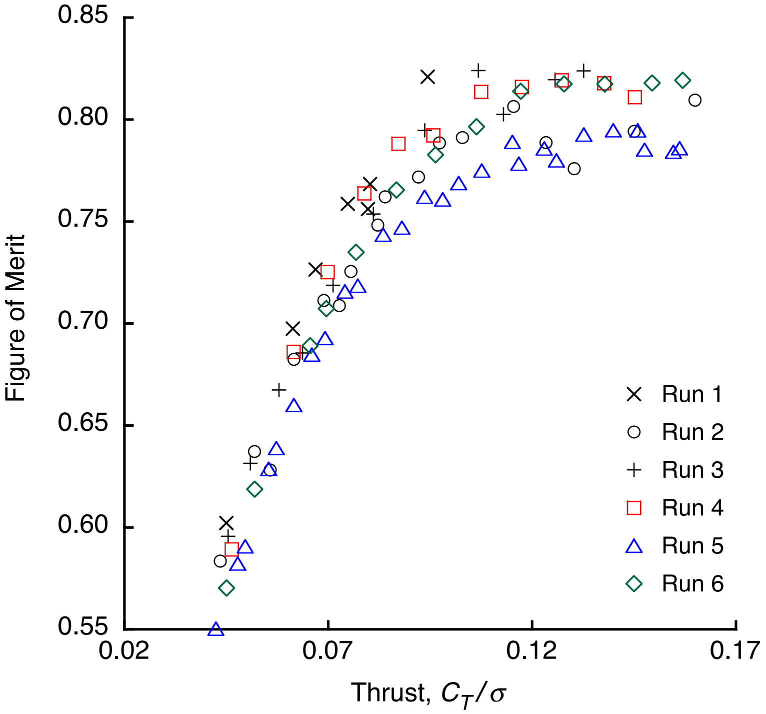

Figure 5. Figure of merit (*without* wind corrections) versus thrust, M_{tip} = 0.68.

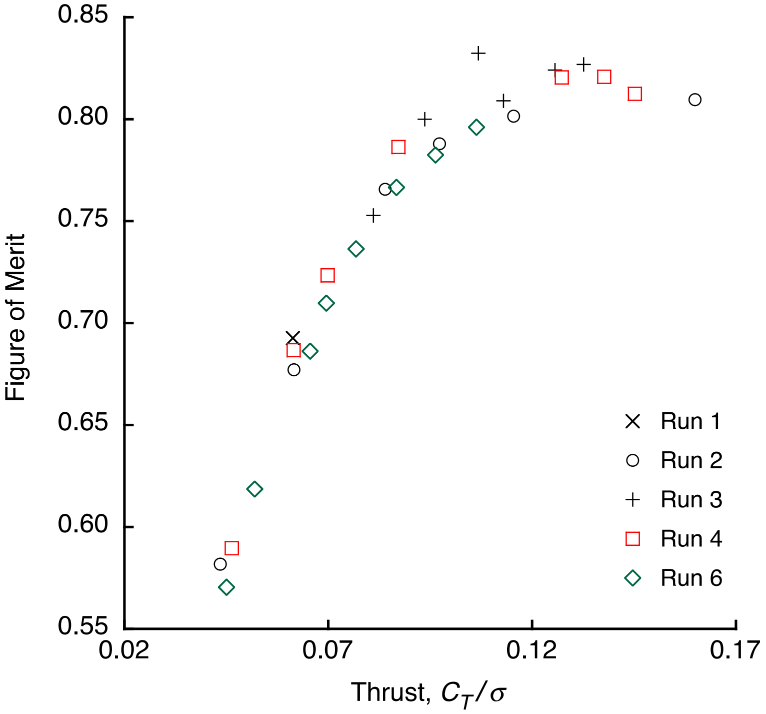

Figure 6. Figure of merit (corrected for wind) versus thrust, M_{tip} = 0.68 and wind <1 knot.

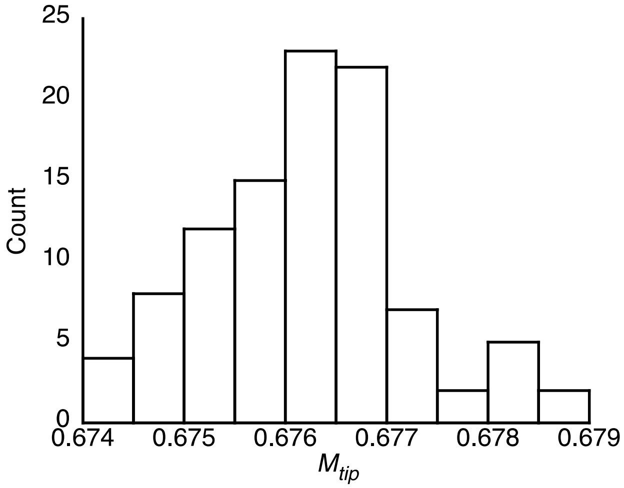

Figure 7(a). Distribution of M_{tip} values.

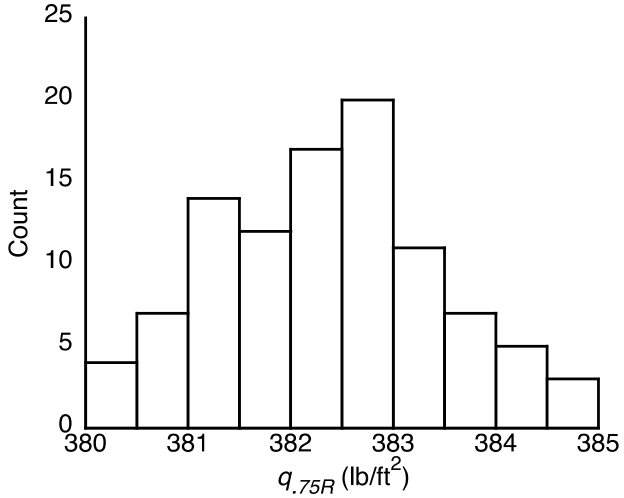

Figure 7(b). Distribution of $q_{.75R}$ values.

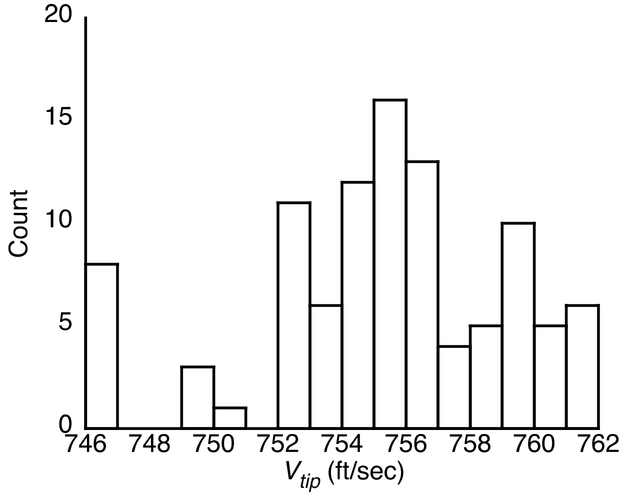

Figure 7(c). Distribution of V_{tip} values.

Some additional insight may be gained by examining the non-ideal power $C_P - C_{P\text{ideal}}$, based on the classic momentum-theory relation

$$C_{P\text{ideal}} = C_T^{3/2} / \sqrt{2} \qquad [1]$$

Figure 8 plots the wind-corrected data as non-ideal versus ideal power. It is evident that the Run 3 data (solid markers) have an anomalous trend between $C_{P\text{ideal}}$ = 0.00044 and 0.00095 (C_T/σ from 0.064 to 0.107). These five data points have the lowest tip speeds of any hover data, and tip speed drops monotonically as thrust increases. Trimming the rotor to constant M_{tip} instead of V_{tip} should give more consistent results, but Figures 4 and 8 suggest otherwise, at least for Run 3. The data from Run 3 are questionable and were therefore excluded from all further analyses reported here.

All of the data were taken by progressively increasing collective to sweep from low to high thrust. Figure 9 shows the data organized by thrust sweep. Runs 2 and 5 had two such sweeps each, with the thrust returned to near-zero at the beginning of the second sweep. These repeated sweeps are here labeled 2A and 2B, and 5A and 5B. Each sweep is plotted as a continuous line, instead of point-by-point, to emphasize the trend within each sweep. Runs 1 and 2B are not shown because they did not extend above C_T/σ = 0.10. The purpose is to select data for further analysis, so it is desirable to include only data runs that span the full range of thrust.

It is evident that Run 4 has consistently higher figure of merit at high thrust, and Runs 2A and 5B have arguably less consistent trends than the other data. There are no obvious parameters in the database that explain these differences, although only a few of the many possible correlations were closely examined. Efforts were instead spent on curve-fitting the data to get the best possible estimate of the rotor performance trend, as described in the next section.

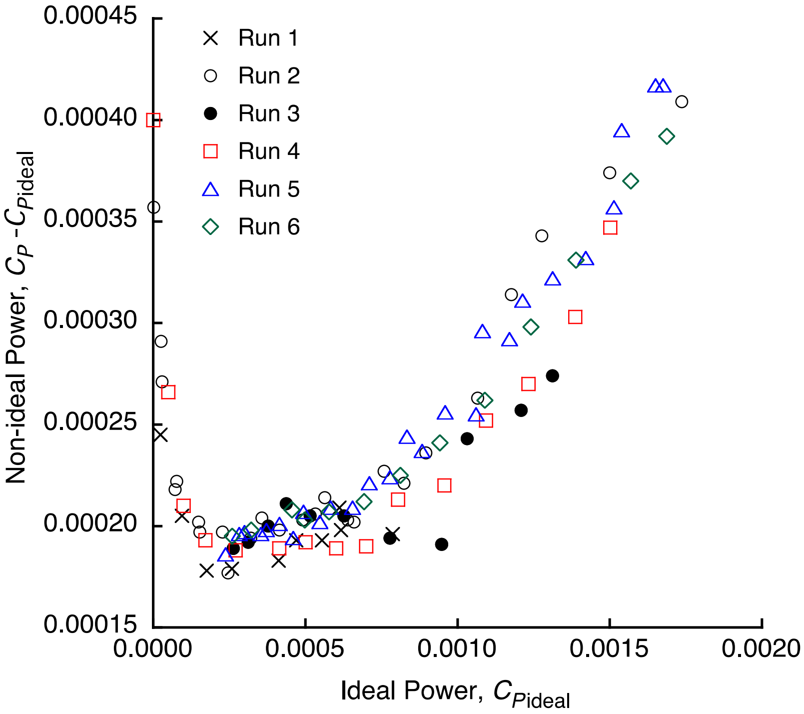

Figure 8. Non-ideal power versus ideal power (corrected for wind), M_{tip} = 0.68.

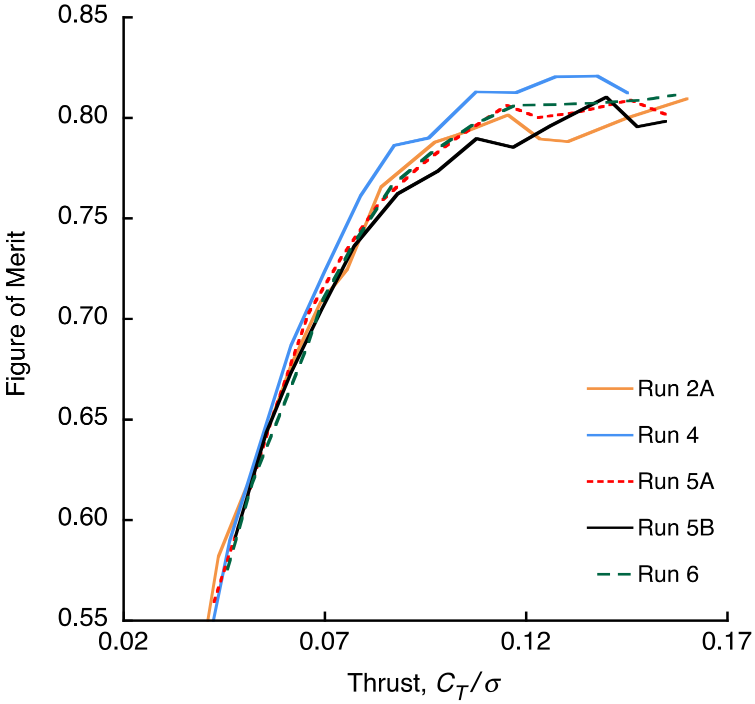

Figure 9. Thrust sweeps by run (corrected for wind), M_{tip} = 0.68.

Regression Analysis of Hover Data

The goal is to estimate the rotor performance trend from several collective sweeps, which have variations in performance trends and scatter between runs. The data were not taken at exactly repeated values of collective or thrust, so point-by-point averaging is not possible. Curve fits across a range of thrust are therefore necessary. Multiple-linear regression is needed to properly capture the trends in the data and to provide reliable estimates of uncertainty in measured performance.

Data at medium and high thrust are generally of more interest that at low thrust, so data for $C_T/\sigma < 0.04$ were excluded. Figure 3 shows that $C_T/\sigma > 0.04$ includes nearly all of the data but excludes the low-thrust data with reversed power trend. Run 3 data were also excluded, for reasons discussed above. The data so filtered comprised 75 data points. Power corrections for wind were included in all curve fits described here, except where noted.

Although some authors have fit figure of merit directly to thrust, this requires a highly nonlinear regression analysis, typically with high-order polynomials in thrust. Fitting power to thrust (or equivalently, C_P to C_T) permits an equally good, if not better, fit with fewer high-order terms (thanks to M. A. McVeigh for pointing this out). The curve fit is then readily transformed to figure of merit. The problem is simplified here because the JVX test never achieved stall, so the data do not show any major change in trend at the high-thrust limit.

Physical reasoning can reduce the choice of functions of the independent variable C_T to a few likely possibilities. Power should approximately follow the momentum theory trend $C_{P\text{ideal}} = C_T^{3/2} \big/ \sqrt{2}$. Below stall, airfoil section drag varies quadratically with lift. For constant tip speed, profile power should therefore vary with C_T^2. There is also the option of including higher-order terms in $C_{P\text{ideal}}$. The scales of Figure 8 were chosen so that a linear fit in $C_{P\text{ideal}}$ would yield a straight line. It is evident that a linear fit will not give a good fit, unless the data are restricted to a narrow range of thrust values (e.g., $C_T/\sigma > 0.10$).

Momentum theory can be extended to include swirl losses, and actuator vortex theory provides an approximation of tip losses (the Prandtl tip-loss correction). From reference 19, a power factor κ_s for swirl losses can be expressed as

$$\kappa_s = \left[1 + 2\frac{C_T}{\sqrt{2}} \ln \frac{C_T}{\sqrt{2}}\right]^{-1/2} \qquad [2]$$

and a factor κ_t for tip losses can be expressed as $1/B$, where B is the Prandtl tip-loss function

$$B = 1 - 2\ln 2 \frac{\sqrt{C_T}}{N} \qquad [3]$$

Combining factors, $C_P = \kappa_s \kappa_t C_{P\text{ideal}}$.

The two loss factors are plotted against C_T / σ in Figure 10 for a three-bladed rotor. Except at very low thrust, the variation of swirl losses with thrust is approximately linear. At medium-to-high thrust, the variation of the tip-loss factor is approximately quadratic, with a negative second-order coefficient. The curve fit for C_P could, therefore, reasonably contain terms in both C_T and C_T^2. Profile power and tip losses should both vary with C_T^2 and therefore cannot be readily distinguished by regression analysis.

Several polynomial curve fits were computed, with different terms as listed in Table 4. Each polynomial also included a constant term (not listed separately in the table).

Table 4. Polynomial regressions for hover data.

Fit No.	Polynomial Terms
1	$C_{P\text{ideal}}$ and $C_{P\text{ideal}}^2$
2	$C_{P\text{ideal}}$ and C_T^2
3	$C_{P\text{ideal}}$ and C_T
4	C_T and C_T^2
5	$C_{P\text{ideal}}$, C_T^2, and C_T
6	$C_{P\text{ideal}}$, $C_{P\text{ideal}}^2$, C_T^2, and C_T

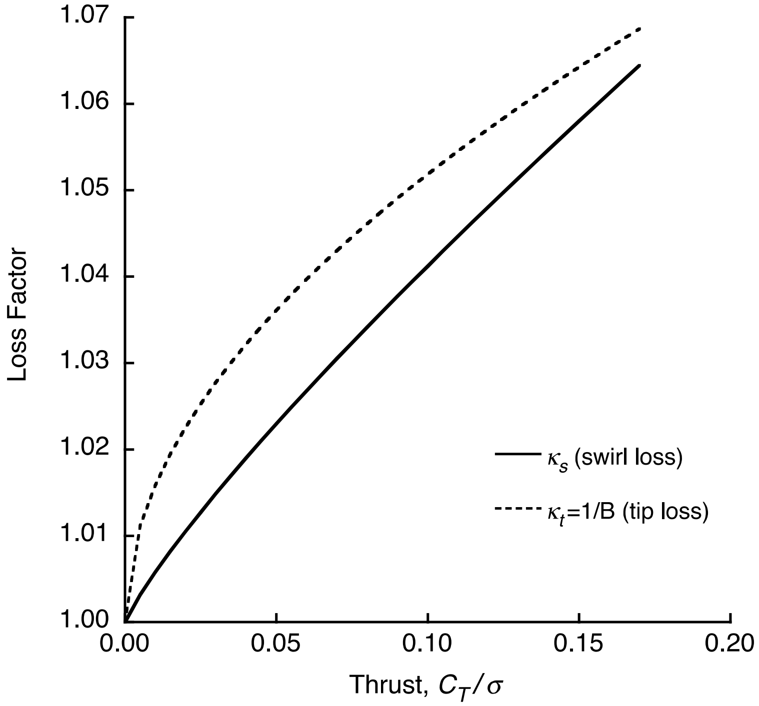

Figure 10. Swirl- and tip-loss factors versus thrust for N = 3.

Not listed in Table 4 are three special cases: a linear fit to $C_{P\text{ideal}}$, and linear and quadratic fits to $C_{P\text{ideal}}$ with swirl- and tip-loss corrections from Eqs. 2 and 3.

The uncertainty of any given curve fit can be expressed as the standard error of estimate s_e. From reference 7, the standard error of estimate is calculated as

$$s_e = \sqrt{\frac{\sum (y-\hat{y})}{k-(m+1)}} \qquad [4]$$

where y is the measured value, $\hat{y}$ is the predicted value, k is the number of data points, and m is the order of the curve fit. For fits 1–4, $y = C_P$, $k = 75$, and $m = 2$. For fits 5 and 6, $m = 3$ and $m = 4$, respectively. For each curve fit, the individual coefficients were tested for statistical significance, but their uncertainties are not otherwise critical and are not explored here.

The linear fits to $C_{P\text{ideal}}$, both with and without swirl- and tip-loss factors, all had significantly higher standard error s_e than the quadratic fit (no. 1 in Table 4). Including swirl and tip losses gave a significant improvement to s_e when compared to the linear fit without. Thus there was a hierarchy of curve fits: the linear fit to $C_{P\text{ideal}}$ had the largest uncertainty, followed by the linear fit to $C_{P\text{ideal}}$ with swirl and tip losses, then by the quadratic fit to $C_{P\text{ideal}}$; each reduction in s_e was statistically significant. Adding swirl- and tip-loss factors to the quadratic fit made only a trivial improvement. For this reason, swirl and tip losses were not further analyzed nor applied to any other curve fits.

The last three combinations in Table 4 yielded the lowest standard errors, but the trends were unrealistic at the extremes of the range of fitted data, with non-physical inflections at low thrust and sometimes at high thrust. For the last two combinations, not all coefficients were statistically significant, meaning that they were over-fitted. The last three combinations were therefore rejected. Of the remaining three, the second combination had the lowest standard error, and the first had the second lowest, but the difference was only in the fourth decimal place. The third combination fit the low-thrust, out-of-range data surprisingly well, but at the cost of a higher standard error. Of all the fits, the first combination yielded a coefficient to the $C_{P\text{ideal}}$ term closest to unity.

The difference between the standard errors of a linear curve fit to $C_{P\text{ideal}}$ (no term in $C_{P\text{ideal}}^2$) and a quadratic fit (no. 1 in Table 4) was statistically significant. However, the differences between the standard errors of any two curve fits in Table 4 were never significant. For these reasons, no further combinations were analyzed.

Swirl and tip losses should be captured by curve fits no. 3 and 2, respectively, and the second-order effects of profile power should be captured by curve fit no. 2. The least uncertainty was seen with the fit to $C_{P\text{ideal}}$ and C_T^2 (fit no. 2). However, the reduction in s_e was too small to be statistically significant, so the effects of profile power and tip losses cannot be proven here. These results do not prove that tip and swirl losses are unimportant for this rotor, or are less important than second-order effects of profile power—they all surely apply—but instead that some other source of nonlinearity is dominant.

If the requirement is to compare predictions or another data set to the data analyzed here, then the best curve fit option depends on the range of data of greatest interest. For the JVX data filtered as $C_T/\sigma > 0.04$, the fit to $C_{P\text{ideal}}$ and $C_{P\text{ideal}}^2$ is recommended because the coefficient of the $C_{P\text{ideal}}$ term should be close to one and is therefore a useful check of the validity of the fit. (A different approach was required for high-speed data, as described in the section "Wind Tunnel Data.")

The resulting equation is

$$C_P = 103.5 C_T^3 / 2 + 0.9535 C_T^{3/2} / \sqrt{2} + 0.0001956 \quad [5]$$

The associated $s_e = 0.00001309$, about 0.61 percent of the maximum measured value of C_P.

The constant term can be expressed in terms of profile power,

$$C_{P_o} = (\sigma / 8) c_{do} \quad [6]$$

Hence,

$$C_P = 103.5 C_T^3 / 2 + 0.9535 C_T^{3/2} / \sqrt{2} + 0.01375 \sigma / 8 .$$

However, the constant term includes induced-power effects in addition to profile power.

Figures 11–13 plot the data and curve fit of Eq. 5, including uncertainty bands of ±2s_e. Figure 11 plots power versus ideal power ($C_{P\text{ideal}} = C_T^{3/2}/\sqrt{2}$); bands based on the standard error with the traditional multiplier of ±2 yield the smallest metric of uncertainty that can be discerned at the scale of the plot. The uncertainty bands are a little easier to see when plotted as figure of merit versus C_T/σ (Fig. 12). The fitted curve and uncertainty bands are limited to the range of data fitted; the lighter gray line extends the fit to the limits of the plot. Although not included in the curve fit, data for $C_T/\sigma < 0.04$ $(C_{P\text{ideal}} < 0.000217)$ are included for reference.

Figure 13 plots the data as non-ideal versus ideal power. Here, it is obvious that the curve fit does not match the trend in the data at very low thrust, even though figure of merit (Fig. 12) superficially appears to be well matched. The plotted curve fit is that of Eq. 5, converted to non-ideal units (not a fit to non-ideal power).

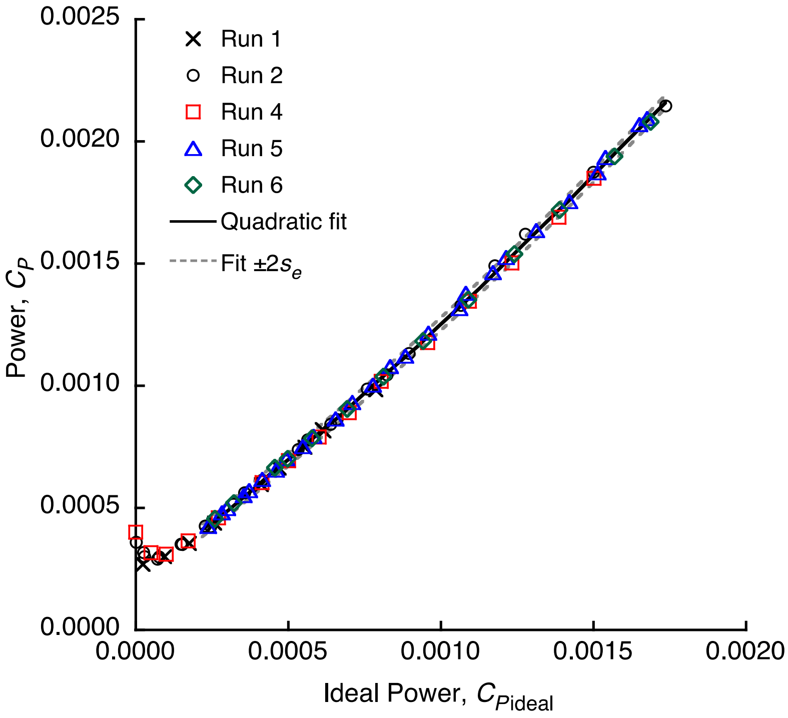

Figure 11. Quadratic curve fit of hover power (corrected for wind) versus ideal power, for $M_{tip} = 0.68$ with ±2s_e bands.

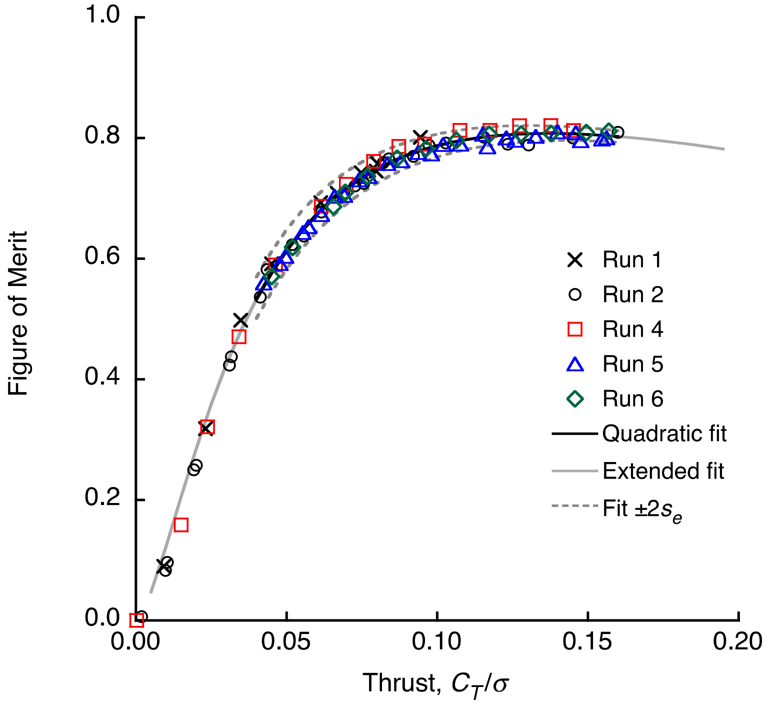

Figure 12(a). Quadratic curve fit of hover power (corrected for wind) versus thrust, converted to figure of merit, for M_{tip} = 0.68 with ±$2s_e$ bands.

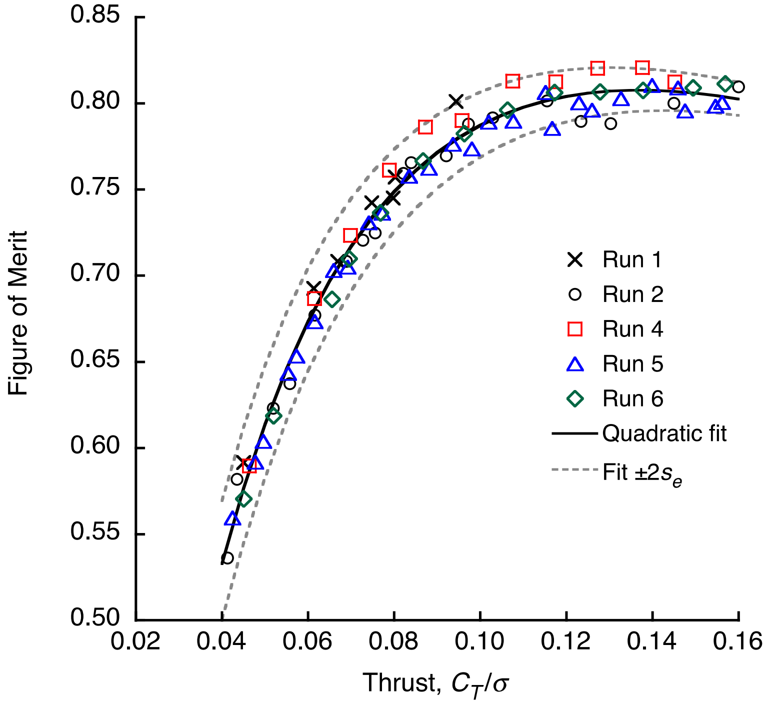

Figure 12(b). Quadratic curve fit of hover power versus thrust (expanded scales).

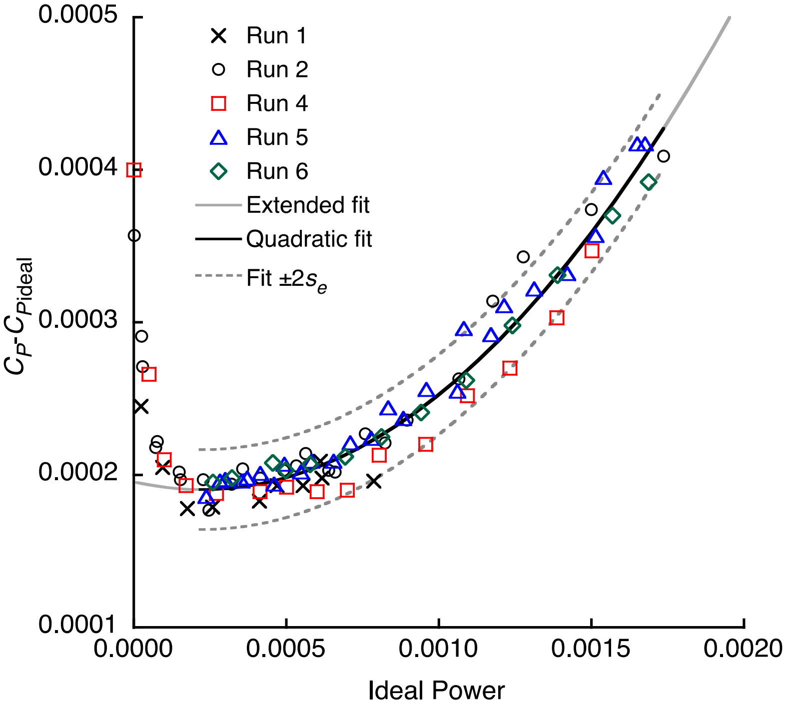

Figure 13. Quadratic curve fit of hover power (corrected for wind) versus ideal power, converted to non-ideal power, for $M_{tip} = 0.68$ with ±2s_e bands.

It may be of interest to show the curve fit with terms of $C_{P\text{ideal}}$ and C_T (combination no. 3 discussed previously). The resulting equation is

$$C_P = -0.05493 C_T^3 / 2 + 1.636 C_T + 0.02195 \sigma / 8 \qquad [7]$$

The associated $s_e = 0.00001333$.

The curve fit is plotted in Figure 14 as non-ideal versus ideal power. The trend at very low thrust is much better than in Figure 13, even though no data below $C_T/\sigma = 0.04$ are included in the fit. The choice of Eq. 5 or 7 depends on the intended use of the curve fit, although inclusion of a different range of data would doubtless be of benefit if extremely low thrust is of interest.

Because the uncertainty bands are easier to see when plotted as figure of merit or non-ideal power, all of the following comparisons of uncertainty in the hover data are made in terms of one of these two performance metrics.

Effects of Wind Corrections

An additional check on the value of wind corrections was made by applying the regression with terms in $C_{P\text{ideal}}$ and $C_{P\text{ideal}}^2$ to the same data as Figures 11–14, but without wind corrections. The results are shown in Figure 15 (compare with Figure 5 for the data set, and with Figure 12 for the curve fit). It is obvious that the wind corrections are successful in generating more consistent performance trends. Without wind corrections, the scatter, in terms of standard error, is nearly doubled: s_e = 0.0000237 versus 0.0000131. The difference between the standard errors is statistically significant.

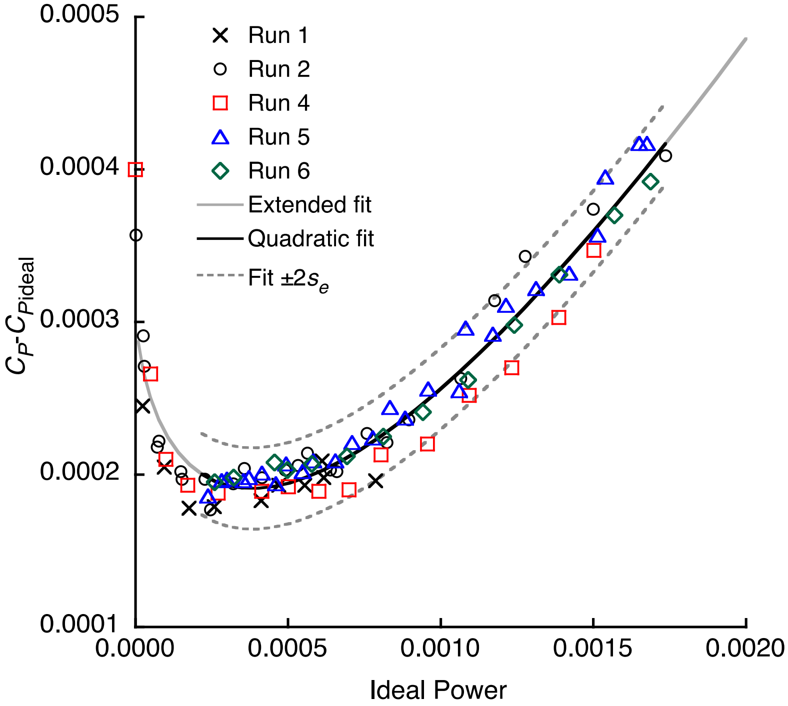

Figure 14. Alternative curve fit of hover power (corrected for wind) versus ideal power, converted to non-ideal power, for M_{tip} = 0.68.

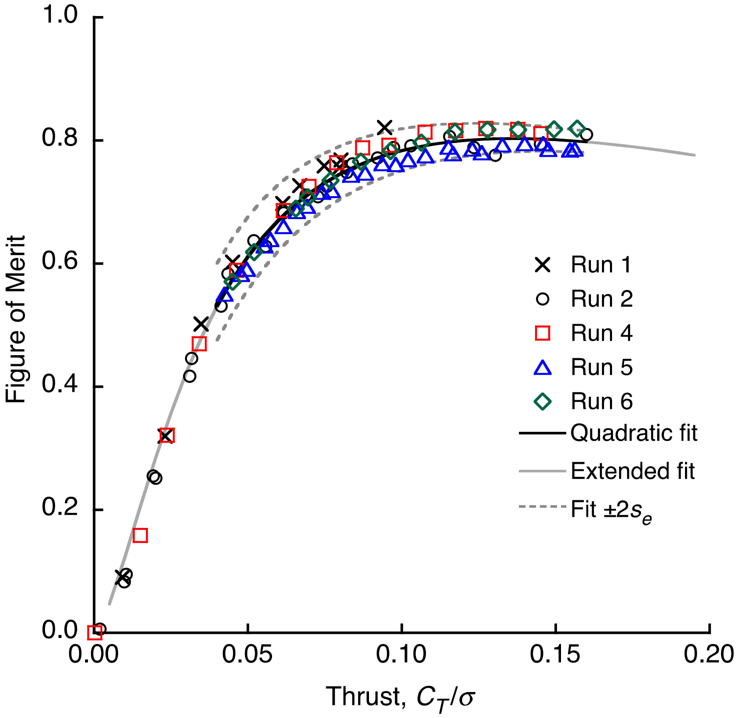

Figure 15. Quadratic curve fit of hover power (*without* wind corrections) versus thrust, converted to figure of merit, for M_{tip} = 0.68 with ±2s_e bands.

Because the power corrections of reference 1 are based on known physical phenomena, wind corrections are included in all hover data plotted and analyzed here except where explicitly noted.

Effects of Coefficient Conversions

In principle, the cleanest curve fits would be of torque Q versus thrust T, or against $T^{3/2}$. The classic performance coefficients C_T and C_P (or C_Q) include terms in atmospheric density and rotor speed (ρ and Ω), both of which are subject to measurement uncertainty. Although measurements of Ω, or equivalently V_{tip}, can be expected to be very accurate, any error will occur in the second power for C_T and C_Q, and in the third power for C_P. Power was measured as $Q \times \Omega$, hence compared with torque, power contains an additional uncertainty contributed by the measurement of Ω.

The ideal power is a fundamental characteristic of the rotor not subject to statistical error: given measured T and ρ, ideal power $P_m = T\sqrt{T/2\rho A}$ can be directly computed without introducing any additional uncertainty. The following analyses used curve fits to P_m and P_m^2, equivalent to curve fit no. 1 in Table 4.

The difference in standard errors between quadratic fits of P versus P_m and Q versus P_m is not statistically significant (all uncorrected for wind). While the fit to Q yields a lower standard error, the difference is in the third decimal place (0.0000235 versus 0.0000239, in units of C_P). A reasonable conclusion is that the uncertainty in the measurement of Ω is insignificant. The conversion of standard errors to units of C_P requires averaged values of Ω and ρ, and therefore introduces additional uncertainty, but the averaged values are the same for both conversions and do not affect the validity of the comparison. The differences are extremely small in any case.

The difference between the standard errors of quadratic fits of C_P versus $C_{P\text{ideal}}$ and of Q versus $T^{3/2}$, both uncorrected for wind and the latter scaled to C_P, differ only in the third significant figure (0.0000237 versus 0.0000242, respectively). It is obvious that conversions from physical units to rotor coefficients introduce no meaningful increase in uncertainty. These results imply that ρ and Ω were measured more accurately than T and Q, or at least that ρ and Ω had too little uncertainty to affect the curve fits.

For the purposes of this paper, the curve fits to hover data as converted to performance coefficients C_P and C_T give completely acceptable results and are perhaps easier to interpret in the context of traditional rotor performance analysis. Therefore, the remainder of this paper reports fits and comparisons in terms of C_P and C_T (or C_P/σ and C_T/σ) except where explicitly noted.

Considerations for Off-Trend Data

There are several physical reasons why C_P/σ would not exactly follow the $C_T^{3/2}/\sqrt{2}$ trend line including, but not limited to, profile power, stall at high collective settings, and variations in the lift distribution, which will rarely if ever approach the ideal. The JVX hover tests never achieved full stall. A few other possibilities are briefly explored here.

The JVX rotor has very high total twist (–47.5 deg nominal). As the total thrust approaches zero, the tip experiences negative lift to cancel out residual positive lift at the root. Induced power may then increase as thrust further decreases, even without stall. Under such conditions, the rotor no longer behaves like an actuator disk of radius R, and Eq. 1 is not appropriate. Figure 3 shows a trend reversal at about $C_T/\sigma = 0.02$.

The design lift distribution is necessarily a compromise, but for a well-designed rotor, the lift distribution will yield minimum non-ideal induced power near the design C_T, with higher non-ideal power at lower and higher C_T. However, the JVX twist distribution must work in high-speed axial flow, and therefore varies greatly from the ideal for hover. The effect of non-ideal lift distribution can be significant, and minimum induced power may not occur exactly at design C_T. The JVX design C_T is well above the mid-thrust data, where non-ideal power is increasing rapidly (Fig. 13).

In hover, profile power is dominated by rotational velocity, not thrust, and the JVX twist is large enough (–47.5 deg) that the root and tip cannot simultaneously operate in the unstalled regions of their respective airfoils. Three-dimensional (3D) stall delay may mitigate this effect but cannot achieve an ideal lift distribution. Given a large enough data set, with large variations in thrust, tip speed, and axial velocity, it might be possible to separate the effects of profile power from those of twist distribution, but not with the existing JVX data.

The close quadratic fit to ideal power (Eq. 5 and Figs. 11–13) does not prove that the variations from the ideal power trend are caused by variations in lift distribution, or indeed by any other particular physical mechanism, but it is plausible and consistent with the data. The larger point is that a quadratic curve fit to ideal power gives a very close fit to the data, and the resulting estimate of uncertainty is unlikely to be usefully reduced by any reasonable set of physical or mathematical assumptions.

Uncertainty Comparisons for Hover

The PTR measures thrust and torque with a combination of a rotor balance and an instrumented flex coupling on the rotor shaft (refs. 1 and 11). The documentation for the JVX OARF test has incomplete data for measurement uncertainty. The balance was bench-calibrated prior to installation, and check loads were applied afterwards to determine the as-installed accuracy, including corrections for known interactions. Torque/thrust interactions proved problematical for the Phase II wind tunnel data and are discussed in context later in this report. There was no evidence of problems with interactions during the OARF test.

Reference 11 states that thrust is measured within ±50 lb up to the maximum range of 16,000 lb, and torque is measured within ±10 ft-lb with a maximum range of 21,000 ft-lb. Reference 1 states that check loads applied during the JVX tests revealed thrust and torque accuracies of ±200 N and ±70 Nm, respectively. The ±200 N accuracy is consistent with ±50 lb, but ±70 Nm is decidedly greater than ±10 ft-lb.

There is scant documentation of how uncertainties for balance and shaft instrumentation were determined and combined to generate the stated measurement accuracies. The given values of accuracy—the terminology used in the references—appear to be the greatest excursions from the nominal values, not the standard deviations from the mean, root mean square, or other metric. The accuracies are given to one significant figure, with likely but unknown round-off errors from conversion between English and S.I. units.

Data plots in reference 11 imply that much of the uncertainty in both thrust and torque is hysteresis, which possibly would be physically averaged out by vibration during a data point, but there is no way to prove that assumption. See Appendix B for further discussion of balance uncertainties.

For the following analysis, the accuracies given in reference 1 are taken at face value, but converted to English units of ±50 lb thrust and ±50 ft-lb torque (hence a slight rounding up in thrust, consistent with reference 11). It is further assumed that the given values of accuracy are twice the standard deviations, giving measurement uncertainties of 25 lb thrust (σ_T) and 25 ft-lb torque (σ_Q).

Figure of merit can be written in terms of the directly measured quantities T and Q as

$$FM = \left(T\sqrt{T/2\rho A}\right)\Big/Q\Omega \ .$$

Assuming that ρ and Ω do not contribute significantly to the total uncertainty, the uncertainty in figure of merit, expressed as σ_{FM}, can be estimated as

$$\sigma_{FM}^2 = \frac{T}{Q^2\Omega^2 2\rho A}\left(\frac{9}{4}\sigma_T^2 + \frac{T^2}{Q^2}\sigma_Q^2\right) \tag{8a}$$

or

$$\sigma_{FM}^2 = FM^2\left(\frac{9}{4}\frac{\sigma_T^2}{T^2} + \frac{\sigma_Q^2}{Q^2}\right) \tag{8b}$$

Figure 16 plots the curve fit of Figure 12 but with $\pm 2\sigma_{FM}$ uncertainty bands, here at expanded scales to match Figure 12 (b). At $C_T/\sigma = 0.10$, the thrust term in Eq. 7 contributes about three times to the uncertainty σ_{FM}^2 as the torque term. The estimates of balance measurement uncertainties used here are very rough. The check loads data in reference 11 suggest that the error in thrust measurement is much reduced over the range of data analyzed here; further reductions in measurement error may be assumed if hysteresis is averaged out over each data point. On the other hand, thermal effects and uncorrected interactions could increase the measurement errors. Nevertheless, it is clear that the uncertainty bands in Figure 12 (b) are larger than those contributed by the balance and shaft instrumentation. See also the discussion of airfoil drag in the next section of this report.

Other measures of uncertainty are available, such as the confidence interval, which characterizes the dispersion of the regression line, and the prediction interval, which is the uncertainty in the prediction of a given data point; both of these metrics account for the increase in uncertainty with distance from the mean value of the independent variable (ref. 8). Figure 17 plots these metrics in the same format as Figure 12. The prediction interval (P.I.) is comparable to the $\pm 2s_e$ uncertainty bands, while the confidence interval (C.I.) is much smaller. The data transformation from power to figure of merit inverts the usual spread of the prediction interval about the mean regression line, in that the spread is greatest at mid-thrust and decreases at the ends of the range of thrust. The spread in the confidence interval increases slightly at maximum thrust, as can just barely be discerned in Figure 17.

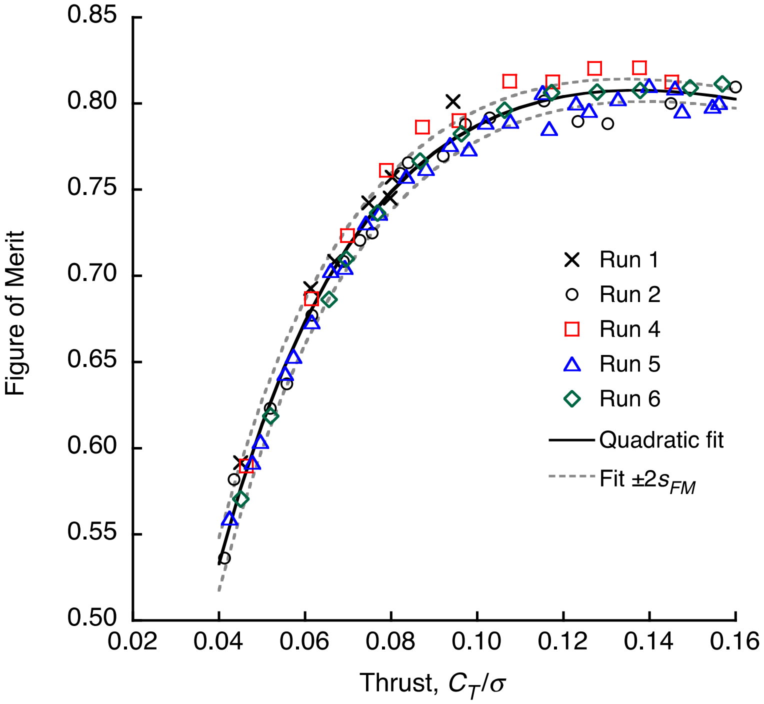

Figure 16. Quadratic curve fit of hover power (corrected for wind) versus thrust, converted to figure of merit, for $M_{tip} = 0.68$ with $\pm 2\sigma_{FM}$ bands.

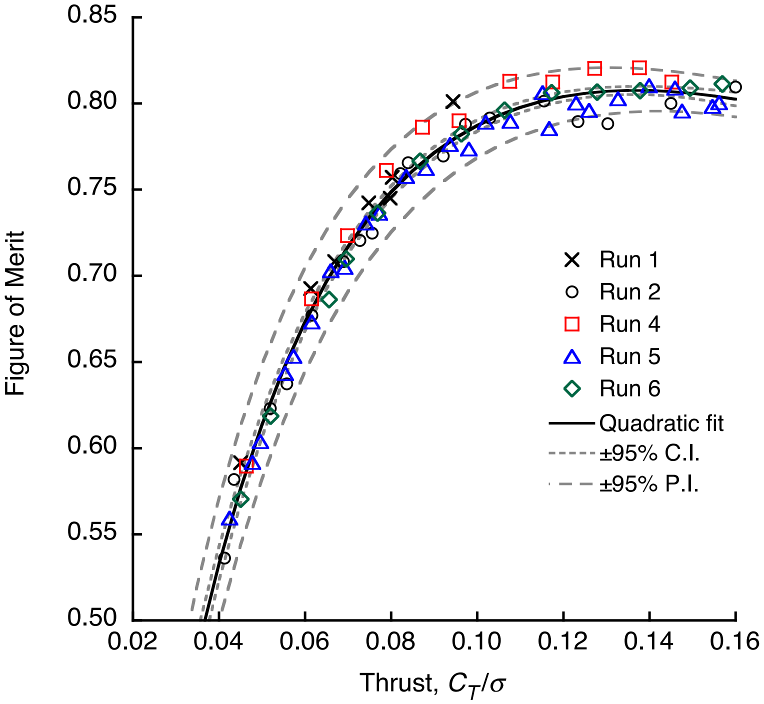

Figure 17. Quadratic curve fit of hover power (corrected for wind), converted to figure of merit versus thrust, with confidence and prediction intervals, $M_{tip} = 0.68$.

Uncertainties in Airfoil Drag

The focus of this report is the JVX OARF and wind tunnel data, which are used to validate predictive methods such as CAMRAD II (ref. 20). Other sources of measurement uncertainty, namely experimentally determined airfoil data, are also relevant and are briefly explored here to illustrate their importance relative to the JVX test data.

CAMRAD II relies on external airfoil tables for aerodynamic analysis. An inflow model—here a free-wake model—computes the local aerodynamic environment of each blade section, and values of lift, drag, and pitching moment read are from the tables to determine the section loads. It was conjectured that uncertainties in airfoil drag data might explain the mismatch between CAMRAD II predictions of high-speed performance (refs. 4 and 5), so estimates of airfoil drag uncertainty were generated and converted to equivalent performance uncertainty. Although airfoil drag has less effect on rotor performance in hover than at high speed, the statistical comparisons for hover are nevertheless revealing. Furthermore, the XN-series airfoil data were determined experimentally, so comparing the two types of uncertainty—two-dimensional (2D) airfoil section data versus rotor performance data—provides useful insight into the relative importance of different sources of uncertainty. An important caveat is that the uncertainties in airfoil data were estimated by indirect means, as described next.

The statistical comparison was derived from the results reported by Bousman (ref. 21). Extending the work of McCroskey (ref. 22), Bousman calculated variations in airfoil performance as measured in several different wind tunnel tests. The SC1095 and SC1094 R8 airfoils were chosen, largely because of the availability of data from 10 different tests. Although no equivalent variety of test data exists for the XN-series airfoils used on the JVX rotor, the SC-series airfoils and test data are of similar vintage to those of the JVX airfoils. Therefore, the uncertainty in the airfoil characteristics analyzed by Bousman should be similar to what would be expected if an equivalent series of wind tunnel tests were carried out for the JVX airfoils.

For a well-designed rotor operating below stall, the airfoil characteristic critical for hover is c_{d_0}, the section drag coefficient at zero lift. Its effect on figure of merit may be estimated by adjusting total power by the estimated profile power, Eq. 6:

$$C_{P_o} = (\sigma/8)c_{d_o}\,.$$

The uncertainty in measured c_{d_0} may then be compared to the uncertainty in measured figure of merit by substituting the standard deviation of c_{d_0} into Eq. 6 to get ΔC_{Po}, then plotting

$\Delta FM = \dfrac{C_T^{3/2}/\sqrt{2}}{C_P \pm 2\Delta C_{P_o}}$, where $\pm 2\Delta C_{Po}$ is used for comparison to $\pm 2s_e$ of the curve fit to the data (Eq. 5).

The SC1095 airfoil was taken as an appropriate surrogate for the JVX airfoils (the SC1094 R8 has nose droop not present in the JVX airfoils). To avoid contaminating the uncertainty measure with drag-divergence effects, only data below Mach 0.7 were used. Furthermore, the "Experiment 4" data were deleted because they have a clearly different trend (Figure 31 of reference 21). The uncertainty in c_{d_0}, computed as the standard deviation, was thereby determined to be 0.000872; the equivalent variation in figure of merit is plotted in Figure 18 with the usual multiplier of ±2.

Whereas the c_{d_0} uncertainty band in Figure 18 was derived from airfoil data, the JVX rotor has a fixed but unknown value of c_{d_0} at any given test condition. The fact that c_{d_0} is unknown does not contribute to uncertainty in measurements of rotor performance. The $s_d(c_{d_0})$ uncertainty band is, therefore, an indicator of prediction uncertainty arising from imperfect knowledge of isolated airfoil performance. In contrast, the s_e uncertainty band characterizes the experimental measurement of JVX rotor performance. It is almost certainly a coincidence that both uncertainty bands are nearly the same magnitude.

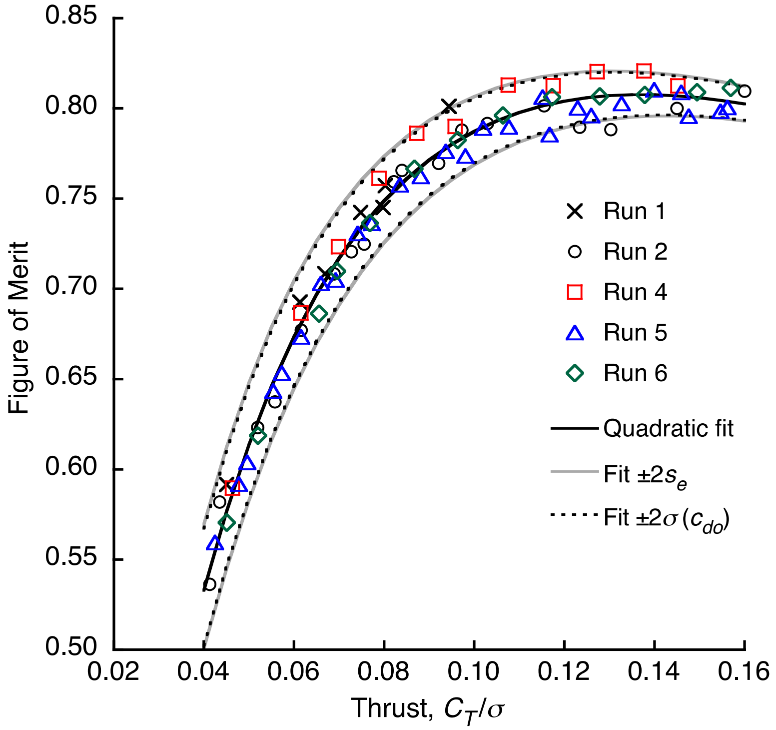

Figure 18. Quadratic curve fits of hover power, converted to figure of merit versus thrust, with ±2s_e bands and ±2s_d (c_{d_0}) bands.

The value of uncertainty in c_{d_0} given here is much larger than that reported in reference 23 for low-drag conditions. Reference 23 gives uncertainties for a single wind tunnel (at Penn State University), whereas reference 21 gives pooled uncertainties for 10 wind tunnels, none the same as that of reference 23. The JVX airfoil tables were generated from data taken in a yet another wind tunnel (the Boeing Supersonic Wind Tunnel, ref. 10).

The uncertainty of c_{d_0} determined as described for the SC1095 airfoil is only an approximation. A logarithmic curve fit to the data, as suggested in reference 21 to account for Reynolds number, would have yielded a standard error of fit slightly less than the standard deviation about the mean. On the other hand, including “Experiment 4” data would have increased the standard deviation. The exact value of the standard deviation would also have been affected by choosing a different maximum Mach number. Finally, multiple tests of the JVX airfoils would doubtlessly have yielded further differences. The larger point, however, is that airfoil drag alone can contribute uncertainty to *predicted* rotor performance of similar magnitude as the uncertainty in *measured* performance.

Were the JVX rotor to have been driven into stall, maximum section lift c_{lmax} would have also provided a useful statistical comparison. Because of the highly nonlinear behavior that is characteristic of stall, there is no simple estimate of the effect of c_{lmax} on power corresponding to Eq. 6. An indirect estimate may be made with a rotor performance code by modifying the airfoil tables, or perhaps by repurposing a stall-delay model to adjust the section lift by the uncertainty in c_{lmax}. The latter approach was carried out with CAMRAD II, using the SC1095 statistics of reference 21, but the effect was negligible within the range of test C_T/σ (hence not shown here).

Hover Data for M_{tip} = 0.73

A limited amount of hover data were taken at M_{tip} = 0.728. Run 7 included two separate thrust sweeps, labeled Run 7A and 7B in Figure 19. Three additional data points were taken in Run 8, but at M_{tip} = 0.724. All data in Figure 19 have been corrected for wind. The maximum wind speed for Run 7 was 3.0 knots, but the wind speed for Run 8 was 3.6 to 4.5 knots. Because of the higher wind speed and slightly lower tip speed, the Run 8 data were not used in any further plots or analyses.

Figure 20 plots the M_{tip} = 0.73 data (Run 7) against the data for M_{tip} = 0.68 (the same data as in Figure 12). Here, all data at a given M_{tip} have the same symbol. Also shown are ±$2s_e$ uncertainty bands for the M_{tip} = 0.68 data (also the same as Figure 12). The data taken at the higher tip speed rarely fall outside of the uncertainty bands and then only at high thrust.

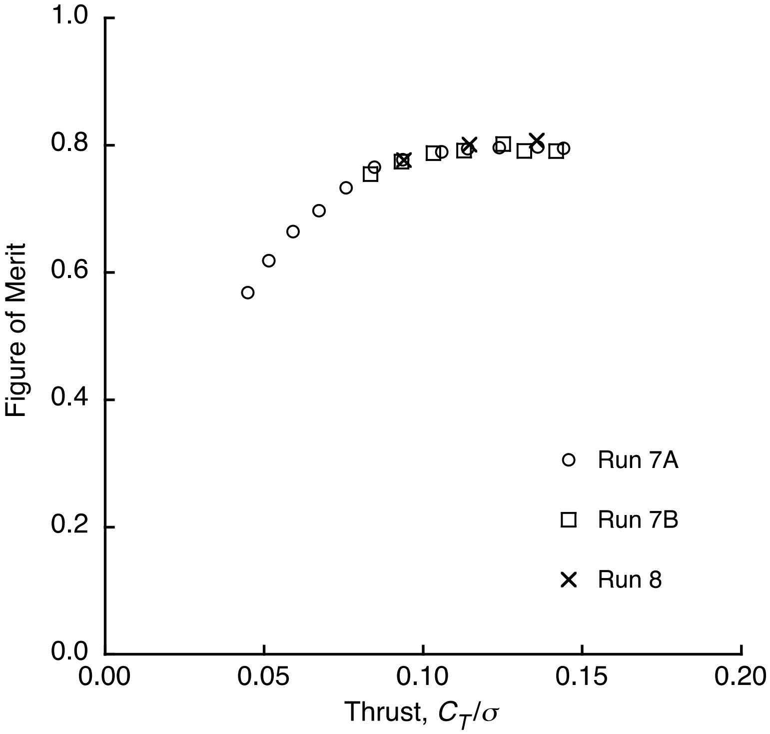

Figure 19. Figure of merit (corrected for wind) versus thrust, M_{tip} = 0.73.

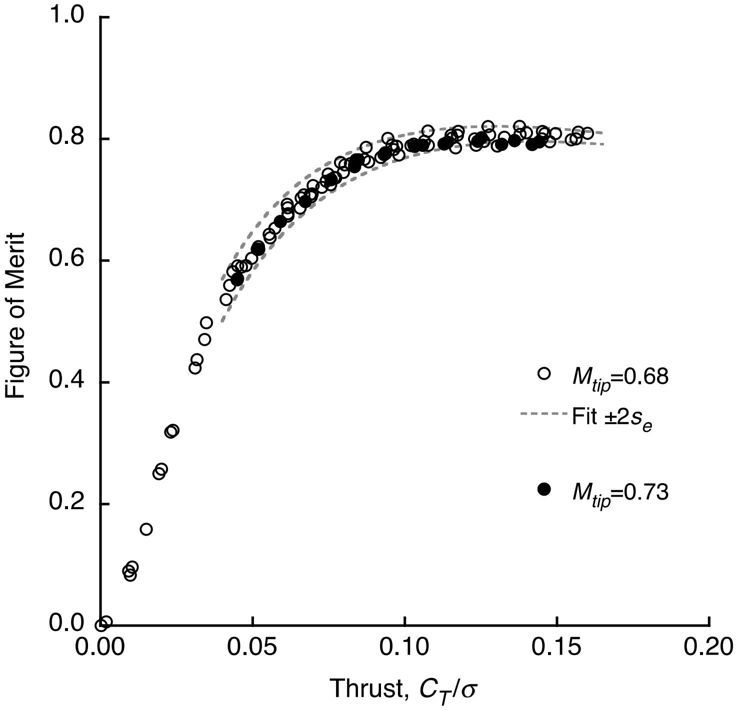

Figure 20. Figure of merit (corrected for wind) versus thrust for $M_{tip} = 0.73$ and $M_{tip} = 0.68$, with ±2s_e bands for $M_{tip} = 0.68$.

Figure 21 shows a quadratic curve fit to ideal power, with $\pm 2s_e$ uncertainty bands. The fit is directly equivalent to that of Figure 12 and Eq. 5 for $M_{tip} = 0.68$. The fitted equation for $M_{tip} = 0.73$ is

$$C_P = 144.8C_T^3/2 + 0.9037\,C_T^{3/2}/\sqrt{2} + 0.01493\sigma/8 \tag{9}$$

The associated $s_e = 0.00000533$, about 0.28 percent of the maximum measured value of C_P. The uncertainty is less than half that for $M_{tip} = 0.68$ (Eq. 5); the difference in standard errors is statistically significant. However, the range of thrust is narrower and there are fewer repeated runs. A run-by-run comparison would likely yield different results, but without an explicit understanding of the reasons for the higher scatter at the lower tip speed, definitive conclusions would be elusive. The results presented here accordingly do not prove that the data at $M_{tip} = 0.73$ are somehow better than the data at $M_{tip} = 0.68$, although the former may be more pleasing to look at. Figure 22 replots the data as non-ideal versus ideal power (compare to Figure 13).

Reference 1 includes an even smaller data set at $M_{tip} = 0.60$. There was only one thrust sweep, hence limited scope for examining repeatability and uncertainty. Accordingly, the data at $M_{tip} = 0.60$ are not examined here.

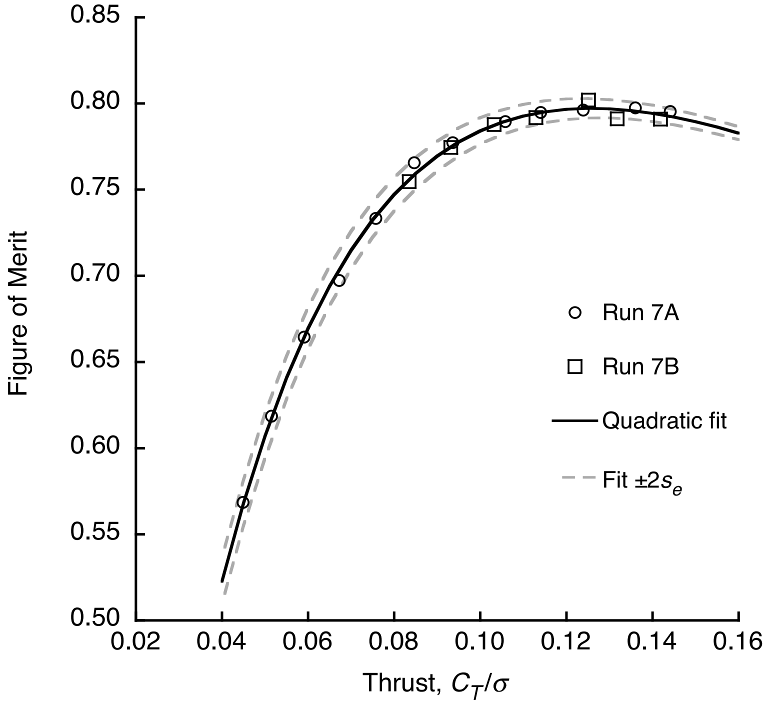

Figure 21. Quadratic curve fit of hover power (corrected for wind) versus thrust, converted to figure of merit, for $M_{tip} = 0.73$ with ±2s_e bands.

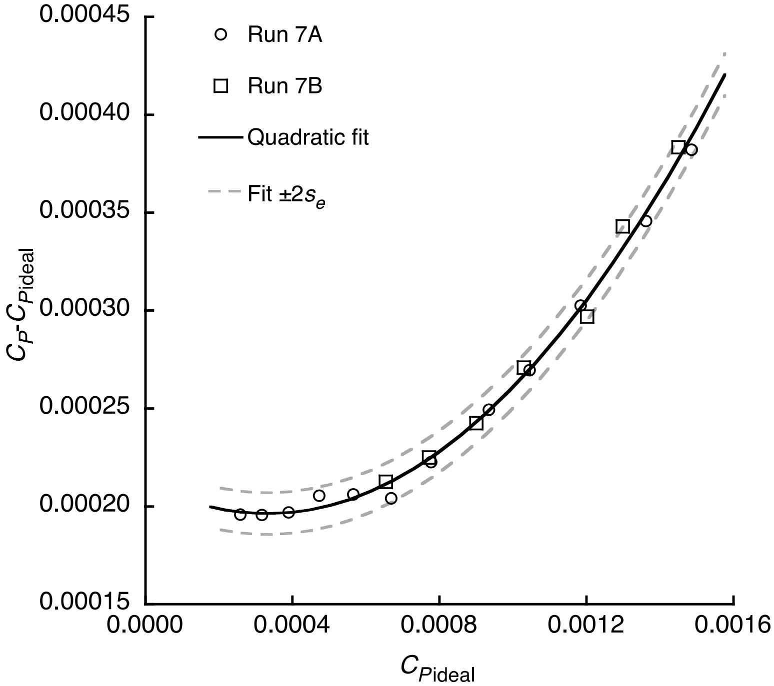

Figure 22. Quadratic curve fit of hover power (corrected for wind) versus ideal power, converted to non-ideal power, for $M_{tip} = 0.73$ with ±2s_e bands.

CAMRAD II and U^{2}NCLE Predictions for Hover

With analyses of hover performance data in hand, meaningful evaluations of the accuracy of performance predictions can be made. References 4 and 5 presented CAMRAD II predictions of hover performance compared with selected JVX test data (wind <1 knot). The predictions were updated and plotted here against the expanded hover data set described previously. Plots of figure of merit versus thrust are preferred here because they emphasize the magnitude of any mismatch to the data, thus highlighting any differences.

Inflow Models

Figure 23 plots CAMRAD II predictions made using four different aerodynamic models: uniform inflow, blade element/momentum theory (BEMT), rolled-up free wake (single-tip vortex), and multiple-trailer wake (two outboard vortex trailers). Figure 23 also includes U^{2}NCLE computational fluid dynamics (CFD) predictions (kindly provided by Dr. Chunhua Sheng). The CAMRAD predictions are essentially the same predictions as reported in reference 5, but plotted here against an expanded data set; the models are described in detail in reference 20. The uniform-inflow model used an induced velocity factor $\kappa = 1.10$, and the BEMT model used $\kappa = 1.04$. (In this context, the induced velocity factor is equivalent to the induced power factor $C_{Pi}/C_{P\text{ideal}}$.) BEMT is implemented in CAMRAD as a differential-momentum model and includes the Prandtl tip-loss correction (Eq. 3). The wake models used second-order lifting-line theory for the aerodynamic collocation points. CAMRAD used a 3D stall-delay model, discussed in the next section. The U^{2}NCLE predictions used the Spalart-Allmaras detached eddy simulation (DES) model (ref. 6).

To better reveal detail, Figure 24 is a simplified and rescaled version of Figure 23, but with $\pm 2s_e$ uncertainty bands from Eq. 5 instead of individual data points (the same as Figures 11–13). The uncertainty bands terminate at $C_T/\sigma = 0.16$, the limit of measured thrust, beyond which the validity of the curve fit becomes questionable.

The multiple-trailer predictions match the data very well and always fall within the $\pm 2s_e$ bands, at least within the limit of measured thrust. The BEMT predictions are almost as good, and exceed the uncertainty bands only at very high and low thrust where there are relatively few data points to define the local trends. The uniform-inflow model is nearly as good as the BEMT model above $C_T/\sigma = 0.06$, but falls below the measured data shortly below that thrust value. The uniform-inflow and BEMT models each required a different empirical induced velocity factor κ to match the data, so the good results do not indicate robust models. The BEMT predictions, for example, can be better matched to the data at high thrust by slightly increasing κ, but will then have a worse match at medium thrust. There is ample reason to believe that a wake model or CFD is required for a good fit to the data.

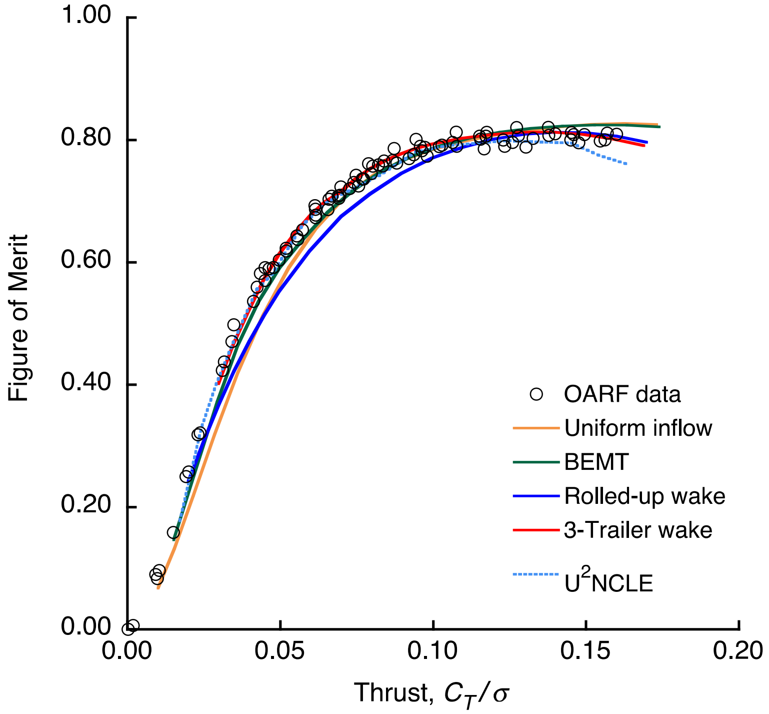

Figure 23. CAMRAD II predictions of JVX figure of merit with five aerodynamic models, compared with OARF test data.

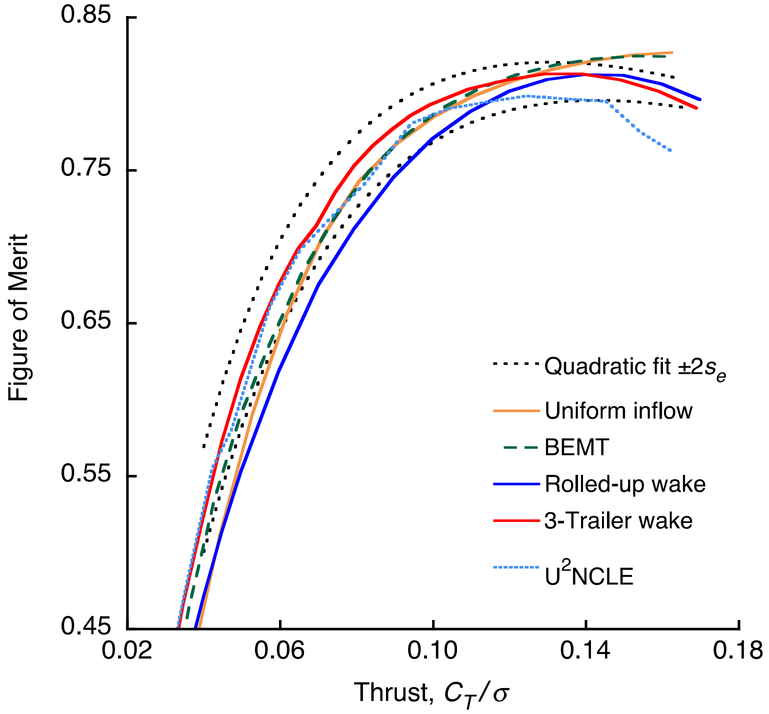

Figure 24. CAMRAD II predictions of JVX figure of merit with five aerodynamic models, compared with test data uncertainty. The $\pm 2s_e$ bands are for the quadratic curve fit (Eq. 5).

The most surprising result is the relatively poor accuracy of the conventional rolled-up wake model. It exceeded the ±2s_e uncertainty bands more than any other model, although the trend of figure of merit at high thrust is better than either of the simpler models and matches the trend of the multiple-trailer model. The rolled-up model plotted here used a second-order lifting-line model for the blade aerodynamics (inner solution, see reference 20). The second-order model improved the match to data at high thrust, compared to the first-order model used in references 4 and 5. However, figure of merit is still underpredicted at low-to-medium thrust.

Considerable effort was put into refining the rolled-up wake model, but with little useful improvement to the predictions. Adjusting the radial location of the tip vortex, fraction of peak circulation entrained in the tip vortex, extent of initial wake convection, and other measures resulted in either small or inconsistent improvements. The only measure that made for a general improvement over a large range of thrust conditions was to reduce section c_d by 0.002, which is a lower value of drag than expected. However, the JVX rotor was cleaned every day and operated only in low wind, so it is possible that some degree of laminar flow was achieved. The airfoil tables used by CAMRAD did not include this effect (assuming it did indeed exist).

Figure 25 shows CAMRAD predictions with nominal drag and with all values of section c_d reduced by 0.002. The results are consistent with laminar flow at low thrust, changing to turbulent flow at high thrust. However, the multiple-trailer wake also gave good results at low thrust with nominal drag. The existence of laminar flow remains speculative. A constant reduction in c_d, independent of both radius and thrust, is too crude an adjustment to constitute a reliable model.

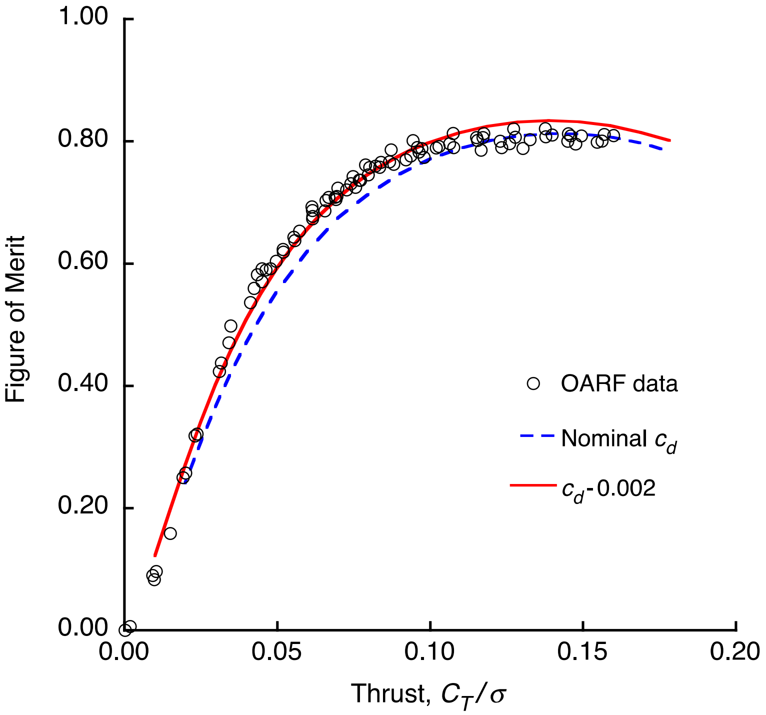

Figure 25. CAMRAD II predictions of JVX figure of merit with nominal and reduced section c_d, compared with OARF test data.

Wake models need semi-empirical inputs such as core size, tip vortex radial location, etc., but once such parameters are established, wake models typically give good results over a wide range of operating conditions. The simpler models, notably BEMT, are much more computationally efficient than the wake models, and in this implementation proved more computationally robust. The multiple-trailer model in particular had major problems with convergence at very low thrust.

Although more accurate than the rolled-up wake model, the multiple-trailer model requires an additional parameter: the radial location of the additional trailer. The model used here had a trailer at $0.8R$, which Figures 23 and 24 show to be completely adequate. The predictions were little affected by variations in trailer location from 0.7 to $0.9R$. The multiple-trailer model received much further tuning of various convergence parameters, but with little net effect on computational efficiency or accuracy. The multiple-trailer model has not proven robust for other rotors and is no longer being developed.

Finally, the U^{2}NCLE CFD predictions match the data nearly as well as the multiple-trailer model, except at high thrust where U^{2}NCLE prematurely predicts stall. Given that the CFD predictions required far fewer empirical parameters, the achievement is quite impressive.

Stall-Delay Models

Reference 5 presents results for three different, 3D stall-delay models: the "Bell" model (ref. 24), the "Selig" model (ref. 25), and no stall delay. Those analyses were repeated, always using the multiple-trailer wake model, and are plotted in Figure 26 against the uncertainty bands from Eq. 5. It is evident that a stall-delay model is necessary at high thrust; it is also evident that the difference between the Bell and Selig models is much less than the uncertainty in the test data, except at low thrust where numerical problems begin to appear (off-scale in Figure 26). The near-coincidence of results of using the different stall-delay models is not surprising because they both incorporate empirical adjustments. Aside from Fig. 26, all CAMRAD predictions shown here used the Selig stall-delay model.

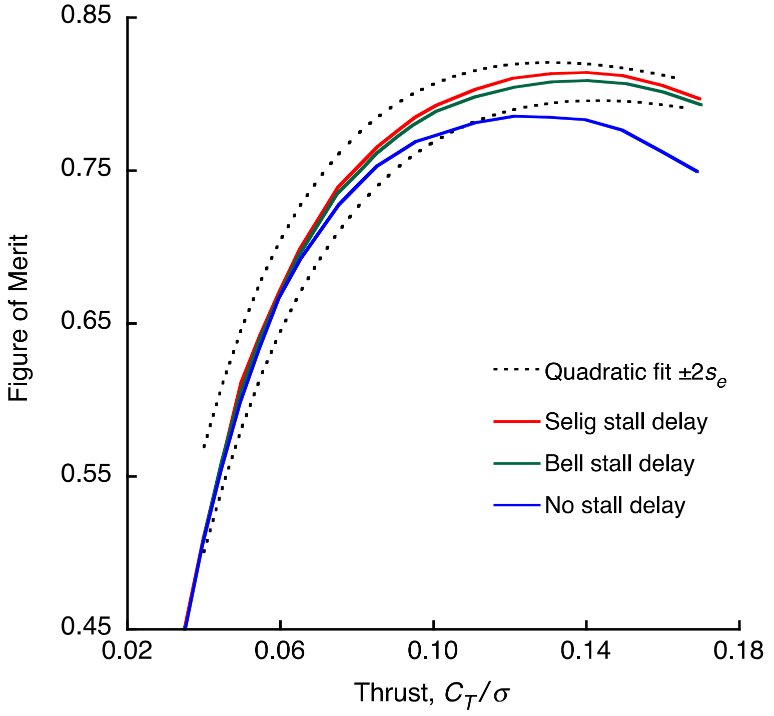

Figure 26. CAMRAD II predictions of JVX figure of merit with three stall-delay models. The ±2s_e bands are for the quadratic curve fit to data (Eq. 5).

Reynolds Number Corrections

The CAMRAD II aerodynamic model relies on externally supplied airfoil tables and optionally provides for corrections for Reynolds number effects. The airfoil tables used here were derived from 2D wind tunnel tests of full-scale V-22 airfoils (ref. 10). At 0.656 scale to the V-22, the JVX rotor should experience minor Reynolds number effects. Nevertheless, the CAMRAD II multiple-trailer model was run separately with corrections for turbulent flow, laminar flow, and no correction.

From references 20 and 26, the corrections are implemented as

$$c_d = \frac{1}{K_D} c_{d\,2D} \qquad [10a]$$

$$c_l = K_L c_{l\,2D}(\alpha / K_L) \qquad [10b]$$

where $K = (\mathrm{Re}/\mathrm{Re}_t)^n$.

The 2D coefficients are those given in the airfoil tables. Here, $K_D = K_L$, and $n = 0.2$ (turbulent), 0.5 (laminar); or 0 (no correction). The results are plotted in Figure 27, which shows that while the differences are detectable, they are less than the uncertainty in the test data, except at very low thrust where convergence problems begin to dominate (off-scale in Figure 27). Corrections for turbulent flow (n = 0.2) were used for all CAMRAD analyses unless explicitly noted otherwise.

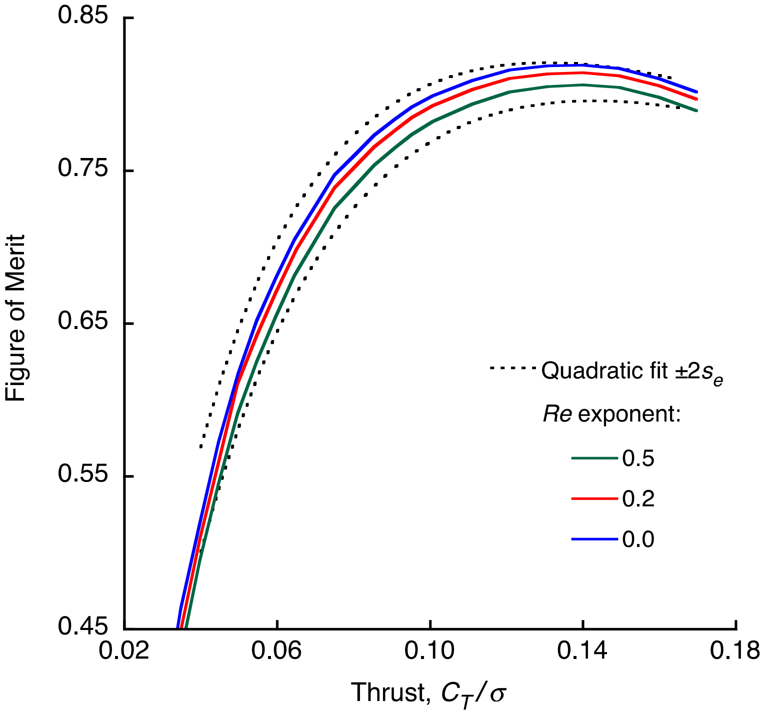

Figure 27. CAMRAD II predictions of JVX figure of merit with three Reynolds number correction models. The $\pm 2s_e$ bands are for the quadratic curve fit to data (Eq. 5).

Wind Tunnel Data

The wind tunnel tests used the same rotor and test stand as the hover tests, but with a revised cuff on the inboard section of the blade, nearest the spinner (Fig. 2). The same rotor balance was used for the wind tunnel tests as for the hover tests. There is no reason to suspect that conversion from physical units to rotor coefficients would introduce any changes to the statistics worse than those in the hover data. Therefore, the analyses of wind tunnel data were usually done in terms of rotor coefficients.

Crosswind corrections do not apply to the wind tunnel data. The nonlinearities seen at very low hover thrust data are not evident in the wind tunnel data and would not be expected for such test conditions (minimum speed, 99 knots). Therefore, the process for deleting non-representative data was not needed for the wind tunnel data.

The Phase II data presented here differ from those reported in references 4 and 5 in two ways: different spinner drag tare corrections are used, and the thrust is recomputed without any adjustment for torque/thrust interaction. An effective spinner drag area of 0.901 ft^2 was applied to the balance data to generate net rotor thrust. Deleting the torque/thrust interaction gave results that matched the Phase I data.

A summary of the Phase II rotor performance data is presented first, including CAMRAD II predictions. Discussions of spinner tares and torque/thrust interaction follow, including selected Phase I performance data. Next is a deeper look at rotor performance, including data consistency and regression analyses. The discussion of wind tunnel data closes with a comparison of CAMRAD II predictions to those of U^2NCLE, an independent CFD analysis.

More detailed discussions of spinner tares, including the (unsuccessful) use of internal pressure data, are included in Appendix B. Justification for rejecting the recommendations of reference 2 are also included.

A simple analysis of wind tunnel blockage effects is given in Appendix C. The effects are small for the range of operating conditions reported here. No corrections for blockage are used elsewhere in this report.

Numerical tables of the data presented in this report are included in Appendix D.

Summary Rotor Performance Data

The 40x80 wind tunnel airplane-mode data were taken at several different tunnel wind speeds but only two tip speeds. The JVX rotor tests typically varied thrust at a fixed tunnel speed and rotor tip speed. The resulting data group into five speeds, from $\mu = 0.263$ to $\mu = 0.562$, listed in Table 5. All data at $\mu = 0.523$ and below were taken at about 487 rpm, but the data at $\mu = 0.562$ were taken at 531 rpm. There were no data points at the same tunnel speed but different tip speeds.

The JVX airplane-mode data are plotted as propulsive efficiency η versus thrust C_T/σ in Figure 28. No single advance ratio μ has data that span the full range of thrust. In Figure 28, the data points are offset in C_T/σ by multiples of 0.01 to make the trends easier to see. CAMRAD II predictions of rotor performance are also plotted. The same data are plotted in Figure 29 as power C_P/σ versus C_T/σ, here without any plotting offsets. The data use a spinner drag tare of 0.901 ft^2 and do not include any torque/thrust interaction corrections. The justifications for using the stated spinner tare and for omitting the torque/thrust interactions are discussed at length following the summary data plots.

Table 5. Mean test conditions for JVX wind tunnel data, with standard deviations. V_{tip} and M_{tip} are nominal hover values.

μ	Ω (rpm)	V_{tip} (ft/sec)	M_{tip}	V (knots)	$s_d(\mu)$	$s_d(V_{tip})$ (ft/sec)	$s_d(V)$ (knots)
0.210	487	638	0.57	99	0.0009	1.9	0.4
0.349	489	640	0.58	132	0.0009	1.7	0.5
0.438	489	641	0.58	166	0.0015	2.0	0.4
0.523	491	642	0.58	199	0.0018	1.9	0.3
0.562	531	695	0.63	231	0.0007	1.1	0.2

The CAMRAD predictions in Figures 28 and 29 used a free-wake model equivalent to the rolled-up model used for hover (Figs. 23–27). Three-dimensional stall delay is not important at the low blade-lift coefficients typical of airplane mode at high speed, so no stall-delay model was used. The multiple-trailer model was not considered here, because blade-vortex interaction does not occur in high-speed axial flow, even at low thrust. There is, therefore, no advantage to be gained from higher-order wake models. The CAMRAD analysis used airfoil section drag coefficients adjusted by −0.002. The drag adjustment is discussed in a later section, Additional CAMRAD II Predictions. That section also compares CAMRAD with U^{2}NCLE predictions.

Reference 15 reported higher values of propulsive efficiency for the XV-15 rotor. However, the XV-15 had 22 percent lower solidity than the JVX rotor and was operated at tip speeds as low as 400 ft/sec (compare Table 5). Both of these differences should substantially improve propulsive efficiency.

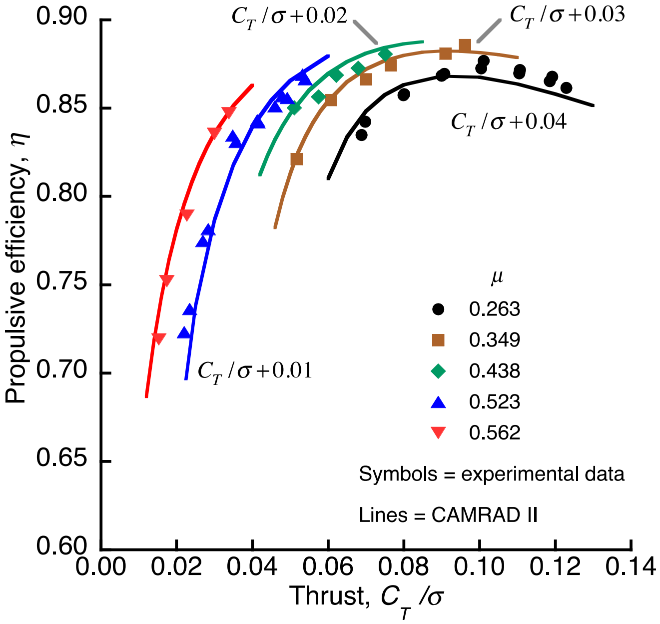

Figure 28. Measured JVX rotor propulsive efficiency from the NFAC Phase II test.

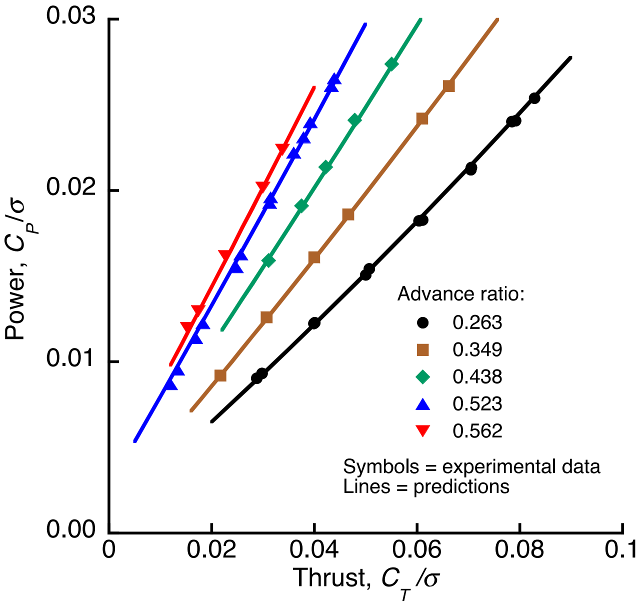

Figure 29. Measured JVX rotor power from the NFAC Phase II test.

JVX Spinner Tares

This section documents the selection of a recommended value of JVX spinner drag tare. See Appendix B for discussion of alternative analyses of spinner drag. For this report, “spinner” refers to the entire fairing around the hub, including an ogival cone upstream of the hub and a skirt fairing immediately behind the cone (Fig. 30). The seam between the cone and skirt is barely visible in the photo. The cone and skirt rotated with the hub but did not gimbal. The skirt had oblong holes to accommodate the pitch and flap motions of the blade shanks and spindles.

Figure 30. Close-up of the JVX rotor on the PTR in the OARF test configuration.

Figure 31. The JVX rotor on the PTR with the wing in airplane mode.

A limited amount of spinner tare data were taken during the Phase I wind tunnel test. Data were taken with the rotor blades removed over a range of airspeeds from 131 to 238 knots. With one exception, the spinner was always rotating at 495 rpm. Data were taken at three different yaw (ψ_s) angles: 0, −3, and −6 deg (rotor shaft yaw, set by the tunnel turntable). No equivalent tare data were taken during the Phase II test database. All spinner tare data were taken with a wing installed in airplane mode (Fig. 31), but the wing was sufficiently far behind the spinner that interference effects can be assumed to be negligible.

The Phase I spinner tare data are plotted in Figure 32, in units of drag versus tunnel dynamic pressure q_0. The data fall into three distinct, narrow bands, one for each yaw angle. The data point at 52 rpm, $\psi_s = -6$ (marked with a solid symbol in the plot), is slightly off the trend for the 495-rpm data, but a solo data point is insufficient for judging sensitivity to rpm.

The trends are highly linear and apparently closely similar. Linear curve fits to the 495-rpm data yield the following equations:

$$\psi_s = 0 \text{ deg:} \qquad \text{Drag} = 0.901 \text{ ft}^2 q_0 + 6.25 \text{ lb} \qquad r^2 = 0.99222$$

$$\psi_s = -3 \text{ deg:} \qquad \text{Drag} = 0.876 \text{ ft}^2 q_0 + 14.83 \text{ lb} \qquad r^2 = 0.99734$$

$$\psi_s = -6 \text{ deg:} \qquad \text{Drag} = 0.912 \text{ ft}^2 q_0 + 16.77 \text{ lb} \qquad r^2 = 0.99836$$

where r^2 is the correlation coefficient. For clarity, only the fit to $\psi_s = 0$ deg is shown in Figure 32. The intercepts differ from zero by less than the claimed accuracy of the balance (refs. 1 and 11).

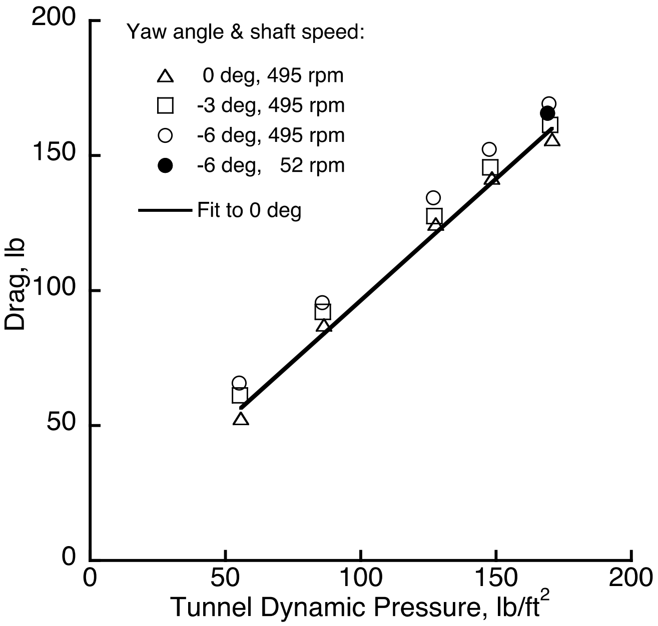

Figure 32. Phase I spinner tare data, plotted as raw drag versus q_0.

The drag values are lower than those of references 4, 5, and 15. For the data presented in this report, the spinner drag tare is taken from the curve fit to the data at zero yaw angle, but without any zero offset. Hence the equivalent flat-plate drag tare A_{SP} = 0.901 ft^2, which is less than the plotted values in reference 15. That report is for a full-scale test of the XV-15 rotor, which used a hub and spinner identical to those used for the JVX test. For the data presented in this report, A_{SP} = 0.901 ft^2 resulted in calculated spinner drag as high as 23 percent of the measured axial load.

The spinner was instrumented with internal pressure transducers, but the pressure data were questionable and were not used here. The spinner tares used here are accordingly different from those of reference 2. See Appendix B for further discussion of spinner pressures.

A complication is the somewhat imprecise definition of "spinner drag." Reference 15 (Fig. IV-6) gives limited data for three different XV-15 blades-off configurations: with spindles; without spindles, spinner openings covered; and without spindles, openings uncovered. The spinner radius is 13.63 in. at the base, and slightly less at the spindle holes. The spindles project about 5 in. beyond the spinner surface; each spindle diameter is about 4 in. at the outboard end. Dimensions are approximate because of the compound curve of the spinner and the nonuniform taper of the spindles. The spindles add about 0.3 ft^2 to the spinner drag area, relative to the drag with spindle holes closed (ref. 15).

The data presented in Figure 32 with spindles exposed roughly match the data in reference 15 with the spindles removed. The reason for the discrepancy is unknown. However, the data in Figure 32 were taken from the onboard rotor balance, whereas the data in reference 15 were taken from the tunnel scales. Reference 15 does not describe how XV-15 spinner tares were distinguished from total installation tares. The rotor balance used for the JVX tests directly measured the spinner loads transferred to the rotor shaft, so its data should be more reliable at the low drag levels characteristic of spinner tares.

When the blades are installed, the spindles are almost entirely enclosed within the blade shanks. A spindle is just barely visible for the lower JVX blade in Figure 30. The effect on spinner tares of the different root shapes for the JVX and XV-15 blades is unknown.

The assumptions underlying the use of spinner drag A_{SP} = 0.901 ft^2 can be summarized as follows: (1) the data from the JVX Phase I test are more accurate than the XV-15 data at the measured levels of spinner drag; (2) the wing had a negligible effect on spinner drag; and (3) installation of the rotor blades had negligible effect on spinner drag. The last statement has three supporting assumptions: the shorter but thicker blade shanks contributed the same net drag as the spindles, aerodynamic interference from the blade root section was small, and the blades did not change the internal spinner pressures.

Torque/Thrust Interactions

In the original JVX database, the rotor balance data were corrected for residual rotor shaft axial thrust with an equation of the following form:

$$X_c = X_b + X_s - K_{TQ} Q_s \qquad [11]$$

where X_c is the corrected X-force (thrust), X_b is the X-force measured at the balance, X_s is the residual shaft thrust, K_{TQ} is the thrust/torque correction coefficient, and Q_s is the raw shaft torque. Spinner drag corrections are accounted for separately. The accuracy of the X-force corrections, as applied to the Phase II database, is thrown into question by the following analysis.

In order to check for the possibility of incorrect values of thrust, CAMRAD II predictions of JVX performance were trimmed to the values of torque measured at each wind tunnel data point, with airfoil section drag c_d adjusted by −0.002. The difference between measured and predicted thrust is plotted at each data point in Figure 33. The CAMRAD free-wake model was used here, but the results are barely distinguishable from those obtained with a BEMT analysis. BEMT is too well-proven for those predictions to be easily discarded as erroneous. The good consistency between aerodynamic models is an important justification for the assumptions made here. See also the discussion of U^{2}NCLE predictions in the section “Additional CAMRAD II Predictions.”

Figure 33 shows a clear trend of thrust difference versus torque. Without the c_d adjustment, the data are shifted downwards but with little change in slope. A linear curve fit yields a slope of −0.0080 lb/ft-lb. The value of K_{TQ} used to generate the database was −0.0086 lb/ft-lb; the slope of the plotted data is not significantly different from K_{TQ} (per a *t*-test at the 5-percent level).

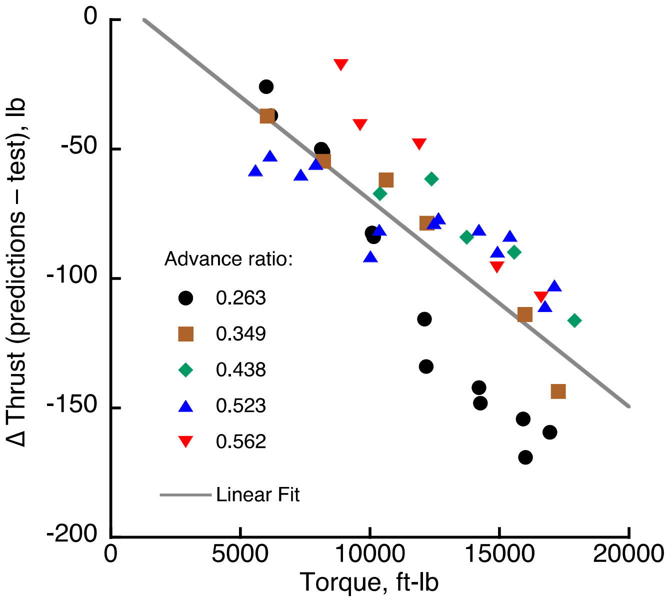

Figure 33. Difference between predicted and measured thrust versus torque.

There is a discernible variation in slope with advance ratio, but the variation is consistent only for the data taken at 489 rpm ($\mu < 0.562$). The slope at the highest μ is similar to that at the lowest μ. For all but the $\mu = 0.532$ data, the slopes vary linearly with both tunnel velocity and air temperature (not shown here). Unfortunately, there are no data for balance or rotor shaft temperature, so it is not possible to separate residual aerodynamic effects from thermal effects on instrumentation.

The data at different advance ratios were not all taken during the same test run. Table 6 lists the data runs for each advance ratio. The only subset that includes data from Run 8 is $\mu = 0.263$, and $\mu = 0.523$ is the only subset with data from Run 9. Figure 33 shows that these are the two advance ratios with the largest difference in slope. This raises further suspicion of an instrumentation problem or thermal effect, but it falls far short of proof.

There is no evident aerodynamic mechanism that can explain these results. An error in computation of induced power could result in an error that varies linearly with torque, but such a close match to K_{TQ} would be a remarkable coincidence. An error in predicted rotor drag, hence profile power, such as might be caused by an error in the airfoil tables, would vary with both airspeed and tip speed. An error in spinner drag would vary strongly with airspeed.

Table 6. Data runs for each value of advance ratio.

μ	Data Run
0.263	4, 8
0.349	4
0.438	4
0.523	5, 9
0.562	5

A more likely explanation is that the thrust/torque correction was improperly applied to the data, or possibly that the measurements of residual shaft thrust were inaccurate. The numerical equivalence of the slope in Figure 33 and the database value of K_{TQ} is telling.

Not all intermediate values of balance data and corrections were recorded in the OARF hover database, so the thrust for the OARF tests cannot be corrected in exactly the same manner. The shaft torque Q_s is itself subject to corrections for thrust/torque interaction and bearing friction, which should not be applied to K_{TQ}. The torque data have these corrections. An approximate correction would simply add K_{TQ} times torque (as corrected) to thrust, which for a negative value of K_{TQ} will reduce figure of merit. The result would be a worse match to the CAMRAD II predictions for high-speed data, but a better match to the wind tunnel hover data (see Fig. A-1). The wind tunnel hover data should be less accurate than the OARF data, so a better match would not necessarily be an improvement. Accordingly, all OARF data presented here use rotor thrust exactly as in the database. The possibility remains that the OARF data are less accurate than thought, and the wind tunnel hover data more accurate, but this is highly unlikely.

The flex coupling had multiple strain gages. A different set was used for Phase II, compared to the Phase I wind tunnel test and the OARF hover test. This could explain why the problem—assuming it is real—was seen only in the Phase II data. The counterpart to K_{TQ}, the thrust/torque interaction K_{QT}, was nearly the same for Phase I and Phase II: 0.2089 versus 0.2143 ft-lb/lb, respectively, a difference of less than 3 percent. In contrast, the Phase I and Phase II values of K_{TQ} differed by nearly a factor of 4: −0.0023 versus −0.0086 lb/ft-lb, respectively.

There are too little data in the Phase I wind tunnel test to check the K_{TQ} adjustment in the manner of Figure 33. No correction to K_{TQ} was applied to the spinner tare data. However, the spinner drag data were taken at extremely low torque, therefore terms in K_{TQ} should have negligible effect on spinner tares.

Further justification for doubting the database value of K_{TQ} is given by Figures 34 and 35, which compare the Phase I results *with* K_{TQ} with those of Phase II *without* K_{TQ}. During Phase I, few data points were taken at the same values of tip speed as during Phase II, and fewer still where thrust was varied systematically at constant values of tip speed and tunnel speed. There were only two advance ratios at which the Phase I and Phase II data had the same tip speed, and even here, neither μ nor M_{tip} quite match for the two data sets. Table 5 gives the values for the Phase II data, and Table 7 gives the equivalent data for the Phase I data plotted in Figures 34 and 35. For ease of comparison, the figures show only the data at $M_{tip} = 0.58$.

Table 7. Mean test conditions for JVX Phase I wind tunnel data, with standard deviations. V_{tip} and M_{tip} are nominal hover values.

μ	Ω (rpm)	V_{tip} (ft/sec)	M_{tip}	V (knots)	$s_d(\mu)$	$s_d(V_{tip})$ (ft/sec)	$s_d(V)$ (knots)
0.210	494	646	0.57	80	0.0005	2.7	0.2
0.259	497	650	0.57	100	0.0011	0.7	0.3
0.344	497	650	0.57	132	0.0002	1.4	0.3

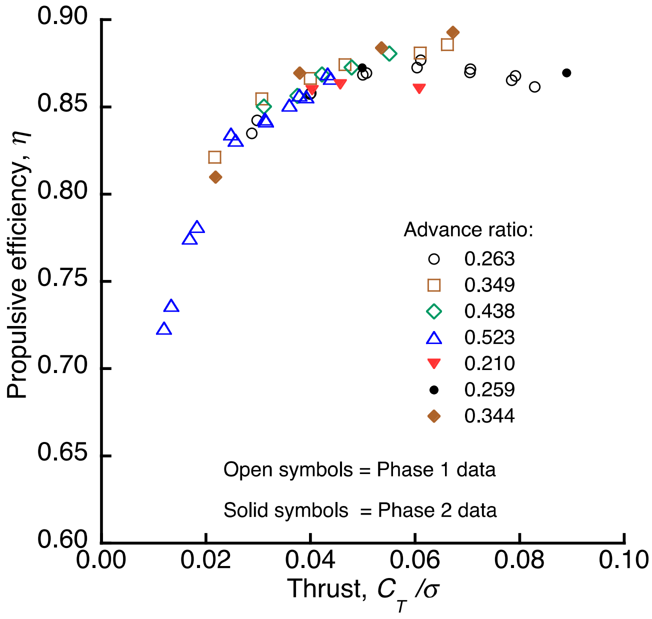

Figure 34. Rotor propulsive efficiency from the Phase I and Phase II tests at M_{tip} = 0.58.

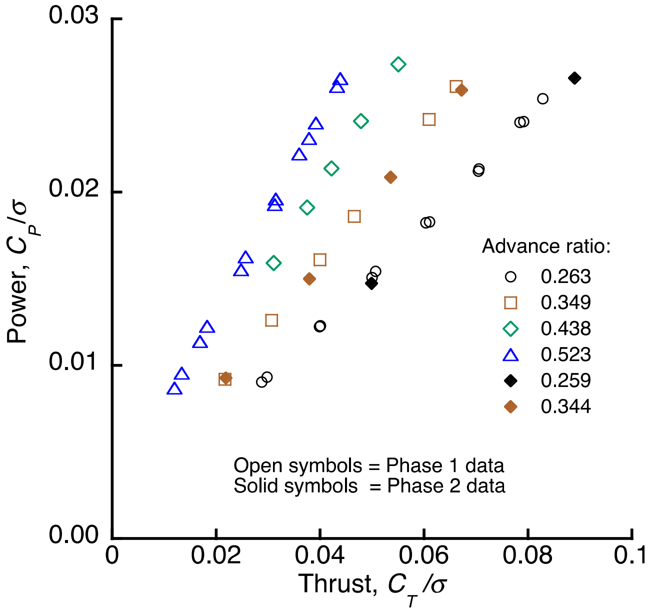

Figure 35. Rotor power from the Phase I and Phase II tests at M_{tip} = 0.58.

Figure 34 plots propulsive efficiency versus thrust, here without any plotting offsets (compare Figure 28). Collapsing the data emphasizes that the Phase II trends of μ versus thrust are similar for all advance ratios at the given tip speed (M_{tip} = 0.58). The trends for the Phase I data are not as consistent, but at least some of the variation may be caused by disparities in operating condition. The Phase II data lie roughly within the bounds of the Phase I data, but this is hardly a rigorous comparison, again considering the imperfectly matched operating conditions. Nevertheless, the two data sets, generated with the same assumptions of spinner drag but different assumptions of torque/thrust interaction, give very similar results.

Figure 35 plots power versus thrust, including the two advance ratios from Phase I that match test conditions in Phase II. A difference in slope is discernible at both advance ratios where the data overlap. The data at $\mu = 0.349$ were analyzed in more detail by curve fits to ideal power. The analysis was limited to $\mu = 0.349$ because that is the only advance ratio at which both tests had more than two data points. Given fixed M_{tip} and μ, power should vary as $P = T(V+v)$, which at the low levels of thrust seen here is close to $C_P = \mu C_T$, plus a constant term for profile power. (This analysis is developed more fully in the section "Regression Analysis," later in this report.) Comparing the Phase I and Phase II curve fits, the ratio of the slopes was less than the ratio of μ, and both ratios were less than the standard error of the slopes. Therefore, the difference in slope can be fully explained by the difference in μ.

Furthermore, there is one data point, at $\mu = 0.349$ and $C_T/\sigma = 0.022$, at which tunnel velocity matches within 0.02 percent, and Phase II thrust and torque are both less than 1 percent lower than the Phase I data. At that operating condition, Phase II tip speed is lower than Phase I by 1.4 percent, hence μ and η are slightly higher, as shown in Figure 34. Even though the match is imperfect, the variations are all small and consistent, so there is no evident bias in either thrust or power.

The preceding argument rests on a handful of data points at a single combination of M_{tip} and μ, and at the extreme compares one data point from each of the two tests. This is hardly a rigorous analysis, but unfortunately the two data sets are not sufficiently well-matched to allow much improvement. Nevertheless, inspection of Figures 34 and 35 shows that the data are closely similar if the Phase I data use the nominal value of K_{TQ} and the Phase II data use $K_{TQ} = 0$.

There are physical reasons to expect that the flex coupling will exhibit torque/thrust interactions under high strain. If the strain gages were perfect, then K_{TQ} would be an exact measure of material strain effects, and the same coefficient could be used for both Phase I and Phase II data. However, K_{TQ} necessarily includes the imperfections of the strain gages, and the same coefficient should not be applied to data from different strain gages.

If the nominal value of $K_{TQ} = -0.0086$ is applied to the Phase II data, the result is much higher propulsive efficiency, as high as $\eta = 0.93$. This value is almost as high as the maximum value for the XV-15 data (ref. 15), but taken at a higher tip speed and with a higher solidity rotor. Such an improvement strains credibility, and the Phase I and Phase II data cannot possibly match if the nominal values of K_{TQ} are applied to both data sets. Accordingly, the torque/thrust interaction term was not applied to the Phase II data reported here. Enough data are given in Appendix D to recompute thrust with the nominal interaction, or any other value of K_{TQ}, should the reader so choose.

While these results do not prove the existence of a misapplied thrust/torque interaction for Phase II, the excellent match between predictions and wind tunnel data (as corrected), and between the two different tests, cannot be lightly dismissed. It would be of questionable legitimacy to derive a new value of K_{TQ} using CAMRAD II predictions. Nevertheless, CAMRAD proved useful for revealing the torque/thrust correction as the likely source of the discrepancy between Phase I and Phase II. The results shown here may point the way towards more extensive data-consistency checks that could be applied during future rotor tests, in hopes of early detection and correction of errors in data acquisition and processing.

Data Consistency

Data consistency was examined for the two advance ratios with the most data points. For μ = 0.263 and μ = 0.523, there were two separate runs with repeated data at most thrust conditions, as shown in Figure 36. Shaft torque and measured drag are plotted without any adjustments for spinner tares: the data include only balance and torque calibration corrections, without the torque/thrust interaction term. Nor were the data converted to rotor coefficients, so the plotted points are as close as practical to raw balance data. Total drag, as measured by the balance, includes spinner drag, so measured drag is zero when rotor thrust equals spinner drag. At a given tunnel speed, spinner drag is constant and does not affect the run-to-run comparisons discussed next.

The data in Figure 36 match closely at each advance ratio and are highly linear. At a fixed tunnel speed and rotor tip speed, power, hence shaft torque, should include a constant contribution of profile power and a linearly varying contribution of induced power. Linear curve fits determined the slopes and intercepts separately for the two runs at each advance ratio. None of the differences between runs at a given advance ratio were statistically significant. For all four curve fits, the worst-case correlation coefficient was 0.9995.

Strictly speaking, neither shaft torque nor rotor drag is an independent variable: both are functions of collective. Hence the simple regression analysis summarized here is not as rigorous as might be desired. Nevertheless, the measurements showed excellent linearity and consistency. The intercepts, in terms of thrust, varied less than the claimed accuracy in thrust measurement (refs. 1 and 11). Similar results were obtained if the torque/thrust interaction was included.

Summarizing, the measurements were acceptably repeatable from run to run and from point to point.

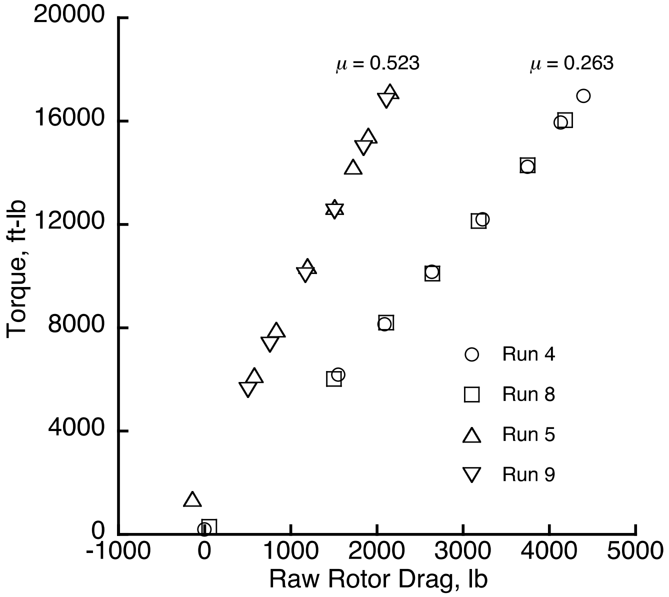

Figure 36. Measured JVX shaft torque versus rotor drag sorted by run.

Regression Analysis

Following the same general procedure as applied to the hover data, a regression analysis was used to estimate the uncertainty in the wind tunnel data. Measured JVX rotor power is plotted against thrust in Figure 37. A linear curve fit to ideal power and profile power factor is also shown (equations are given later in this section). Figures 38 and 39 show the curve fit converted to propulsive efficiency and non-propulsive power, respectively (conversions provided later). The scales are expanded to more clearly show the data points. For Figure 38, the data points are offset in C_T/σ by multiples of 0.01 to make the trends easier to see. The plot of non-propulsive power (Fig. 39) better reveals the nonlinear trends in the data.

In high-speed axial flight, the induced power is low but not zero. The total rotor power comprises the propulsive power TV, induced power Tv, profile power P_0, and possibly parasite power from hub drag, depending on how drag tares are accounted for in the data processing. Following reference 19, the ideal or minimum possible power P_m can be defined as

$$P_m = T(V+v) = T\left[\frac{V}{2} + \sqrt{\left(\frac{V}{2}\right)^2 + \frac{T}{2\rho A}}\right] \qquad [12a]$$

or

$$C_{Pm} = \frac{C_T}{2}\left[\mu + \sqrt{\mu^2 + 2C_T}\right] \qquad [12b]$$

Equation 12 is based on the same physical considerations as those of Eq. 1, but adds the effects of axial flow.

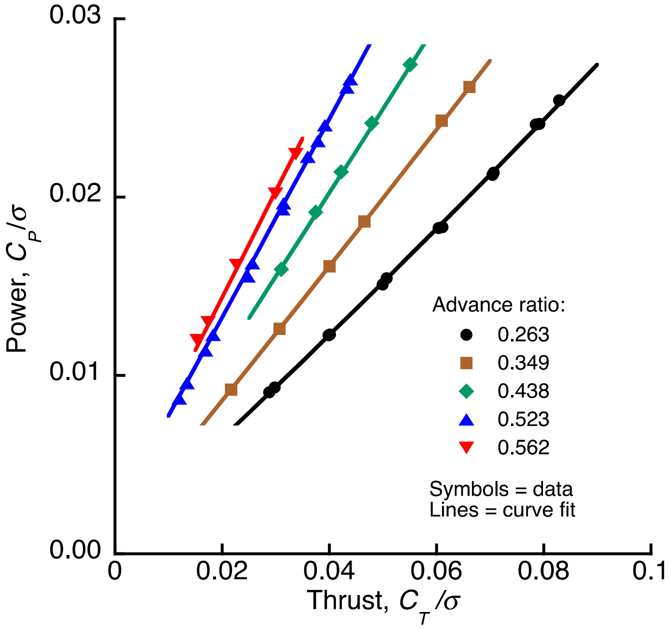

Figure 37. Curve fit to measured rotor power from the NFAC Phase II test.

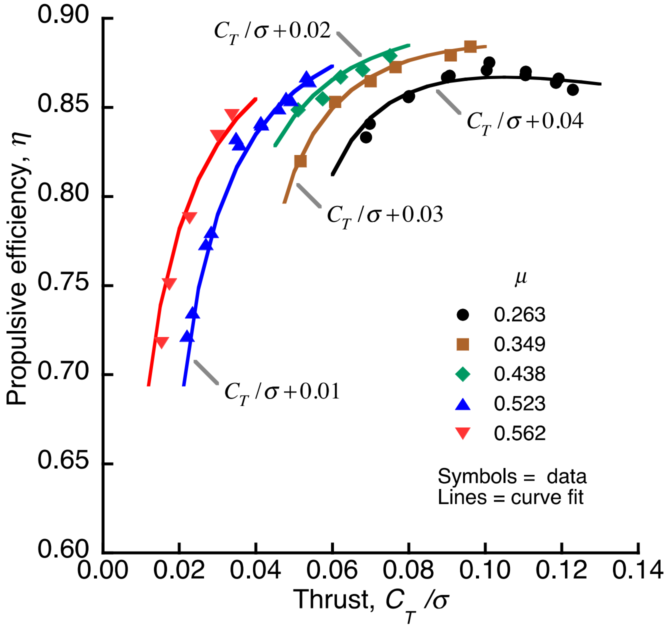

Figure 38. Curve fit to measured rotor power, converted to propulsive efficiency.

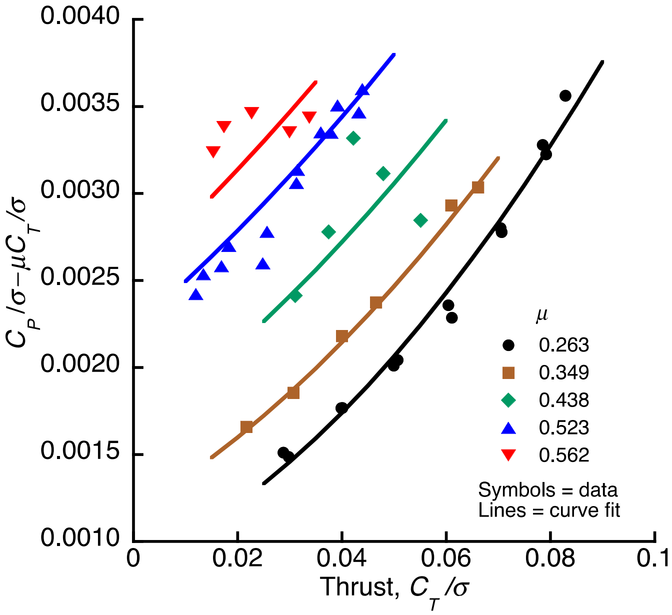

Figure 39. Curve fits to measured rotor power, with propulsive power subtracted.

If $v<<V$, P_m is nearly linear in T. However, the induced power term is physically important and statistically significant. A linear fit to C_T at one airspeed can give good results only for that airspeed. The curve fit shown here includes all terms in Eq. 12. Non-ideal power (Fig. 40) is simply measured $C_P/\sigma - C_{Pm}/\sigma$; note that propulsive power $\mu C_T/\sigma$ has also been subtracted (compare with Figure 39).

To account for the effects of airspeed, a profile power term must be added. Using the notation of reference 19, the equation can be written as

$$C_{Po} = (\sigma/8)c_{d\,\mathrm{mean}}F_P, \qquad [13]$$

where $c_{d\mathrm{mean}}$ is the mean blade section drag coefficient and the function F_P accounts for the increase in blade section velocity as V increases:

$$F_P = \sqrt{1+\mu^2}\left(1+\tfrac{5}{2}\mu^2\right)+\tfrac{3}{2}\mu^4\ln\left(\frac{\sqrt{1+\mu^2}+1}{\mu}\right) \qquad [14]$$

(compare Eq. 6; see also reference 2). For the data plotted here, F_P ranges from 1.225 to 2.259.

Equation 14 is physically exact for a constant $c_{d\mathrm{mean}}$. The twist distribution of the JVX rotor is a compromise between hover and airplane-mode performance. There is no guarantee that all blade sections will always operate near c_{d0}, hence $c_{d\mathrm{mean}}$ is not necessarily constant with airspeed. Nevertheless, Eq. 14 gives good results, as shown in Figures 37–40, with the exception of the highest advance ratio.

Figure 37 shows a multiple-linear curve fit to measured C_P/σ with C_{Pm}/σ and F_P as the independent variables; Figure 38 shows the same fit, converted to propulsive efficiency $\eta = TV/P = \mu C_T/C_P$. Figures 39 and 40 respectively plot the fit as non-propulsive power $C_P/\sigma - \mu C_T/\sigma$ and non-ideal power $C_P/\sigma - C_{Pm}/\sigma$. The latter figure shows the effects of profile power plus non-ideal induced power.

The regression analysis used exact values of μ and F_p, but the plotted curve used averaged values of μ and F_p for smoothing. Except where noted, there is only one curve fit, derived from the entire data set. It plots as multiple lines because it includes terms in μ (Eq. 14).

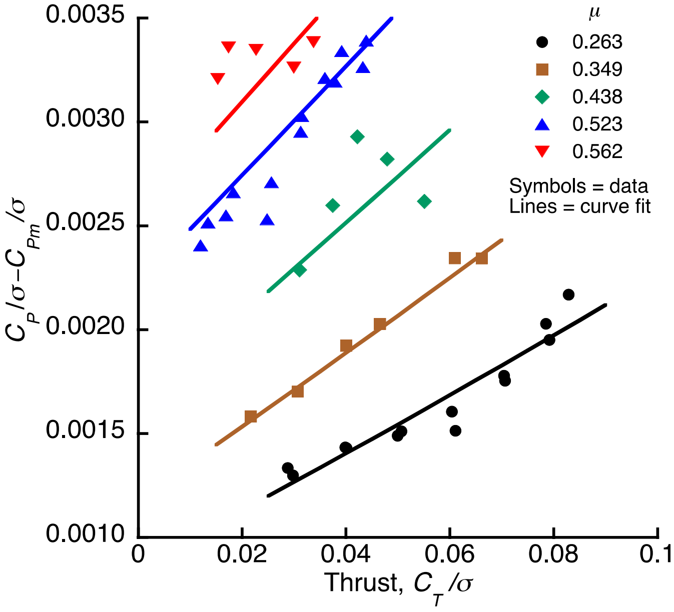

Figure 40. Curve fits to measured rotor power, with ideal power subtracted.

The curve fit plotted in Figures 37–40 is

$$C_P / \sigma = 1.049 C_{Pm} / \sigma + 0.001632 F_P - 0.001136 \qquad [15]$$

with a standard error $s_e(C_P/\sigma) = 0.000125$. This is 0.46 percent of the maximum measured value of C_P/σ. The intercept is not significantly different from zero. For comparison to hover, the uncertainty can be expressed in terms of C_P: $s_e(C_P) = 0.0000143$. The standard error is slightly greater than that for the quadratic fit to hover data (Eq. 5). The coefficient of F_P is equivalent to $c_{d\mathrm{mean}} = 0.01306$.

Figure 40 reveals the non-ideal power trends versus thrust; that is, the power not explainable by momentum theory. Comparing Figure 37 with Figure 40, non-ideal power is an order of magnitude less than measured power. Subtracting both propulsive power and ideal induced power results in a series of linear trends with airspeed (compare with the nonlinear trends in Figure 39). The vertical offsets of the trend lines represent profile power that is essentially constant at any given airspeed, and the linear trends represent non-ideal induced power, or thrust multiplied by non-ideal induced velocity.

A slightly nonlinear trend can be seen in the data at $\mu = 0.263$, notably above $C_T/\sigma = 0.06$. There is no physical requirement for the losses to be perfectly linear with thrust (a linear variation would imply constant induced velocity). Only one other advance ratio, $\mu = 0.349$, has any data at $C_T/\sigma > 0.06$, and only two data points at that. Unfortunately, the limitations of the data do not encourage further refinement of the analysis in the manner done for hover data.

Figure 40 also reveals that the data at $\mu = 0.438$ have high scatter, and the data at $\mu = 0.562$ appear to follow a different trend than predicted by Eq. 15. The JVX data at $\mu = 0.562$ are problematic, simply because the average tip speed is different from that at all other data points (695 ft/sec versus 641 ft/sec), and because there are so few data points at that speed. Any curve fit will best fit the test conditions with the most data points, so the regression lines should not be expected to closely follow the data at $\mu = 0.562$.

Re-running the regression analysis of Eq. 15, but without the data at $\mu = 0.562$, resulted in a standard error $s_e(C_P/\sigma) = 0.0000920$. The difference with respect to the fit with the high-speed data is statistically significant, despite the reduced degrees of freedom. This result implies that the data at maximum speed contribute a disproportionate amount of uncertainty.

Two advance ratios, $\mu = 0.263$ and $\mu = 0.523$, each contain considerably more data points than the others, making these data subsets useful for more detailed comparisons. Curve fits to these data subsets were performed separately at each advance ratio, using only C_{Pm}/σ as the independent variable. There was a slight improvement in standard error for each fit, compared to the fits shown in Figures 37–40 and Eq. 12, but the differences were not statistically significant. While the scatter in the data at each advance ratio may possibly be less than the aggregate for all data points, the reduction in degrees of freedom for separate fits will adversely affect the uncertainty. For this reason, all following comparisons are based on the global curve fit to the entire data set, as given in Eq. 12, unless otherwise noted.

In order to better reveal the data, Figures 41 and 42 re-plot the curve fit of Figure 37 for the two values of μ with the greatest number of points. Also plotted are $\pm 2s_e$ uncertainty bands. Uncertainty bands are potentially misleading for values of thrust outside the range of the data, and are therefore extended only slightly beyond the data in the figures. The thrust scale of Figure 41 is twice that of Figure 42. All but one data point fall within $\pm 2s_e$ of the global fit.

For these two figures, the uncertainty bands are the standard errors of C_P/σ converted to $\eta = \mu C_T / C_P$. The advance ratio in Figure 42 is almost exactly twice that of Figure 41, but the efficiency is similar. At the same value of C_T/σ, the μ = 0.523 data has about twice the value of C_P/σ. Therefore, a constant value of s_e plots as uncertainty bands with about half the vertical spread as those for μ = 0.263.

Figures 43 and 44 show the prediction interval (P.I.) and the confidence interval (C.I.) for the same curve fit as in Figures 41 and 42, converted to η. The thrust scale of Figure 43 is twice that of Figure 44. The prediction interval is the uncertainty in the prediction of a given data point, whereas the confidence interval is a measure of uncertainty in the regression line. The prediction interval is similar to the standard error, but takes into account the increase in uncertainty with distance from the mean value of the independent variable. For the data in Figures 43 and 44, the prediction interval is comparable to the standard error.

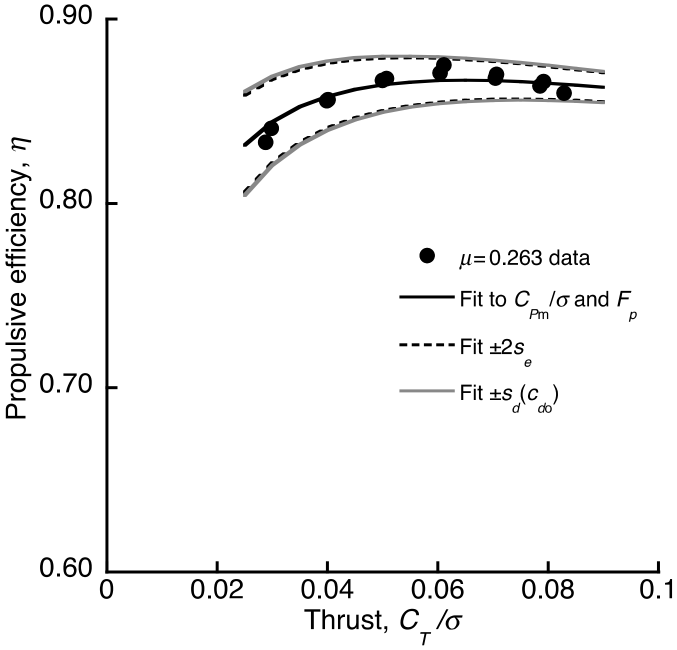

Figure 41. Uncertainty bands ($\pm 2s_e$) for propulsive efficiency at μ = 0.263 with $\pm 2s_d(c_{d0})$ bands.

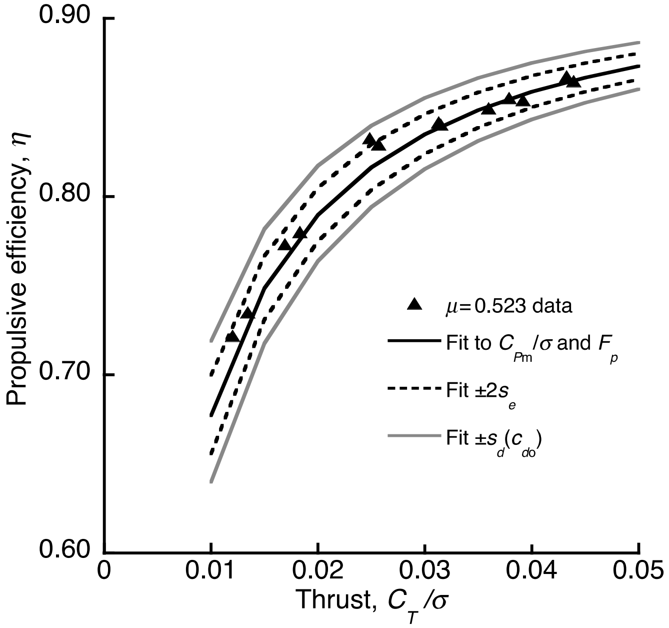

Figure 42. Uncertainty bands ($\pm 2s_e$) for propulsive efficiency at μ = 0.523 with $\pm 2s_d(c_{d0})$ bands.

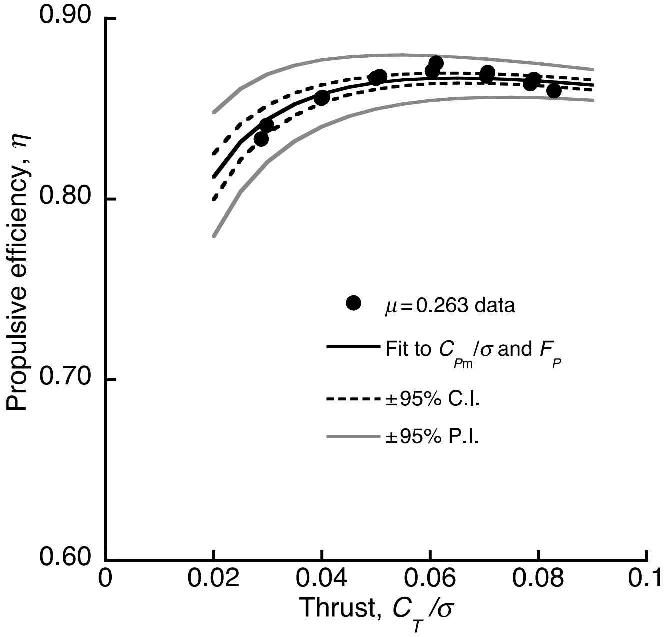

Figure 43. Curve fit of power at μ = 0.263, converted to propulsive efficiency, with confidence and prediction intervals.

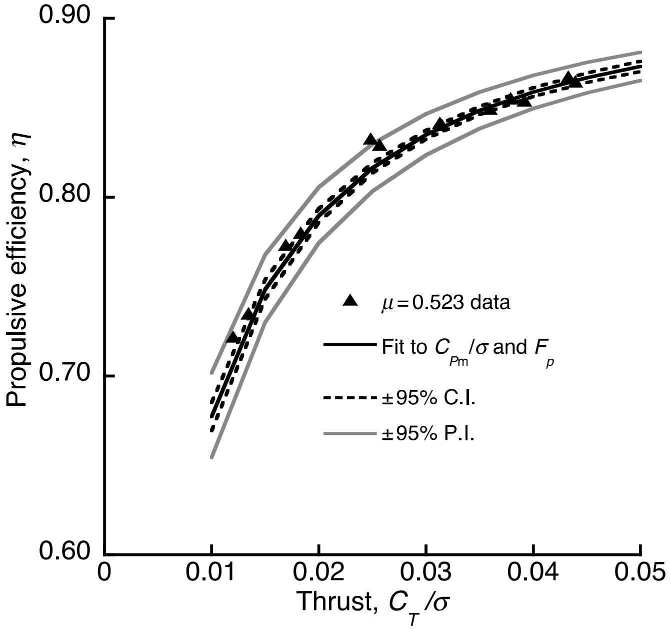

Figure 44. Curve fit of power at μ = 0.523, converted to propulsive efficiency, with confidence and prediction intervals.

The relative importance of uncertainty in the airfoil performance may be evaluated by following the same procedure used for hover. Substituting s_d (c_{d0}) into Eq. 13 gives an estimated ΔC_{Po}, which can be readily converted to an equivalent $\Delta\eta$. In Figures 41 and 42, the estimated uncertainty in η due to airfoil properties, $\pm 2s_d$ (c_{d0}), is plotted with the $\pm 2s_e$ bands due to uncertainty in measured power (from Eq. 15).

Any uncertainty in drag will have a larger effect on power at high speed than at lower speed. At μ = 0.263 (Fig. 41), the uncertainty in airfoil drag $s_d(c_{d0})$ is nearly the same magnitude as the uncertainty of the curve fit $s_e(C_P)$. This result is similar to that for hover (Fig. 18). At twice the airspeed, μ = 0.523 (Fig. 42), the uncertainty in drag is about twice the uncertainty of the curve fit.

For the JVX Phase II data, the maximum helical Mach number at 0.75 *R* was 0.59, which is comfortably below drag divergence for the XN-12 airfoil at that radial station (ref. 27). Had the maximum airspeed been higher, drag-divergence effects might have become important, at least at high rotor tip speeds. Reference 21 presents statistics for drag divergence, which could usefully be compared to future high-speed test data.

Additional CAMRAD II Predictions

CAMRAD II predictions of rotor performance are plotted in Figures 28–29, all made with the rolled-up free-wake model and c_d adjusted by −0.002. Figures 45 and 46 expand the scale and add the uncertainty bands of the curve fits to the wind tunnel data (Eq. 15). These plots include the advance ratios with the most data points (μ = 0.263 and μ = 0.523). The uncertainty is expressed as ±95 percent prediction intervals.

The uncertainty bands shown in Figures 45 and 46 are those for the multiple-linear curve fit to the entire data set (Eq. 15) and do not perfectly capture the trend for any given advance ratio. The discrepancy is most obvious at high C_T/σ and low μ (Fig. 45).

Also shown are CAMRAD predictions with a uniform-inflow model. Predictions were made with a blade element/momentum theory (BEMT); they are not shown because they vary from the free-wake predictions by barely more than one line width at most. At μ = 0.523, the CAMRAD predictions closely follow the data and always fall within the uncertainty bands. At μ = 0.263, the CAMRAD predictions exceed the uncertainty bands at high thrust, although CAMRAD follows the nonlinear trend in the data.

The uniform-inflow and BEMT models require empirical adjustments to the inflow velocity, expressed as the induced power ratio κ. To match the free-wake predictions, BEMT required κ = 1.25 at μ = 0.263 and κ = 1.60 at μ = 0.263. In contrast, the free-wake model requires no empiricism in the calculation of induced velocity and was therefore used for all airplane-mode predictions in this report, except as noted in Figures 45 and 46. The free-wake model does allow for empirical adjustments to the tip vortex model, particularly the core size and radial location. The analyses done for this report used the CAMRAD II default values of core size (20 percent mean chord) and recommended values of radial location (98 percent radius), although the predictions showed little sensitivity to these two parameters. The low sensitivity to the wake model is expected at high axial velocity. See references 20 and 28 for details of the CAMRAD II wake model.

The uniform-inflow model appears to follow the data better than the free-wake model, but that was achieved only by adjusting κ. In Figures 45 and 46, the uniform-inflow model required κ = 1.7 at μ = 0.263 and κ = 5.5 at μ = 0.263. The very large value of κ required at low μ suggests that the uniform-inflow model has reached the limits of its validity. Further optimization of κ should yield a better match of BEMT to the data, or uniform inflow to the free wake, but no further effort was made here to improve what are, after all, purely empirical adjustments.

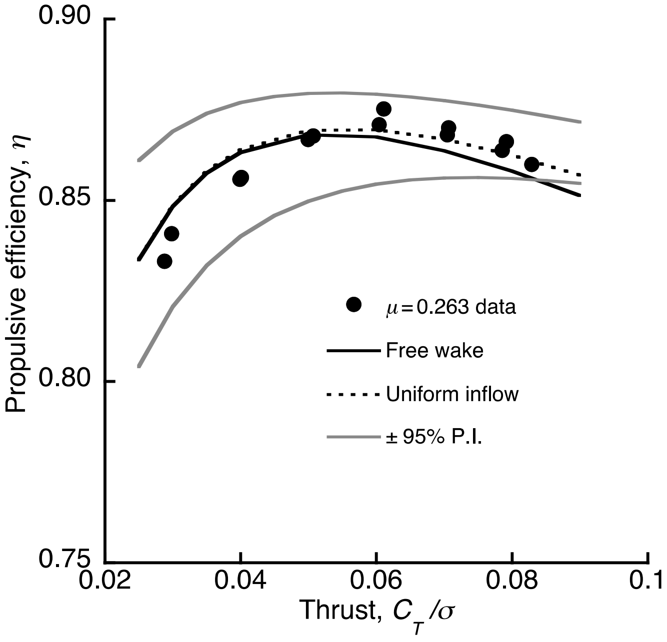

Figure 45. CAMRAD II predictions of JVX propulsive efficiency at μ = 0.263 with data uncertainty bands.

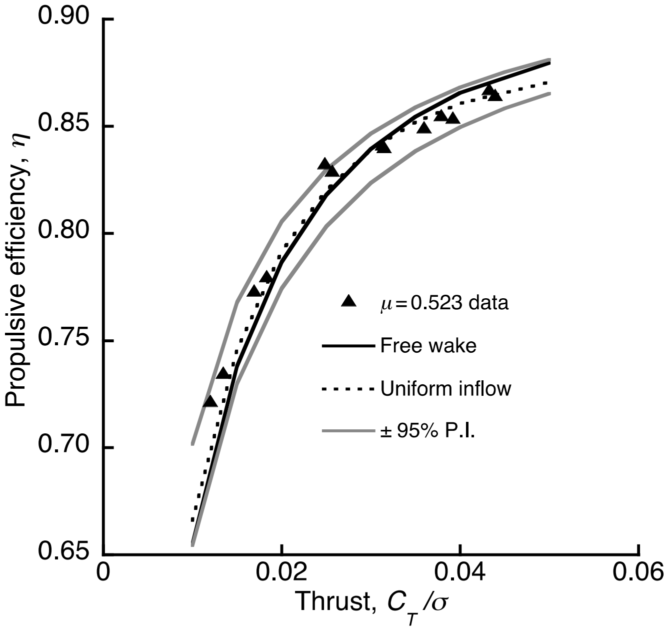

Figure 46. CAMRAD II predictions of JVX propulsive efficiency at μ = 0.523 with data uncertainty bands.

With the data and uncertainty bands plotted on the expanded scales of Figures 45 and 46, it is evident that the curve fit of Eq. 15 does not fully capture the trends in the data, particularly at low μ and high C_T/σ. While extending the regression analysis to higher orders of the independent variables is possible, it is not recommended here because of the limited data set. Figure 40 shows that the scatter at μ = 0.438 is large, and the range of thrust at μ = 0.438 and μ = 0.562 is small. Furthermore, there are very few data points at M_{tip} = 0.63 (μ = 0.562). For these reasons, it is highly unlikely that a more elaborate regression model could better capture the trends with thrust or tip speed.

CAMRAD allows for different Reynolds number corrections to be applied to the input airfoil coefficients; details of the correction method are given at the end of the discussions of hover data. Unless otherwise noted, the turbulent correction (Eq. 10, $n = 0.2$) was used for all CAMRAD predictions. Figure 47 shows predictions made with the same three models as were applied for hover, but here applied at $\mu = 0.263$ and $\mu = 0.523$. No adjustments were made to section c_d, in contrast to all previous plots of CAMRAD predictions for axial-flow conditions. Data and predictions at $\mu = 0.523$ are offset vertically by –0.01. It is clear that the predictions fall short of measured rotor performance, and that Reynolds number corrections can only partially account for the shortfall.

CAMRAD and U^{2}NCLE predictions for axial flow are compared in Figure 48. No adjustments were made to section c_d for either code. As in Figure 47, the CAMRAD predictions in Figure 48 used a free-wake model with a turbulent Reynolds number correction. The U^{2}NCLE predictions used the Steady DES turbulence model (ref. 6).

The CAMRAD and U^{2}NCLE predictions match each other very well, especially at high speed. However, neither code predicts performance as well as the CAMRAD predictions with $\Delta c_d = -0.002$; this holds true for free-wake, BEMT, and uniform-inflow models. The two codes, CAMRAD and U^{2}NCLE, were independently developed and their rotor models independently constructed. Furthermore, CAMRAD relies on external airfoil tables for blade section aerodynamics, here based on 2D wind tunnel test data, in contrast to U^{2}NCLE, which is a CFD code. The likelihood of both sets of predictions having identical errors is small.

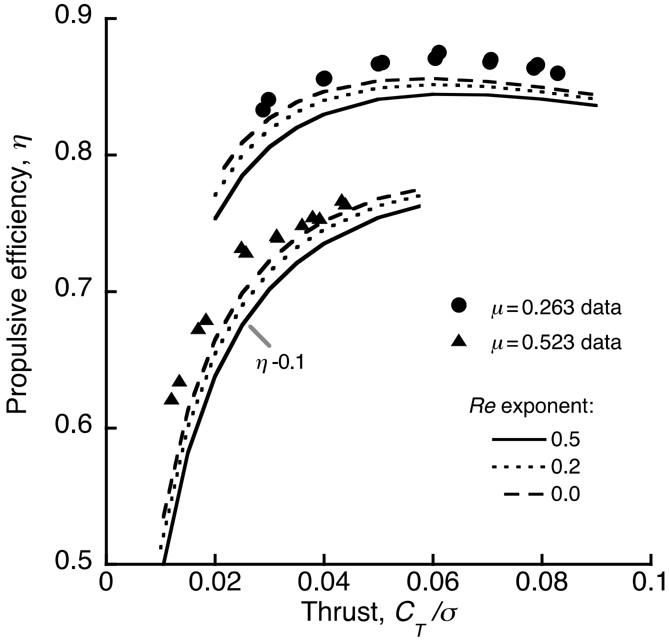

Figure 47. CAMRAD II predictions of JVX propulsive efficiency with three Reynolds number correction models.

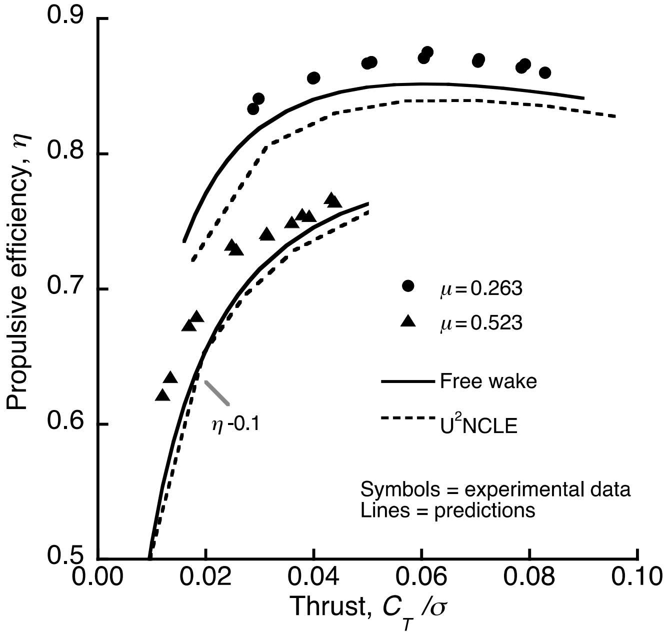

Figure 48. CAMRAD and U^2NCLE predictions of JVX propulsive efficiency in axial flow.

There remains the possibility that the rotor experienced some degree of laminar flow during the test that would explain the mismatch for both codes. The rotor blades were cleaned every day, and were operated inside a closed-circuit wind tunnel and thereby protected from the elements. Laminar flow over some portion of the rotor is entirely possible, and would not be properly represented in the airfoil tables, and conceivably not by the aerodynamic representation within U^2NCLE. Furthermore, the results for hover are also consistent with partial laminar flow and section c_d reduced by 0.002 at low thrust (Fig. 25). It is unreasonable to expect the extent of laminar flow, both chordwise and spanwise, to be constant at all flight conditions. Therefore, a uniform adjustment in c_d is unlikely to be an accurate model; it is merely the simplest adjustment that gives good results.

Conclusions

Test data for the Joint Vertical Experimental (JVX) rotor were extensively reviewed. The data were taken on the OARF and in the NFAC at NASA Ames Research Center and included hover and high-speed cruise conditions (all axial flow). The great majority of the hover data were taken on the OARF; a much smaller data set was taken in the 40x80 wind tunnel test section. The high-speed data reported here were largely taken during the Phase II wind tunnel entry, with a limited amount of data from the Phase I entry. For these tests, cruise data were equivalent to tiltrotor airplane-mode operations.

Multiple-linear regression was used to estimate hover and airplane-mode performance from the data, with uncertainty bands about measured power in terms of classic $\pm 2s_e$ limits, plus confidence intervals and prediction intervals. The nonlinearities inherent in rotor performance were accommodated by curve fitting to ideal power from momentum theory. The results were compared to CAMRAD II and U^2NCLE performance predictions.

A new method of data selection was devised that greatly expanded the range of useable hover data. The wind tunnel data were significantly revised. Revisions included an improved method of estimating spinner drag tares and deletion of questionable thrust/torque interaction corrections. These revisions resulted in much greater consistency between Phase I and Phase II wind tunnel data. Expanded tables of hover data and revised tables of airplane-mode data are included in Appendix D.

OARF Hover Data

A quadratic curve fit to ideal hover power gave a statistically significant improvement over a linear fit. Several combinations of terms in thrust and ideal power were examined, but none showed a statistically significant improvement over the quadratic fit to ideal power (terms in $C_T^{3/2}/\sqrt{2}$ and $C_T^3/2$). The uncertainty, computed as the standard error of fit, was about 0.61 percent of maximum measured power C_P.

Corrections for swirl- and tip-loss effects gave statistically significant improvements to a linear fit, but not to the quadratic fit. Conversion from physical units to rotor performance coefficients had no statistically significant effect on uncertainty.

The previous practice of rejecting hover data with wind >1 knot was determined to be overly restrictive. Run-to-run consistency checks revealed questionable data, but also showed that additional data could be admitted. The number of useable data points was thereby more than doubled.

40x80 Airplane-Mode Data

Multiple-linear curve fits were needed to match the airplane-mode data. The fits required terms in ideal power C_{Pm} (from momentum theory, ref. 19) and profile power factor F_p (ref. 19). Nearly all of the high-speed data were taken at $M_{tip} = 0.58$, and there were no data points at the same tunnel speed but different tip speeds. The limited range of tip speeds, combined with other limitations of the data set, would render inconclusive many otherwise desirable statistical analyses.

The JVX Phase II database values of spinner drag were recalculated with a linear fit of drag versus dynamic pressure. Incorporating spinner internal pressure data into the drag calculations did not yield realistic values of net spinner drag.

The Phase II airplane-mode data matched the Phase I data only if a thrust/torque interaction term was deleted from the data conversions. Including the nominal interaction resulted in unrealistic values of propulsive efficiency.

CAMRAD II and U^{2}NCLE Predictions

The CAMRAD II predictions of references 4 and 5 were updated and combined with U^{2}NCLE predictions (ref. 6) for comparison with the expanded hover data and revised airplane-mode data. The results are summarized here.

A free-wake model with a single tip vortex matched the hover data well at high thrust, but a multiple-trailer model was needed for accuracy at low thrust. The multiple-trailer model showed little sensitivity to the radial location of the additional trailer over a reasonable range of values. However, the multiple-trailer model was computationally much less efficient than the conventional model. Differential-momentum (BEMT) and uniform-inflow models could be adjusted for a good fit to hover performance data, but required empirical corrections to do so.

Both the Corrigan and Selig stall-delay models (refs. 24 and 25) provided equally good fits to hover data. Reynolds number corrections had only a small effect on predicted hover performance, as was expected given the small difference in scale between the JVX rotor chord and the airfoils tested to develop the airfoil tables.

The U^{2}NCLE predictions matched the hover data as well as any of the CAMRAD models, except at maximum thrust where U^{2}NCLE appeared to prematurely predict stall. U^{2}NCLE predicted slightly lower airplane-mode performance than did CAMRAD, but the number of data points was too limited to permit in-depth comparisons. Both CAMRAD and U^{2}NCLE underpredicted airplane-mode performance with the default aerodynamic models. The CAMRAD predictions closely matched the wind tunnel data only after reducing blade section c_d by -0.002. These results suggest that at least partial laminar flow was achieved during the test.

Recommendations

The present work relies on fairly simple statistical analyses of curve fits to rotor performance data, namely comparisons of the standard error of estimate. Other statistics could usefully be derived from the data set. Unfortunately, too little data survive to perform a proper Pareto analysis to the standards of reference 7, which is an important motivation for many of the following recommendations.

Calibration data should be considered an integral part of the experimental database, including data for all transducers. The database should also contain as many intermediate calculations as possible, including unit and axis conversions, computation of nondimensional coefficients, and calibration corrections. It is equally important to document all data reduction equations, from individual measurements through to final calculated values. There are two distinct but related purposes: to provide better physical insight into the meaning of the results, the subtleties of which may be elusive; and to generate more detailed statistical tests, which can reveal shortcomings in the data that may bias interpretation of the results.

The intent of these recommendations is not only to facilitate troubleshooting: test planners should keep in mind that future researchers may wish to use the data for purposes not envisioned until long after the test is completed, and may therefore require different methods of analysis than normally applied to the raw data.

Similarly, provisions for uncertainty analysis should be a part of test planning. This is another motivation for retaining all calibration data. A simple example is the sensitivity of spinner drag to tunnel velocity. Spinner drag scales as V^2, and the propulsive power lost to spinner drag scales as V^3. Tests of proprotors to speeds even higher than the JVX test may find that even very small uncertainties in tunnel velocity or spinner drag measurements will have non-trivial effects on net measured rotor thrust and propulsive power.

Pretest predictions are an essential part of any test. The obvious example for the JVX data is airplane-mode performance, where the existence of CAMRAD or other predictions might have alerted the test team to potential problems with the data while the PTR and rotor were still in their as-tested condition. The discovery of an unrealistic torque/thrust interaction coefficient derived from a peculiar consistency in the mismatch of CAMRAD predictions to data. As it stands, there is no way to rigorously determine whether the failure to match predictions with the nominal database values is due to transducer failure, data processing error, corruption of the database, or modeling error.

Appendix A: JVX Wind Tunnel Hover Data

A limited amount of hover data were taken during the 1998 Phase I entry in the 40x80 test section. The overhead doors, high-bay doors, 40x80 exhaust louvers, and main air exchange were all open to minimize recirculation; see references 2 and 14 for details. The rotor shaft was tilted 2.5 deg nose up, which represented the V-22 nacelle outboard cant. Most of the hover data were taken with the rotor facing downstream, the reverse of that used for high-speed data, and with the image plane installed but the wing removed; average $M_{tip} = 0.709$.

A few data points were taken with the rotor facing upstream without the image plane or wing. The upstream test condition gave poor results, which are not shown here. An extremely limited amount of hover data were taken during the 1991 Phase II 40x80 test. The results were very poor, with excessive scatter, and are accordingly not shown here.

Figure A-1 shows the wind tunnel data from the Phase I test (downstream orientation, $M_{tip} = 0.709$) superimposed on the OARF data at $M_{tip} = 0.728$ (Run 7). For the wind tunnel data, there was residual wind in the test section, measured to be 8–16 knots. The wind tunnel data in Figure A-1 have not been corrected for wind. Attempts to correct for wind using the methods of reference 1 yielded unrealistically low values of figure of merit.

The reason for the unsatisfactory wind corrections is unknown. Attempts to fit the data with terms in C_{Pm} and F_p (Eqs. 12 and 14) also failed to give usable results. All of the these corrections require accurate measurements of free-stream velocity, which is problematic for a large rotor in the 40x80 test section. The data set contains measurements of tunnel speed from only one set of transducers, so there is no way to retroactively determine velocity variations along the length of the test section, nor to determine recirculation velocity independent of test section velocity. For this reason, there was no further attempt to statistically analyze the wind tunnel data.

The reason for the shortfall in figure of merit at high thrust in the wind tunnel is also unknown. One would expect to see a slight reduction in performance because of the larger cuff, but the magnitude of the cuff effect should be very small for the JVX rotor. The slight reduction in tip speed and the small residual wind should result in an increase in performance, not a decrease.

These caveats aside, the OARF and 40x80 data are encouragingly close. Neither 40x80 entry had measurement of isolated-rotor hover performance as a primary objective. There appears to have been little or no previous attempt to closely compare 40x80 data to OARF data. The results presented here suggest that the 40x80 test section—or more realistically, the 80x120 test section—with careful attention to rotor installation, flow control and low-speed velocity measurement, may yet become a viable facility for measuring proprotor hover performance.

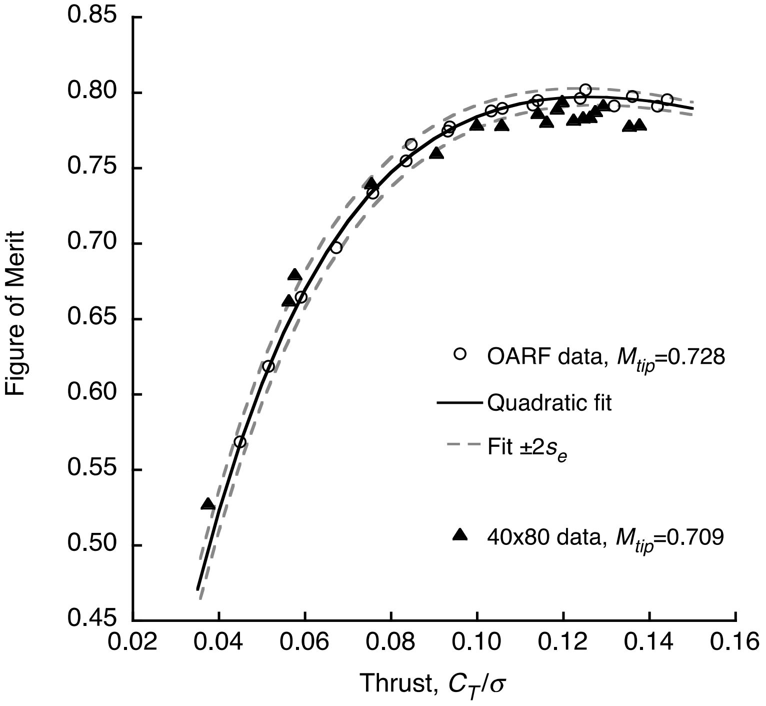

Figure A-1. JVX 40x80 hover data at M_{tip} = 0.709, downstream orientation, superimposed on OARF data at M_{tip} = 0.728.

Appendix B: Analysis of Spinner Drag Tares

Alternative Interpretations of Spinner Tare Data

A few of the pitfalls in statistical analysis can be illustrated with the spinner tare data from the Phase I wind tunnel test. Data were taken with the rotor blades removed over a range of airspeeds from 131 to 238 knots. For the data discussed here, the spinner was rotating at 495 rpm. Data were taken at three different yaw (ψ_s) angles: 0, 3, and 6 deg. No spinner tare measurements were taken for the JVX Phase II entry.

The Phase I spinner tare data in Figure 32 are replotted in Figure B-1, in units of equivalent flat-plate area (drag/q_0) versus tunnel dynamic pressure (q_0). Most of the data fall into three distinct, narrow bands, one for each yaw angle. The trends are highly linear, except for the data point at zero yaw, 131 knots, or $q_0 = 56$ lb/ft^2 (marked with a solid symbol in the plot).

Reference 2 shows an additional, off-trend data point for $\psi_s = 0$ at just over 200 knots (roughly 130 lb/ft^2 in Figure B-1). No comparable data could be recovered from the data set for the analyses described here. The data in Figure A2 of reference 2 are adjusted for internal spinner pressure, and therefore are of lower magnitude than shown here. For the present report, pressure corrections were rejected for reasons discussed later in this appendix.

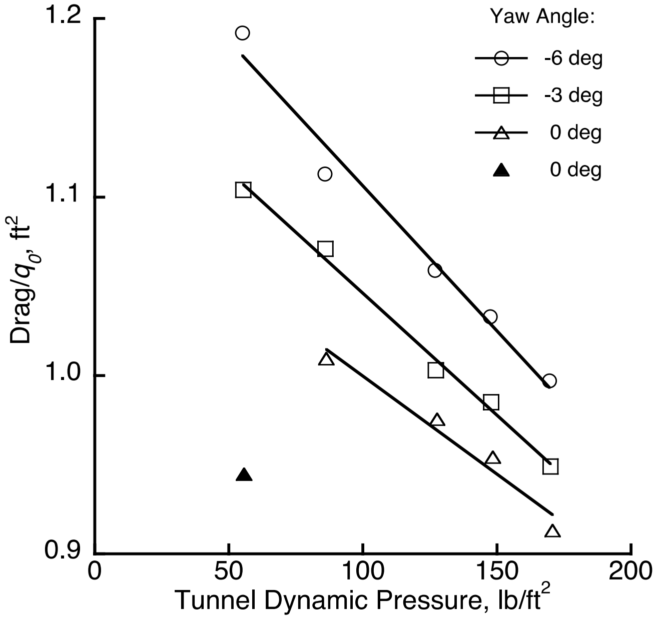

Figure B-1. Phase I spinner tare data at 495 rpm, plotted as flat-plate area versus dynamic pressure.

Linear curve fits are shown for each yaw angle. The anomalous data point at zero yaw, 56 lb/ft^2, is not included in any curve fit. The fits are consistent, in that no two slopes are statistically different from each other. That is, even though slight differences are visible, the scatter in the data is too large to reliably calculate those differences. However, the dependent variable is divided by the independent variable. The data transformation more clearly reveals the anomaly at $q_0 = 56$ lb/ft^2 but violates the assumptions underlying the classic curve fitting method used here. A curve fit to drag versus q_0, as in Figure 32, should give more reliable results.

It is unlikely that the spinner would have highly nonlinear drag behavior only at zero yaw near 130 knots (50 lb/ft^2 in Figure B-1) and linear behavior elsewhere. A deeper look at the database reveals that this is the first data point taken during that run, which hints at a measurement problem. Two possibilities are explored in the following sections.

The total force on the exposed spindles should vary with q_0, but that force projected in the longitudinal and circumferential directions should result in drag and torque trends that vary with slightly different functions of airspeed. In principle, it should be possible to separate spindle drag from total drag by comparing the different trends. However, the torque measured during the tare runs was 0.1 percent of full scale at best, and sometimes much less, which is far too low for reliable analysis. Again, the curve fit of Figure 32 is the more reliable method.

Balance Hysteresis

Reference 11 plots PTR balance check-loads data in terms of measurement error versus applied thrust. The balance data were collected during tests of the Advanced Technology Blade (ATB) (ref. 11), but the test rig, balance, and rotor hub were identical to those used for all JVX tests reported herein. Figure B-2, reconstructed from reference 11, clearly shows hysteresis at low thrust, separate nonlinear trends for "up" and "down" data, plus a large anomaly at about 1000 lb applied thrust. The anomalous data, plus the nonlinearities, make curve-fitting problematic. Nevertheless, it is instructive to estimate the hysteresis by averaging the "up" and "down" values separately for data at 2000 lb applied thrust and above. The result is a nominal hysteresis of 5.5 lb (±2.75 lb).

If the curve fit in Figure B-1 to spinner drag at 0-deg yaw is extrapolated to $q_0 = 56$ lb/ft^2, the predicted value of spinner drag is 1.05 ft^2, and the difference between the predicted and measured values is 0.10 ft^2, equivalent to 5.6 lb—almost exactly the estimated value of hysteresis. While the near-perfect match is most likely a coincidence, the evidence is strongly suggestive that the first data point for spinner drag (the solid symbol in Figure B-1) does not represent the correct trend line and should not be used for curve fitting. Moreover, the balance hysteresis appears to be much worse at the low-thrust levels corresponding to spinner drag. Unfortunately, there are no balance check-loads data at negative thrust to directly compare the spinner drag data against.

A different possible explanation of the anomalous data point is presented in the following section, in the discussion of Figure B-3.

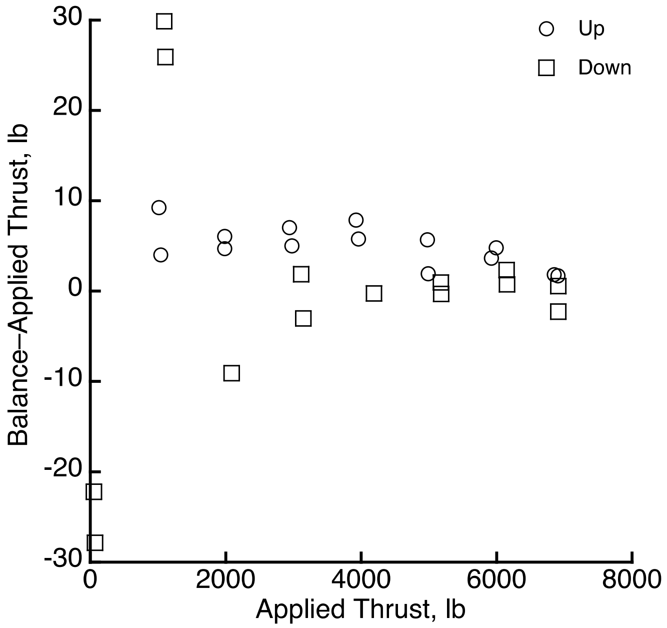

Figure B-2. PTR balance thrust-measurement error (Ref. 11, Fig. 6.3).

Spinner Pressures

Reference 2 discusses spinner pressure measurements, reconsidered here. In traditional propeller tests with an external balance, aerodynamic loads on the spinner and nacelle must be measured and subtracted from the measured axial force to get net propeller thrust. The spinner may experience both external drag forces and internal pressure forces, both of which must be taken into account. In contrast, the JVX tests used an internal balance that was shielded from aerodynamic loads. A tacit assumption is that the PTR cowling did indeed shield the balance from aerodynamic effects, and that internal pressures on the upstream and downstream sides of the balance were equal. The internal balance was added to the PTR after the XV-15 tests, so one must be careful when comparing XV-15 and later data.

To determine the effects of spinner pressures, the difference between the measured internal pressure and free-stream static pressure is required. The JVX spinner was open at the rear, so the net load caused by internal pressure was calculated by multiplying the pressure by the projected spinner area (the area of the base of the spinner). The presence of the spinner openings makes this an imprecise calculation.

Measured spinner pressures were always lower than free-stream static pressure, hence the net spinner pressure force was always negative in the thrust direction.

Internal spinner pressures were measured during both the Phase I and Phase II tests, but the transducer configuration was changed so no direct comparison is possible. Two indirect methods of correcting the data were tried, as discussed next.

Reference 2 estimated spinner tares for the Phase I tests by subtracting the internal spinner pressures, times the projected area, from the total force measured by the rotor balance. However, the resulting net spinner drag, with blade spindles exposed, was less than that measured during the XV-15 tests with spindles removed (ref. 15). While not physically impossible, this result is not very credible. It cannot be determined whether the XV-15 data or the JVX data, or both, are incorrect.

The procedure described above was repeated with the Phase I tare data and the Phase II pressure data, which as noted had a different transducer installation. However, this gave unrealistic results for the Phase II data: the resulting spinner drag was much too large (equivalent to about 4 ft^2 frontal area). The Phase II pressure data were much greater in magnitude than the Phase I data, which is again unrealistic. It has been conjectured that the static pressures were misrecorded or improperly applied to the data, but this has not been proven. The discrepancy may merely be an artifact of mislabeled data, but no alternative interpretation of the database has yielded reasonable results, so this matter has not been further pursued. Selected Phase II pressure data are included in Appendix D, in the event that someone wishes to try their hand with a different approach to the problem.

An alternative method is to use the Phase I pressure data to correct the spinner tares for the presence of the rotor blades, then use the same trend for Phase II, thereby avoiding the need to use any Phase II pressure data. The Phase I test acquired both blades-on and blades-off pressure data. An equivalent blades-on tare can be calculated as:

blades-on tare = blades-off drag – blades-off pressure + blades-on pressure

where drag is the total force measured by the rotor balance, and the spinner pressures have been converted to net drag forces. Alternatively, drag and pressure forces may be converted to equivalent flat-plate areas.

Both sets of Phase I pressure data, blades-on and blades-off, showed approximately linear trends with tunnel dynamic pressure q_0 (but see Figure B-3). The trends were converted to flat-plate areas and combined with the raw drag data (Fig. B-1) to get a corrected spinner tare. However, the resulting effective spinner drag was unrealistically high: about 1.7 ft^2, which is much higher than that reported for the XV-15 tests (ref. 15).

A closer look at the spinner pressure data is revealing. The pressure data taken during the Phase I spinner tares are plotted versus q_0 in Figure B-3, transformed into force/q_0 to emphasize the nonlinearities. The previous caveat concerning the interpretation of data so transformed applies. Perfect spinner pressures would presumably fall on a straight, horizontal line. It is evident that the trends with q_0 are not only nonlinear, but vary inconsistently with yaw angle. Curve-fitting is unlikely to give reliable results.

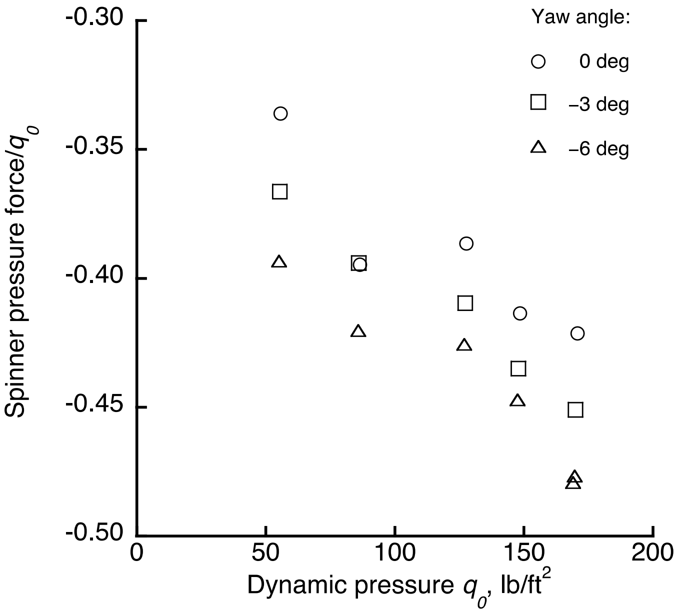

Figure B-3. Phase I spinner tare internal pressure data.

The spinner tare data in Figure B-1 include the effects of spinner pressure. In Figure B-3, the trend in the data for $\psi_s = 0$ is very different if the first data point is excluded. If the trend *without* the first data point is correct, then the first data point is off-trend in the same direction as the presumed hysteresis effect, and of similar magnitude. The anomalous data point in Figure B-1 can possibly be explained as an effect either of hysteresis in the balance data or of scatter in the pressure data, but there is no way to determine which, if either, actually applies.

There are several ways to approach the problem of erratic pressure data. A partial list includes (1) delete the first data point and fit to the remaining data at $\psi_s = 0$; (2) fit to all of the data, with or without the first point; (3) apply curve fits to the pressure data separately from the balance data; or (4) fit to all of the data at $\psi_s = 0$. The last of these methods was chosen for this paper, using a linear curve fit, on the grounds that it makes the fewest assumptions about the nature and quality of the data. The results are shown in Figure 32 in the main body of this paper. No attempt was made to correct for presumed hysteresis in the balance or nonlinear trends of spinner pressure versus q_0.

Appendix C: Glauert Blockage Correction

The shortfall in CAMRAD II predicted propulsive efficiency can, perhaps, be partially explained by wind tunnel flow blockage effects. The method used here was originally developed by Glauert (ref. 29); the equations below are taken from reference 30, here rewritten in terms of helicopter thrust coefficient.

In the wind tunnel, the influence of the test section walls changes the flow conditions at the rotor disk relative to what would exist in free-stream flow (that is, with an infinitely large wind tunnel). The Glauert correction derives an equivalent free-stream velocity V' at which the rotor will experience the same axial velocity as in the wind tunnel, and for which "this condition will maintain the same working conditions for the airscrew blades" (ref. 29).

Let $\tau = T/\rho A V^2 = C_T/\mu^2$, and $\alpha_1 = A/C$, where C = wind tunnel cross-section area. The Glauert correction is then

$$\frac{V'}{V} = 1 - \frac{\tau\alpha_1}{2\sqrt{1+2\tau}}.$$

For any combination of μ and C_T/σ, the nominal value of η is first calculated, along with V'/V. C_T/σ and C_Q/σ are the same at V and V', but η', the propulsive efficiency in free air, is recalculated as $\eta' = \eta V'/V$.

Figure C-1 shows the data with and without the Glauert correction. The open symbols are the nominal data with spinner tare corrections and thrust bias adjustment applied (the same data as in Figure 28). The dots are the data with the Glauert correction.

The figure shows that the Glauert correction has little effect except at the highest values of C_T/σ. At the maximum value of C_T/σ, the Glauert correction is 1.01 percent, which is slightly less than the $\pm 2s_e$ uncertainty band in the data (Eq. 15). However, the trend is consistent and suggests that the correction may be significant at higher values of C_T/σ, at least at low μ; the effect is negligible at low C_T/σ and high μ. Furthermore, V'/V was calculated using a literal interpretation of the Glauert formula, with no allowance made for the wind tunnel's non-circular cross section (visible in Figure 2), nor with any other blockage correction, such as for the PTR's long afterbody. The blockage effect could easily be larger than shown here. The trend in the reduction in η is consistent with the CAMRAD II predictions at high C_T/σ (Fig. 45). However, the adjustment, even if significant, cannot by itself explain the discrepancy between the predictions and the data.

A more subtle consideration is that the Glauert correction assumes a uniform change in velocity across the rotor disk, even for large α_1. The JVX rotor would have in fact experienced a non-uniform radial inflow perturbation, which could combine with non-ideal circulation distribution to further change the effective η. Although frankly speculative, this assumed effect could be important for rotors operating at combined high thrust and off-design V or V_{tip}.

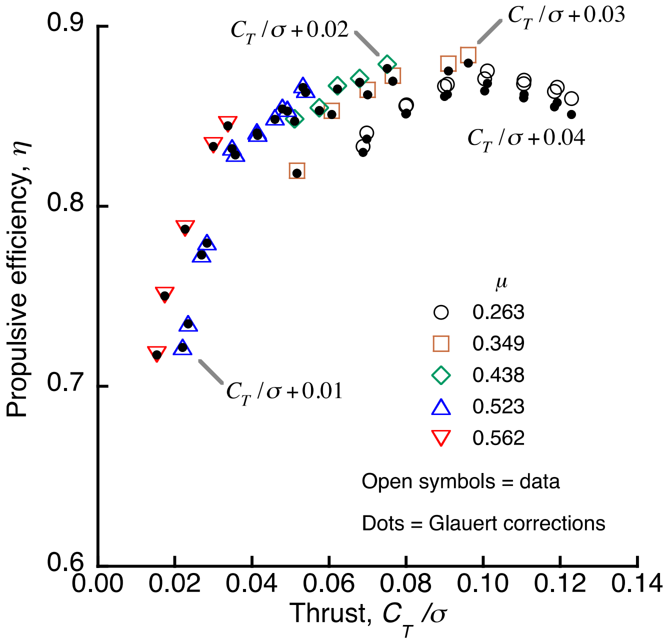

Figure C-1. Measured JVX propulsive efficiency with and without Glauert blockage corrections. The nominal data are the same as in Figure 28.

Far more sophisticated blockage corrections have been developed; reference 31 includes comparative data for three methods and provides a list of further references. A deeper study of blockage corrections appropriate for proprotors is recommended, but is beyond the scope of the present inquiry.

Appendix D: JVX Test Data

The JVX 1984 hover (ref. 1) and 1991 airplane-mode data used for this report are tabulated here, as extracted from the Rotor Data Reduction System (RDRS) database. They generally include the highest quality data that could be extracted from archives, but do not constitute the complete test data set. The data presented in this appendix include corrections for hub drag, as detailed in Appendix B. Limited data from the JVX 1988 airplane-mode test (ref. 2) are also included.

JVX Hover Data

The JVX hover data presented in the main body of this report are a subset of the data in reference 1 (Test 911). These test conditions are rotor only (no wing or ground plane) for M_{tip} = 0.67–0.68. Table D-1 lists the data meeting these criteria. C_P and FM are corrected for ambient wind using the methodology described in reference 1.

A more limited set of hover data was taken at M_{tip} = 0.73 and is listed in Table D-2. These data were used for comparison with 40x80 hover data in Appendix A.

A few hover data points were taken in the wind tunnel during the 1988 Phase I entry. See Appendix A for discussion. The "downstream" data are listed in Table D-3.

For all comparisons between data and theory (CAMRAD II predictions) in the main body of this report, the values of V_{tip}, M_{tip}, and ρ were averaged at each test condition, and ambient wind was assumed to be zero for the predictions.

Table D-1. JVX OARF hover data (ref. 1), rotor only, M_{tip} = 0.67–0.68.

Run	Point	V_{tip} (ft/sec)	M_{tip}	Wind (knots)	ρ (slug/ft^3)	C_T/σ	C_P/σ	*FM*
1	10	752.8	0.6768	0.81	0.002406	0.02311	0.002632	0.3183
1	11	752.8	0.6765	0.75	0.002404	0.03479	0.003107	0.4981
1	12	752.7	0.6765	1.79	0.002404	0.04504	0.003853	0.5916
1	13	752.5	0.6762	0.64	0.002403	0.06134	0.005232	0.6926
1	16	752.4	0.6760	1.44	0.002403	0.08027	0.007163	0.7572
1	17	752.3	0.6759	1.45	0.002403	0.07977	0.007211	0.7451
2	9	759.3	0.6765	1.78	0.002359	0.04352	0.003721	0.5819
2	11	759.2	0.6761	0.87	0.002357	0.06159	0.005384	0.6771
2	12	759.1	0.6760	1.07	0.002357	0.06894	0.006095	0.7084
2	13	759.0	0.6755	1.61	0.002354	0.07559	0.006839	0.7248
2	14	758.9	0.6755	0.83	0.002354	0.08395	0.007577	0.7657
2	15	758.7	0.6753	-0.09	0.002354	0.09729	0.009185	0.7879
2	16	758.6	0.6752	0.13	0.002354	0.10291	0.009947	0.7916
2	17	760.6	0.6766	0.85	0.002351	0.11551	0.011682	0.8015
2	20	760.2	0.6769	1.97	0.002356	0.13034	0.014238	0.7883
2	21	759.8	0.6769	1.47	0.002359	0.14504	0.016467	0.8000
2	22	759.6	0.6760	-0.14	0.002354	0.16001	0.018856	0.8095
3	4	746.8	0.6758	2.10	0.002436	0.05091	0.004433	0.6180
3	5	746.7	0.6757	1.98	0.002436	0.05791	0.005080	0.6542
3	6	746.6	0.6753	1.59	0.002433	0.06374	0.005692	0.6742
3	7	746.5	0.6749	1.56	0.002431	0.07119	0.006339	0.7146
3	8	746.4	0.6747	0.62	0.002430	0.08109	0.007315	0.7529
3	9	746.3	0.6745	0.62	0.002430	0.09365	0.008545	0.7999
3	10	746.1	0.6743	0.98	0.002429	0.10685	0.010008	0.8324
3	11	749.5	0.6772	0.94	0.002428	0.11303	0.011202	0.8090
3	12	749.3	0.6769	0.90	0.002427	0.12562	0.012886	0.8240
3	13	749.2	0.6767	0.98	0.002426	0.13269	0.013941	0.8269
4	5	754.4	0.6773	0.64	0.002396	0.02382	0.002728	0.3213
4	6	754.3	0.6772	0.76	0.002396	0.03422	0.003209	0.4704
4	7	754.2	0.6771	0.92	0.002396	0.04635	0.004036	0.5896
4	8	754.1	0.6770	0.89	0.002396	0.06152	0.005300	0.6867
4	9	754.0	0.6768	0.95	0.002395	0.06986	0.006087	0.7234
4	10	753.9	0.6765	1.23	0.002394	0.07886	0.006938	0.7612
4	11	753.8	0.6765	0.98	0.002394	0.08727	0.007819	0.7863
4	12	753.7	0.6763	1.57	0.002394	0.09578	0.008948	0.7901
4	13	753.5	0.6762	1.37	0.002394	0.10754	0.010346	0.8130
4	14	753.3	0.6758	1.20	0.002393	0.11753	0.011826	0.8126
4	15	753.1	0.6756	0.54	0.002393	0.12731	0.013204	0.8205
4	16	752.9	0.6755	0.90	0.002393	0.13770	0.014849	0.8208
4	17	752.7	0.6751	0.99	0.002392	0.14523	0.016247	0.8124
5	3	756.7	0.6766	2.02	0.002375	0.04246	0.003730	0.5594
5	5	756.5	0.6765	2.09	0.002376	0.05729	0.005007	0.6532
5	9	756.0	0.6760	2.10	0.002375	0.09367	0.008809	0.7762
5	13	755.4	0.6756	1.77	0.002377	0.13272	0.014366	0.8027
5	16	756.6	0.6767	1.80	0.002377	0.04777	0.004208	0.5918

Table D-1. JVX OARF hover data (ref. 1), rotor only, M_{tip} = 0.67–0.68 (continued).

Run	Point	V_{tip} (ft/sec)	M_{tip}	Wind (knots)	ρ (slug/ft^3)	C_T/σ	C_P/σ	*FM*
5	22	755.9	0.6760	1.79	0.002376	0.09807	0.009469	0.7736
5	24	755.6	0.6755	1.21	0.002375	0.11672	0.012109	0.7854
5	27	754.9	0.6748	1.60	0.002374	0.14760	0.016999	0.7956
6	6	755.6	0.6761	-0.05	0.002383	0.04507	0.004000	0.5704
6	7	755.5	0.6756	0.48	0.002380	0.05198	0.004569	0.6187
6	8	755.4	0.6753	0.47	0.002378	0.06558	0.005836	0.6863
6	9	755.4	0.6751	0.55	0.002377	0.06955	0.006163	0.7098
6	10	755.3	0.6749	0.42	0.002376	0.07684	0.006899	0.7364
6	11	755.2	0.6746	0.41	0.002375	0.08674	0.007949	0.7665
6	12	755.0	0.6745	0.13	0.002375	0.09636	0.009116	0.7825
6	13	754.9	0.6742	0.42	0.002373	0.10636	0.010391	0.7961
6	14	758.1	0.6768	1.73	0.002371	0.11727	0.011879	0.8063
6	15	757.9	0.6766	2.11	0.002371	0.12788	0.013520	0.8067

Table D-2. JVX OARF hover data (ref. 1), rotor only, M_{tip} = 0.73.

Run	Point	V_{tip} (ft/sec)	M_{tip}	Wind (knots)	ρ (slug/ft^3)	C_T/σ	C_P/σ	*FM*
7	4	818.1	0.7289	1.23	0.002361	0.05151	0.004507	0.6186
7	5	818.0	0.7288	1.46	0.002361	0.05911	0.005158	0.6645
7	6	817.9	0.7285	1.42	0.002359	0.06726	0.005966	0.6973
7	7	817.8	0.7283	1.14	0.002358	0.07575	0.006780	0.7334
7	8	817.7	0.7280	1.61	0.002357	0.08467	0.007675	0.7657
7	9	817.5	0.7279	1.83	0.002357	0.09361	0.008788	0.7773
7	10	817.4	0.7276	1.55	0.002356	0.10584	0.010401	0.7896
7	11	817.2	0.7274	1.86	0.002356	0.11405	0.011557	0.7948
7	12	818.4	0.7286	1.13	0.002357	0.12394	0.013069	0.7962
7	13	818.0	0.7284	1.05	0.002358	0.13605	0.015008	0.7975
7	14	817.8	0.7279	1.41	0.002356	0.14416	0.016413	0.7954
7	15	819.1	0.7289	1.83	0.002354	0.08346	0.007619	0.7547
7	18	818.5	0.7285	2.02	0.002355	0.11293	0.011431	0.7918

Table D-3. JVX hover data, isolated rotor in the 40x80 test section, downstream orientation, $M_{tip} = 0.71$. Tunnel velocity V is induced by the rotor.

Run	Point	V_{tip} (ft/sec)	M_{tip}	V (knots)	ρ (slug/ft^3)	C_T/σ	C_P/σ	*FM*
4	10	799.8	0.7084	8.39	0.002303	0.03747	0.009603	0.5277
4	11	799.8	0.7084	10.67	0.002303	0.05627	0.003291	0.6624
4	12	795.9	0.7054	14.98	0.002306	0.09990	0.004859	0.7788
4	13	797.2	0.7071	13.18	0.002310	0.11414	0.009628	0.7865
4	14	803.7	0.7130	15.94	0.002311	0.11860	0.011502	0.7895
4	15	802.4	0.7120	13.80	0.002313	0.11975	0.012373	0.7944
4	16	797.2	0.7078	10.80	0.002317	0.05764	0.012589	0.6796
4	17	799.8	0.7104	11.83	0.002319	0.07548	0.004823	0.7400
4	18	801.1	0.7116	10.16	0.002320	0.09055	0.006664	0.7602
4	19	798.5	0.7094	13.16	0.002320	0.10573	0.008606	0.7785
4	20	799.8	0.7108	16.32	0.002322	0.11616	0.010494	0.7807
4	21	798.5	0.7099	14.36	0.002323	0.12241	0.012128	0.7821
4	22	794.6	0.7065	14.92	0.002324	0.12745	0.013185	0.7878
4	23	797.2	0.7089	15.14	0.002325	0.12461	0.013684	0.7837
4	24	795.9	0.7077	13.14	0.002325	0.12620	0.013431	0.7839
4	25	797.2	0.7090	13.14	0.002326	0.12929	0.013592	0.7916
4	26	793.3	0.7057	16.30	0.002327	0.13539	0.014138	0.7780
4	27	790.6	0.7035	12.88	0.002328	0.13769	0.015364	0.7789

JVX Airplane-Mode Data

The JVX airplane-mode data tabulated here are a subset of the 1991 Phase II database (Test 579). A limited amount of data from Phase I (1988, Test 568) are also included. Because of uncertainty in the measurement of rotor performance at very low wind tunnel speed, data below 30 knots are not included in this report. The Phase II rotor performance data presented here are limited to five advance ratios. The objective is to prove a wide range of advance ratios with the constraint that each advance ratio must include data covering a reasonable range of thrust coefficients. There was a further requirement that rotational speed be constant at a given tunnel speed, but this eliminated only one data point.

Mean operating conditions and the C_T/σ range for each chosen advance ratio are listed in Table D-4. See also Tables 5 and 7 in the main body of this report.

RDRS database label definitions and units are listed in Table D-5. The data are listed in Tables D-6 and D-7 using the data labels in the database; data that were rederived have column labels in italics. The data are sorted by advance ratio, then run and point number. Derivative data that can be readily recalculated, such as helical tip Mach number, are generally not included in the tables. In addition, spinner pressure data are listed in Tables D-8 and D-9, and spinner drag tare data from the Phase I test are listed in Table D-10.

Table D-4. JVX summary cruise operating conditions and thrust ranges.

(a) 1988 Phase I entry (Test 568)

μ	V_{tip} (ft/sec)	V (knots)	C_T/σ
.210	646	80	.040–.061
.259	650	100	.050–.089
.344	650	132	.022–.038

(b) 1991 Phase II entry (Test 579)

μ	V_{tip} (ft/sec)	V (knots)	C_T/σ
.263	638	100	.029–.085
.349	640	132	.022–.068
.438	641	166	.031–.057
.523	642	199	.011–.045
.562	695	231	.016–.034

Power coefficient calculations

The power coefficient C_P/σ (CPS) is calculated by the following equations in the database specifications:

CPS = CP / SIGMA

CP = TORQC / (DENOM * R)

DENOM = RHO × AREA × VTIP**2

where RHO is the air density and AREA is the total disk area. VTIP data are sometimes labeled OMEGA*R in the database.

For all wind tunnel data plots in this report, C_P/σ and C_Q/σ were recalculated from the rotor torque data using the above formulas. The data stored in the Phase II database as CPS (for C_P/σ) plot with severe scatter and are not presented here (the Phase I data appear to be correct). The cause of the anomalies in the stored data was not determined.

Table D-5. JVX data labels, definitions, and units.

Label	Symbol(s)	Definition and units
`AFFLEX`	X_s	instrumented shaft axial force, lb
`AFRB`	X_c	rotor balance axial force with shaft corrections, lb
`AFRBC`	X_b	rotor balance axial force, lb
`COLL`		rotor blade collective pitch, deg
`CTISS`	C_T/σ	rotor thrust coefficient, divided by solidity
`ETAIS,F`	η	rotor propulsive efficiency
`DSP`		spinner drag, lb
`KAFXTQ`	K_{QT}	shaft torque/thrust interaction constant, ft-lb/lb
`KTQAFX`	K_{TQ}	shaft thrust/torque interaction constant, lb/ft-lb
`MTUN`		tunnel Mach number
`PSI`	ψ_s	yaw angle, deg
`QPSF`	q_0	corrected tunnel dynamic pressure, lb/ft^2
`RHO100`	ρ	tunnel air density, slug/ft^2 (inconsistent scales in database)
`RPM`	Ω	rotor rotational speed, rpm
`RTRDFS`		rotor drag force, including spinner loads, lb
`SPBP`		spinner base pressure (Phase I test), lb/in^2
`SPBPR`		spinner base pressure (Phase II test), lb/in^2
`SPBPI1`		" " " " " " "
`SPBPI2`		" " " " " " "
`SPBSF`		spinner base force, positive in thrust direction, lb
`TEMP`		total tunnel temperature, deg F
`TIPM`	M_{tip}	rotor tip Mach number
`TORQ`	Q_s	instrumented rotor shaft torque, ft-lb
`TORQC`		corrected rotor shaft torque, ft-lb
`VKTS`	V	tunnel air velocity, knots
`VTIP`	$V_{tip} = \Omega R$	rotor tip speed, ft/sec (also `OMEGA*R`)
`V/OR`	$\mu = V_{tip}/V$	rotor advance ratio

Several different types of corrections were applied to the data in the database. Tunnel dynamic pressure QPSF is corrected for compressibility. Rotor shaft torque TORQC is corrected for shaft force interaction. Rotor balance axial force AFRBC is corrected for balance interactions. Rotor drag force RTRDFS is the rotor balance axial force corrected for rotor shaft axial force and torque interactions (positive in drag direction). Not all interactions were applied to the Phase II data given in this report, as described next.

Interactions

The values given in the Phase II database for rotor shaft torque/thrust interaction are suspect, as detailed in the section Torque/Thrust Interactions in the main body of this report. The defining equation is Eq. 11, here rewritten with database labels from Table D-5:

$$\mathrm{AFRB} = \mathrm{AFRBC} + \mathrm{AFFLEX} - \mathrm{KTQAFX} \times \mathrm{TORQ}$$

The counterpart equation for torque is

$$\mathrm{TORQC} = \mathrm{TORQ} - \mathrm{KAFXTQ} \times [\ \mathrm{AFFLEX} - (\mathrm{KTQAFX} \times \mathrm{TORQ})\ ]$$

TORQ does not include corrections for shaft torque/thrust interaction or bearing friction, whereas TORQC includes these corrections. The raw values of AFRBC, AFFLEX, and TORQ are included in the tables for reference. (AFRBC data are not available for Phase I.) The nominal interaction coefficients are different for Phase I and Phase II:

Test	KTQAFX lb/ft-lb	KAFXTQ ft-lb/lb
Phase I	−0.0023	0.2089
Phase II	−0.0086	0.2143

For the Phase II data, axial force and torque were recalculated with KTQAFX set to zero, then spinner tares added, and finally the coefficients C_P/σ, C_Q/σ, and η computed. The nominal corrections were retained for Phase I.

Drag corrections

In the database, rotor drag force (negative thrust) is defined as

$$\mathrm{RTRDF} = \mathrm{RTRDFS} - \mathrm{DSP} + \mathrm{SPBSF}$$

Here DSP is the spinner drag tare (stored as equivalent drag area), and SPBSF is the spinner base force calculated from internal spinner pressure. However, DSP data were not stored for Phase II, and spinner base force gives unreasonable results. Furthermore, if DSP is the spinner drag tare, then SPBSF should reflect the *difference* between the blades-on and blades-off pressures, not the literal pressure.

For this report, net rotor thrust is recalculated as

$$T = -\mathrm{RTRDFS} + \mathrm{QPSF} \times A_{sp}$$

where $A_{sp} = 0.901$ ft^2, as detailed under JVX Spinner Tares in the main body of this report. The values of rotor thrust, torque, and related coefficients plotted in the main body of this report were recalculated using the equations immediately above.

Allowing for the possibility that some of the data were simply mislabeled or misinterpreted, or that better means of correcting the data may be devised, the original values of RTRDFS, CTISS, SPBSF, and ETAIS,F are included in the tables of this appendix, along with the values corrected as explained previously.

Not all data were stored for all tests. In particular, the *uncorrected* values of shaft torque (TORQ) were stored only for the wind tunnel tests, making it impossible to recalculate rotor axial force for hover data in the same manner as was done here for the Phase II data. As already mentioned, rotor balance axial force (AFRBC), uncorrected for shaft interactions, was not stored for Phase I. Accordingly, all hover data in Tables D-1, D-2, and D-3 use rotor thrust exactly as in the database.

Caution is advised when comparing these data with RDRS data from other tests. RHO100 usually means 100 times density, as in Table D-6a, but the multiplication was evidently not applied to the JVX Phase II test data (Table D-7a).

Table D-6a. JVX 1988 Phase I airplane-mode operating conditions.

Run	Point	TEMP	RHO100	VTIP	VKTS	V/OR	TIPM	MTUN	RPM	QPSF
35	6	78.81	0.2264	642.7	80.2	0.2106	0.5658	0.1191	491	20.7
35	7	79.60	0.2261	646.6	80.3	0.2097	0.5688	0.1193	494	20.8
35	8	80.38	0.2257	649.3	80.6	0.2095	0.5707	0.1195	496	20.9
37	3	73.68	0.2276	650.6	99.3	0.2576	0.5759	0.1483	497	32.0
37	4	75.10	0.2269	649.3	99.9	0.2598	0.5740	0.1491	496	32.3
37	5	78.06	0.2243	648.0	131.8	0.3433	0.5722	0.1964	495	55.5
37	6	78.65	0.2240	650.6	132.4	0.3434	0.5742	0.1972	497	55.9
37	7	79.22	0.2237	650.6	132.5	0.3438	0.5739	0.1973	497	56.0
37	8	79.99	0.2234	651.9	132.7	0.3436	0.5746	0.1974	498	56.0

Table D-6b. JVX 1988 Phase I rotor performance data, as given in the database.

Run	Point	RTRDFS	AFFLEX	COLL	TORQ	TORQC	SPBP
35	6	-2087.9	-30.4	20.21	6471	6450	-0.0624
35	7	-2395.8	-19.4	20.68	7357	7334	-0.0642
35	8	-3212.6	-2.0	21.90	9864	9833	-0.0668
37	3	-2657.2	-31.0	24.97	9945	9914	-0.0827
37	4	-4727.4	5.7	28.35	17791	17764	-0.0920
37	5	-1100.5	-605.2	29.90	5991	6098	-0.1440
37	6	-1960.4	-373.8	30.83	9871	9926	-0.1451
37	7	-2785.4	-95.4	31.96	13795	13790	-0.1478
37	8	-3516.7	-63.6	32.76	17175	17162	-0.1500

Table D-6c. JVX 1988 Phase I rotor performance data, original (text labels) and as recalculated (italic symbols).

Run	Point	ETAIS,F	CTISS	T	C_T/σ	C_P/σ	η
35	6	0.8520	0.03996	2106.5	0.04032	0.00988	0.8596
35	7	0.8563	0.04537	2414.5	0.04572	0.01111	0.8630
35	8	0.8554	0.06044	3231.4	0.06079	0.01480	0.8604
37	3	0.8631	0.04939	2686.0	0.04992	0.01474	0.8724
37	4	0.8642	0.08846	4756.5	0.08900	0.02659	0.8695
37	5	0.7746	0.02093	1150.5	0.02188	0.00928	0.8097
37	6	0.8477	0.03702	2010.7	0.03797	0.01500	0.8694
37	7	0.8681	0.02922	1423.3	0.02679	0.00904	0.7765
37	8	0.8801	0.04088	2050.9	0.03847	0.01228	0.8227

Table D-7a. JVX 1991 Phase II airplane-mode operating conditions (Test 579).

Run	Point	TEMP	RHO100	VTIP	VKTS	V/OR	TIPM	MTUN	RPM	QPSF
4	6	56.60	0.002332	637.8	99.5	0.2633	0.5739	0.1511	487.2	32.9
4	7	56.72	0.002331	638.7	99.6	0.2631	0.5746	0.1512	487.9	32.9
4	8	56.97	0.002330	635.8	99.7	0.2646	0.5719	0.1513	485.7	33.0
4	9	57.20	0.002329	639.8	99.5	0.2625	0.5754	0.1510	488.8	32.8
4	10	57.25	0.002329	641.8	99.6	0.2618	0.5771	0.1511	490.3	32.9
4	11	57.52	0.002327	638.5	100.2	0.2648	0.5740	0.1520	487.8	33.3
4	12	57.55	0.002327	640.9	100.2	0.2638	0.5762	0.1520	489.6	33.3
8	5	52.74	0.002355	635.5	98.7	0.2621	0.5739	0.1504	485.5	32.7
8	6	53.00	0.002354	636.8	99.1	0.2627	0.5750	0.1510	486.4	32.9
8	7	53.14	0.002353	638.0	99.1	0.2620	0.5760	0.1509	487.4	32.9
8	8	53.20	0.002352	635.9	99.2	0.2634	0.5740	0.1512	485.8	33.0
8	9	53.60	0.002350	638.3	99.5	0.2632	0.5760	0.1516	487.6	33.2
8	10	53.66	0.002350	636.7	99.5	0.2638	0.5745	0.1516	486.4	33.2
4	14	58.90	0.002304	639.1	131.8	0.3481	0.5747	0.2000	488.2	57.0
4	15	59.00	0.002303	636.6	132.2	0.3504	0.5725	0.2006	486.3	57.3
4	16	59.20	0.002302	640.9	132.3	0.3483	0.5762	0.2007	489.6	57.4
4	17	59.38	0.002301	638.9	132.2	0.3493	0.5743	0.2006	488.1	57.3
4	18	59.73	0.002299	640.9	133.0	0.3503	0.5759	0.2018	489.6	57.9
4	19	59.80	0.002298	641.8	133.0	0.3499	0.5767	0.2018	490.3	57.9
4	23	62.09	0.002265	642.5	165.8	0.4354	0.5774	0.2514	490.9	88.7
4	24	62.06	0.002266	639.8	165.6	0.4370	0.5749	0.2513	488.7	88.6
4	25	62.52	0.002263	637.9	166.2	0.4399	0.5730	0.2520	487.3	89.1
4	26	62.60	0.002263	639.4	166.2	0.4388	0.5744	0.2520	488.5	89.1
4	27	62.73	0.002264	643.1	166.7	0.4374	0.5776	0.2526	491.3	89.6
5	25	65.43	0.002234	642.5	199.2	0.5233	0.5771	0.3020	490.8	126.3
5	26	64.94	0.002237	643.1	199.1	0.5227	0.5779	0.3021	491.3	126.3
5	27	65.18	0.002235	639.0	199.3	0.5263	0.5741	0.3022	488.2	126.4
5	28	64.88	0.002236	642.8	199.8	0.5245	0.5777	0.3030	491.1	127.1
5	29	62.80	0.002246	638.5	198.9	0.5259	0.5750	0.3024	487.8	126.6
5	30	63.32	0.002244	640.2	198.7	0.5238	0.5762	0.3018	489.1	126.2
5	31	63.50	0.002243	641.6	199.1	0.5238	0.5773	0.3024	490.1	126.7
9	5	68.79	0.002237	641.4	198.8	0.5233	0.5742	0.3005	490.0	126.0
9	6	70.64	0.002229	643.6	198.8	0.5215	0.5751	0.2999	491.6	125.5
9	7	70.43	0.002230	643.9	198.9	0.5215	0.5755	0.3001	491.9	125.7
9	8	70.60	0.002230	644.7	198.4	0.5194	0.5761	0.2993	492.5	125.0
9	9	70.82	0.002229	644.3	199.5	0.5225	0.5758	0.3008	492.2	126.3
9	10	70.65	0.002230	642.3	199.4	0.5240	0.5741	0.3008	490.7	126.3
5	19	67.02	0.002197	695.5	231.3	0.5613	0.6257	0.3512	531.3	167.4
5	20	67.40	0.002195	695.7	231.1	0.5608	0.6257	0.3509	531.5	167.1
5	21	67.40	0.002196	693.0	231.0	0.5626	0.6233	0.3507	529.4	166.9
5	22	67.50	0.002195	694.5	231.4	0.5624	0.6246	0.3513	530.6	167.4
5	23	67.78	0.002193	696.2	231.7	0.5616	0.6260	0.3515	531.9	167.7

Table D-7b. JVX 1991 Phase II rotor performance data, as given in the database.

Run	Point	RTRDFS	AFRBC	AFFLEX	COLL	TORQ	TORQC	SPBSF
4	6	-1602.9	1818.4	-268.2	23.51	6126	6173	134.5
4	7	-2158.6	2326.3	-237.3	24.30	8090	8126	131.8
4	8	-2724.5	2861.3	-223.7	25.22	10118	10148	126.2
4	9	-3328.9	3433.8	-209.4	25.89	12154	12176	124.3
4	10	-3868.1	3945.3	-199.2	26.58	14191	14208	127.7
4	11	-4268.0	4327.1	-195.9	27.49	15903	15916	128.5
4	12	-4542.5	4588.6	-191.8	27.84	16935	16945	133.6
8	5	-1551.8	1761.3	-260.7	23.58	5960	6005	125.2
8	6	-2179.2	2276.4	-167.4	24.37	8165	8186	123.3
8	7	-2729.7	2823.0	-179.9	25.31	10061	10081	124.0
8	8	-3283.6	3363.9	-184.3	26.29	12093	12110	122.3
8	9	-3871.2	3931.1	-182.5	27.18	14251	14264	130.0
8	10	-4320.8	4364.5	-181.4	27.96	16000	16010	122.6
4	14	-1139.6	1633.1	-544.5	29.64	5933	6039	214.7
4	15	-1620.0	1965.4	-415.4	30.33	8135	8209	241.8
4	16	-2153.7	2351.7	-289.1	30.77	10584	10627	227.6
4	17	-2496.2	2670.5	-279.0	31.34	12164	12202	228.7
4	18	-3301.1	3417.4	-253.6	32.40	15962	15986	229.6
4	19	-3593.9	3700.8	-255.3	32.78	17250	17273	228.9
4	23	-1632.1	2081.5	-538.0	36.23	10296	10393	356.8
4	24	-1966.5	2313.1	-452.4	36.72	12304	12378	356.1
4	25	-2208.0	2484.6	-394.2	37.00	13680	13739	353.9
4	26	-2531.0	2749.3	-351.8	37.42	15529	15575	360.3
4	27	-2956.1	3097.4	-295.0	37.61	17870	17900	364.0
5	25	-630.3	1375.3	-796.5	40.87	5992	6151	510.7
5	26	-899.7	1610.8	-777.8	41.27	7762	7915	508.7
5	27	-1283.1	1923.7	-728.6	41.73	10228	10365	516.8
5	28	-1617.7	2144.0	-634.2	42.04	12538	12651	511.5
5	29	-1846.8	2279.5	-554.1	42.15	14116	14209	510.6
5	30	-2031.6	2368.6	-468.9	42.26	15335	15407	499.7
5	31	-2297.8	2641.2	-490.0	42.57	17049	17123	500.9
9	5	-550.7	1272.2	-768.2	40.62	5431	5585	500.6
9	6	-820.6	1486.8	-728.1	40.79	7192	7334	499.8
9	7	-1254.5	1830.5	-661.1	41.15	9897	10021	508.5
9	8	-1614.3	2068.1	-560.2	41.46	12382	12479	495.8
9	9	-1972.3	2286.9	-442.4	41.88	14860	14928	501.6
9	10	-2253.4	2677.9	-567.9	42.58	16670	16761	518.7
5	19	-834.4	1556.2	-796.9	44.04	8725	8879	676.2
5	20	-962.8	1677.9	-796.4	44.13	9464	9618	677.5
5	21	-1287.1	1968.5	-782.6	44.46	11761	11907	677.1
5	22	-1747.7	2369.9	-749.2	44.72	14772	14905	677.6
5	23	-1995.6	2572.8	-719.0	44.94	16490	16614	672.1

Table D-7c. JVX 1991 Phase II rotor performance data, original (text labels) and as recalculated (italic symbols).

Run	Point	ETAIS,F	CTISS	T	C_T/σ	C_P/σ	η
4	6	0.8546	0.03026	1474.6	0.02783	0.00932	0.7862
4	7	0.8736	0.04063	2030.3	0.03822	0.01224	0.8216
4	8	0.8881	0.05179	2596.3	0.04935	0.01543	0.8463
4	9	0.8970	0.06250	3200.6	0.06009	0.01829	0.8624
4	10	0.8910	0.07218	3739.8	0.06978	0.02121	0.8615
4	11	0.8876	0.08054	4140.0	0.07813	0.02403	0.8609
4	12	0.8840	0.08506	4414.6	0.08267	0.02539	0.8591
8	5	0.8467	0.02922	1423.3	0.02679	0.00904	0.7765
8	6	0.8742	0.04088	2050.9	0.03847	0.01228	0.8227
8	7	0.8869	0.05102	2601.3	0.04862	0.01507	0.8452
8	8	0.8927	0.06181	3155.4	0.05940	0.01824	0.8578
8	9	0.8930	0.07238	3743.1	0.06998	0.02133	0.8634
8	10	0.8900	0.08120	4192.7	0.07879	0.02407	0.8636
4	14	0.8210	0.02168	1034.5	0.01968	0.00919	0.7453
4	15	0.8644	0.03107	1515.2	0.02906	0.01260	0.8085
4	16	0.8824	0.04078	2048.9	0.03879	0.01610	0.8395
4	17	0.8932	0.04757	2391.4	0.04557	0.01860	0.8557
4	18	0.9042	0.06259	3196.9	0.06061	0.02425	0.8756
4	19	0.9100	0.06797	3489.7	0.06600	0.02614	0.8836
4	23	0.8547	0.03124	1557.5	0.02982	0.01592	0.8157
4	24	0.8679	0.03797	1891.8	0.03652	0.01911	0.8349
4	25	0.8836	0.04293	2133.8	0.04148	0.02137	0.8539
4	26	0.8914	0.04897	2456.8	0.04753	0.02411	0.8652
4	27	0.9029	0.05652	2882.3	0.05511	0.02738	0.8804
5	25	0.6702	0.01224	591.8	0.01149	0.00955	0.6293
5	26	0.7427	0.01741	861.4	0.01667	0.01225	0.7110
5	27	0.8144	0.02516	1244.8	0.02442	0.01627	0.7901
5	28	0.8384	0.03134	1580.1	0.03062	0.01961	0.8190
5	29	0.8544	0.03610	1808.8	0.03536	0.02222	0.8368
5	30	0.8634	0.03954	1993.1	0.03879	0.02399	0.8470
5	31	0.8787	0.04455	2259.8	0.04382	0.02656	0.8642
9	5	0.6449	0.01072	512.0	0.00996	0.00869	0.5996
9	6	0.7293	0.01591	781.5	0.01515	0.01138	0.6945
9	7	0.8160	0.02429	1215.6	0.02354	0.01552	0.7907
9	8	0.8399	0.03118	1574.8	0.03042	0.01928	0.8193
9	9	0.8630	0.03816	1934.0	0.03741	0.02310	0.8462
9	10	0.8805	0.04385	2215.0	0.04310	0.02609	0.8655
5	19	0.6593	0.01406	835.6	0.01408	0.01197	0.6602
5	20	0.7017	0.01622	963.7	0.01624	0.01297	0.7024
5	21	0.7602	0.02185	1287.8	0.02186	0.01617	0.7606
5	22	0.8243	0.02955	1748.9	0.02957	0.02016	0.8249
5	23	0.8432	0.03360	1997.1	0.03363	0.02238	0.8439

Spinner Pressure Data

Phase I spinner pressure data were taken from a single transducer (SPBP), in units of lb/in^2, referenced to the static pressure ring. Table D-8 lists the spinner pressures for three tip speeds not in Table D-6. Here, RHO100 evidently means that the density was multiplied by a factor of 100, and SPBP has the opposite sign as SPBPR etc. in Phase II. For Phase I, the nominal spinner base force is computed as

$$\text{SPBSF} = \text{SPBP} \times 577.7\text{in}^2$$

Phase II spinner pressure data were taken from three transducers, listed in the database as SPBPR, SPBPI1, and SPBI2, all in lb/in^2 and referenced to the static pressure ring. The values are listed in Table D-9. The spinner base force is computed as

$$\text{SPBSF} = \text{SPBPR} \times 96.1\text{in}^2 + \text{SPBPI1} \times 190.0\text{in}^2 + \text{SPBP2} \times 237.3\text{in}^2$$

The Phase II pressure data are questionable: the values are an order of magnitude higher than the Phase I pressures and are of the wrong expected sign. They are included here only for reference.

Table D-8. JVX 1988 Phase I spinner pressures, blades on.

Run	Point	RHO100	VTIP	VKTS	MTUN	QPSF	SPBP
38	4	0.2305	435.9	98.5	0.1480	31.85	-0.0752
38	5	0.2302	433.3	98.9	0.1486	32.08	-0.0784
38	6	0.2277	429.4	130.8	0.1963	55.46	-0.1325
38	7	0.2273	432.0	131.2	0.1968	55.72	-0.1318
38	8	0.2239	429.4	165.4	0.2478	87.21	-0.2028
38	9	0.2233	437.2	165.7	0.2479	87.28	-0.2049
38	10	0.2192	430.7	199.6	0.2983	124.36	-0.2937
38	11	0.2188	411.0	199.7	0.2982	124.25	-0.2938
43	3	0.2283	651.9	131.2	0.1965	55.97	-0.1426
43	5	0.2268	658.4	143.0	0.2138	66.02	-0.1730
43	6	0.2267	655.8	143.0	0.2139	66.08	-0.1747
43	8	0.2249	653.2	143.3	0.2134	65.79	-0.1746
46	3	0.2147	654.5	220.0	0.3284	149.54	-0.3560
50	3	0.2179	646.6	217.5	0.3273	148.37	-0.3520
51	3	0.2132	547.2	217.9	0.3225	144.18	-0.3257
52	3	0.2150	548.5	216.8	0.3245	145.47	-0.3250

Table D-9. JVX 1991 Phase II spinner pressure data. SPBSF is recalculated.

Run	Point	SPBPR	SPBPI1	SPBPI2	SPBSF
4	6	0.2103	0.2649	0.2694	134.5
4	7	0.2050	0.2593	0.2647	131.8
4	8	0.1922	0.2503	0.2537	126.2
4	9	0.1868	0.2476	0.2497	124.3
4	10	0.1947	0.2538	0.2561	127.7
4	11	0.1943	0.2562	0.2576	128.5
4	12	0.2038	0.2659	0.2677	133.6
8	5	0.1933	0.2500	0.2493	125.2
8	6	0.1899	0.2467	0.2453	123.3
8	7	0.1880	0.2498	0.2465	124.0
8	8	0.1844	0.2473	0.2429	122.3
8	9	0.2009	0.2588	0.2591	130.0
8	10	0.1869	0.2456	0.2445	122.6
4	14	0.3278	0.4249	0.4319	214.7
4	15	0.3789	0.4769	0.4837	241.8
4	16	0.3514	0.4500	0.4566	227.6
4	17	0.3528	0.4527	0.4585	228.7
4	18	0.3534	0.4557	0.4598	229.6
4	19	0.3503	0.4540	0.4592	228.9
4	23	0.5585	0.7050	0.7130	356.8
4	24	0.5567	0.7032	0.7120	356.1
4	25	0.5520	0.7004	0.7072	353.9
4	26	0.5648	0.7117	0.7198	360.3
4	27	0.5721	0.7197	0.7259	364.0
5	25	0.8147	1.0104	1.0133	510.7
5	26	0.8084	1.0067	1.0101	508.7
5	27	0.8256	1.0201	1.0268	516.8
5	28	0.8126	1.0107	1.0171	511.5
5	29	0.8110	1.0078	1.0162	510.6
5	30	0.7898	0.9879	0.9949	499.7
5	31	0.7911	0.9873	0.9999	500.9
9	5	0.8002	0.9945	0.9892	500.6
9	6	0.8044	0.9912	0.9868	499.8
9	7	0.8165	1.0090	1.0042	508.5
9	8	0.7970	0.9832	0.9795	495.8
9	9	0.8055	0.9948	0.9909	501.6
9	10	0.8397	1.0259	1.0243	518.7
5	19	1.0825	1.3340	1.3429	676.2
5	20	1.0842	1.3370	1.3456	677.5
5	21	1.0821	1.3390	1.3430	677.1
5	22	1.0831	1.3390	1.3447	677.6
5	23	1.0765	1.3260	1.3347	672.1

Phase I Tares

In the absence of reliable spinner drag measurements from the Phase II test, the best spinner tare data are those from the Phase I test. Test conditions and tare data are tabulated in Table D-10, all at 495–496 rpm, blades off.

Table D-10a. JVX 1998 Phase I spinner tare test conditions, blades off.

Run	Point	TEMP	RHO100	VKTS	MTUN	RPM	QPSF
57	3	69.99	0.2271	131.2	0.1971	496	55.7
57	4	73.93	0.2253	131.4	0.1966	495	55.4
57	5	74.85	0.2250	131.2	0.1961	495	55.1
57	6	77.33	0.2220	165.3	0.2471	495	86.4
57	7	78.99	0.2213	165.2	0.2466	495	86.1
57	8	79.75	0.2210	165.1	0.2462	495	85.8
57	9	81.46	0.2177	203.0	0.3031	495	127.7
57	10	83.56	0.2169	203.0	0.3025	495	127.3
57	11	84.81	0.2165	202.9	0.3020	495	126.9
57	13	87.44	0.2140	220.7	0.3283	495	148.5
57	14	88.85	0.2135	220.5	0.3276	495	147.9
57	15	89.79	0.2132	220.4	0.3272	495	147.5
57	16	91.62	0.2109	238.4	0.3539	496	170.8
57	17	93.22	0.2105	238.2	0.3530	495	170.0
57	18	93.76	0.2102	238.1	0.3527	496	169.6
57	19	95.08	0.2098	237.9	0.3520	52	169.1

Table D-10b. JVX 1998 Phase I spinner tare data, blades off.

Run	Point	PSI	RTRDFS	DSP/QPSF	SPBP
57	3	0	52.6	0.945	-0.0324
57	4	-3	61.2	1.104	-0.0351
57	5	-6	65.7	1.192	-0.0375
57	6	0	87.2	1.009	-0.0590
57	7	-3	92.2	1.071	-0.0587
57	8	-6	95.5	1.113	-0.0624
57	9	0	124.6	0.976	-0.0855
57	10	-3	127.6	1.003	-0.0902
57	11	-6	134.4	1.059	-0.0935
57	13	0	141.7	0.954	-0.1063
57	14	-3	145.6	0.985	-0.1114
57	15	-6	152.4	1.033	-0.1142
57	16	0	155.9	0.913	-0.1246
57	17	-3	161.4	0.949	-0.1327
57	18	-6	169.2	0.997	-0.1400
57	19	-6	165.8	0.980	-0.1403

References

1. Felker, F. F.; Signor, D. B.; Young, L. A.; and Betzina, M. D.: Performance and Loads Data From a Hover Test of a 0.658-Scale V-22 Rotor and Wing. NASA TM-89419, April 1987.

2. Felker, F. F.: Results From a Test of a 2/3-Scale V-22 Rotor and Wing in the 40- by 80-Foot Wind Tunnel. American Helicopter Society 47th Annual Forum, Phoenix, AZ, May 1991.

3. Young, L. A.; Booth, E. R.; Yamauchi, G. K.; Botha, G.; and Dawson, S.: Overview of the Testing of a Small-Scale Proprotor. American Helicopter Society 55th Annual Forum, Montréal, Québec, Canada, May 1999.

4. Acree, C. W.: Calculation of JVX Proprotor Performance and Comparisons with Hover and High-Speed Test Data. American Helicopter Society Specialists' Conference on Aeromechanics, San Francisco, CA, Jan. 2008.

5. Acree, C. W.: JVX Proprotor Performance Calculations and Comparisons with Hover and Airplane-Mode Test Data. NASA TM-2009-215380, April 2009.

6. Sheng, C.: Predictions of JVX Rotor Performance in Hover and Airplane Mode Using High-Fidelity Unstructured Grid CFD Solver. American Helicopter Society 70th Annual Forum, Montréal, Québec, Canada, May 2014.

7. Castrup, S. and Castrup, H. T.: Measurement Uncertainty Analysis Principles and Methods. NASA-HDBK-8739.19-3, July 2010.

8. Crow, E. L.; Davis, F. A.; and Maxfield, M. W.: Statistics Manual. Dover Publications, New York, NY, 1960.

9. Taylor, B. N. and Kuyatt, C. E.: Guidelines for Evaluating and Expressing the Uncertainty of NIST Measurement Results. NIST TN 1297, Sept. 1994.

10. Jenks, M. D. and Narramore, J. C.: Final Report for the 2-D Test of Model 901 Rotor and Wing Airfoils (BSWT 592). Bell-Boeing Report No. D901-99065-1, May 1984.

11. Bartie, K.; Alexander, H.; McVeigh, M.; La Mon, S.; and Bishop, H.: Hover Performance Tests of Baseline Metal and Advanced Technology Blade (ATB) Rotor Systems for the XV-15 Tilt Rotor Aircraft. NASA CR-177436, Oct. 1986.

12. Potsdam, M. A. and Strawn, R. C.: CFD Simulations of Tiltrotor Configurations in Hover. American Helicopter Society 58th Annual Forum, Montréal, Québec, Canada, June 2002.

13. Johnson, W.: Calculation of Tilt Rotor Aeroacoustic Model (TRAM DNW) Performance, Airloads, and Structural Loads. American Helicopter Society Aeromechanics Specialists' Meeting, Atlanta, GA, Nov. 2000.

14. Felker, F. F.; Shinoda, P. R.; Heffernan, R. M.; and Sheehy, H. F.: Wing Force and Surface Pressure Data from a Hover Test of a 0.658-Scale V-22 Rotor and Wing. NASA TM-102244, Feb. 1990.

15. Bell Helicopter Company: Advancement of Proprotor Technology. Task II – Wind-Tunnel Test Results. NASA CR-114363, Bell Report 300-099-004, Sept. 1971.

16. Johnson, W.: Airloads and Wake Geometry Calculations for an Isolated Tiltrotor Model in a Wind Tunnel. 27th European Rotorcraft Forum, Moscow, Russia, Sept. 11–14, 2001.

17. Kottapolli, S.: Neural Network Research on Validating Experimental Tilt-Rotor Performance. 16th AIAA Applied Aerodynamics Conference, Albuquerque, NM, June 1998.

18. Rosenstein, H.: Aerodynamic Development of the V-22 Tilt Rotor. 12th European Rotorcraft Forum, Bonn, Germany, Sept. 1986.

19. Johnson, W.: *Rotorcraft Aeromechanics*, Cambridge University Press, 2013.

20. Johnson, W.: CAMRAD II Comprehensive Analytical Model of Rotorcraft Aerodynamics and Dynamics. Johnson Aeronautics, Palo Alto, CA, 2007.

21. Bousman, W. G.: Aerodynamic Characteristics of SC1095 and SC1094 R8 Airfoils. NASA TP-2003-212265, AFDD TR-04-003, Dec. 2003.

22. McCroskey, W. J.: A Critical Assessment of Wind Tunnel Results for the NACA 0012 Airfoil. AGARD Fluid Dynamics Panel Symposium on Aerodynamic Data Accuracy and Quality; Requirements and Capabilities in Wind Tunnel Testing, Naples, Italy, Sept. 28–Oct. 2, 1987; also, NASA TM-100019, USAAVSCOM TM 87-A-5, Oct. 1987.

23. Maughmer, M. D. and Coder, J. G.: Comparisons of Theoretical Methods for Predicting Airfoil Aerodynamic Characteristics. RDECOM TR 10-D-106, Aug. 2010.

24. Corrigan, J. J. and Schillings, J. J.: Empirical Model for Stall Delay Due to Rotation. American Helicopter Society Aeromechanics Specialists' Conference, San Francisco, CA, Jan. 1994.

25. Du, Z. and Selig, M. S.: A 3-D Stall-Delay Model for Horizontal Axis Wind Turbine Performance Prediction. AIAA Paper 98-0021, Jan. 1998.

26. Yamauchi, G. K. and Johnson, W.: Trends of Reynolds Number Effects on Two-Dimensional Airfoil Characteristics for Helicopter Rotor Analyses. NASA TM-84363, April 1983.

27. Narramore, J. C.: Airfoil Design, Test, and Evaluation for the V-22 Tilt Rotor Vehicle. American Helicopter Society 43rd Annual Forum, St. Louis, MO, May 1987.

28. Johnson, W.: Rotorcraft Aerodynamics Models for a Comprehensive Analysis. American Helicopter Society 54th Annual Forum, Washington, D.C., May 1998.

29. Glauert, H.: *The Elements of Aerofoil and Airscrew Theory*, Chap. XVII, pp. 222–226, Cambridge University Press, 2nd Ed., 1947.

30. Pope, A. and Harper, J. J.: *Low-Speed Wind Tunnel Testing*, pp. 362–364, John Wiley and Sons, 1966.

31. Fitzgerald, R. E.: Wind Tunnel Blockage Corrections for Propellers. M.S. Thesis, University of Maryland, 2007.